TWO-DIMENSIONAL INVERSE SCATTERING PROBLEM OF PEC AND MIXED BOUNDARY SCATTERERS

YE XIUZHU

(*B. Eng, Harbin Institute of Technology, China*)

A THESIS SUBMITTED

FOR THE DEGREE OF DOCTOR OF PHILOSOPHY

DEPARTMENT OF ELECTRICAL AND COMPUTER ENGINEERING

NATIONAL UNIVERSITY OF SINGAPORE

2012

Acknowledgement

At this very exciting and proud moment, the very first person I would like to thank is my supervisor Dr. Chen Xudong, only with whose patient and endeavored guidance I can complete this thesis. He not only imparts knowledge, but also provides moral education on the spirit of being a real researcher. From him, I learned to be strict with work and humble to be a person. As a Chinese old saying goes ‘once a teacher, forever a teacher like farther’, these four years study with Dr. Chen is certainly a life time treasure for me.

I would like to thank all the staffs in Microwave and RF research group in National University of Singapore, for teaching me the fundamentals of electromagnetic, for providing constructive suggestions, and for establishing a pleasant and home like lab environment. I thank my teammates and friends, Dr. Krishna Agarwal, Dr. Zhong Yu and Dr. Song Rencheng, etc., who are always there to provide selfless help.

I also would like to thank all my best friends. A sincere friendship is the most priceless treasure in the world. Rough roads are becoming smooth only with all these many friends’ accompany. They are the color of my life.

I gratefully thank my parents, who are the first teachers in my life, who have given me the warmest and happiest family in the world, who have supported me to follow my dream with all the effort and give me the most selfless love. I would like to thank them for raising me up, to more than I can be.

Table of Contents

Summary

This thesis studies several applications of subspace based optimization method (SOM) for solving two dimensional inverse scattering problems. The original contributions of this thesis are: Firstly, we proposed a perfect electric conductor (PEC) inverse scattering approach based on SOM, which is able to reconstruct PEC objects of arbitrary quantity and shape without requiring prior information on the approximate locations or the quantity of the unknown scatterers. Two editions of the approach are introduced. In the first edition, a binary vector serves as the representation for scatterers, such that the optimization method involved is the discrete type steepest descent method. In the second edition, a continuous expression for the binary vector is introduced which enables the usage of the alternative two-step conjugate-gradient optimization method. The second edition is more robust and faster convergence than the first one. Secondly, by successfully extending the SOM to the modeling scheme of *T*-matrix method, we solved the challenging problem of reconstructing a mixture of both PEC and dielectric scatterers together. Thirdly, we propose a modified SOM to solve the separable obstacle problem. Various numerical results are carried out to validate the proposed methods.

List of tables

List of Figures

List of Acronyms

EM wave	Electromagnetic wave
DBIM	Distorted Born iteration method
MGM	Modified gradient method
CSI	Contrast source inversion
SOM	Subspace-based optimization method
SVD	Singular value decomposition
PEC	Perfect electric conductors
SOP	Separable obstacle problem
EFIE	Electric field integral equation
BIM	Born iteration method
CG	Conjugate gradient
STIE	Source type integral equation
TE	Transverse electric
TM	Transverse magnetic
KM	Kirchhoff's method
LSF	Local shape function
MoM	Method of moments
MSR	Multistatic response
FEM	Finite element method
FD	Finite difference
LM	Levenberg–Marquardt

List of Publications

The content of the following papers has been included in Chapter 2

1) **Xiuzhu Ye**, Xudong Chen, Yu Zhong, and Krishna Agarwal, "Subspace-based optimization method for reconstructing perfectly electric conductors," *Progress in Electromagnetics Research*, vol. 100, pp. 119-128, 2010.
2) **Xiuzhu Ye**, Yu Zhong, and Xudong Chen, "Reconstructing perfectly electric conductors by the subspace-based optimization method with continuous variables," *Inverse Problems*, vol. 27, p.055011, 2011.
3) **Xiuzhu Ye** and Xudong Chen, "The Role of Regularization Parameter of Subspace-based Optimization Method in Solving Inverse Scattering Problems," *APMC: 2009 Asia Pacific Microwave Conference*, Singapore, vols 1-5, pp. 1549-1552, 2009.
4) **Xiuzhu Ye** and Xudong Chen, "Investigation of the optimization progress of the subspace based optimization method in reconstructing perfect electric conductors," *APMC*: *Asia Pacific Microwave Conference*, Melbourne, Australia, 2011.
5) **Xiuzhu Ye** and Xudong Chen, "The investigation of the regularization term in the continuous-parameter subspace based optimization method in reconstructing PEC objects," *Cross Strait Quad-Regional Radio Science and Wireless Technology Conference*, Harbin, China, 2011.

The content of the following paper is included in Chapter 3

6) **Xiuzhu Ye**, Xudong Chen and Yu Zhong, "Inverse scattering for a mixture of dielectric and perfectly conducting scatterers via subspace based optimization method", *IEEE Transactions on Antennas and Propagation*, submitted, 2011.

The content of the following paper is included in Chapter 4

7) **Xiuzhu Ye**, Rencheng Song, Krishna Agarwal and Xudong Chen, "Electromagnetic imaging of separable obstacle problem", *Optics Express*, vol. 20, pp. 2206-2219, 2012.

In addition, there are three papers the contents of which are not included in this thesis

8) **Xiuzhu Ye,** Xudong Chen, "The subspace-based optimization method in reconstruction of perfectly electric conductors" *Progress In Electromagnetics Research Symposium(PIERS)*, Marrakesh, Morocco, 2011.

9) **Xiuzhu Ye,** Xudong Chen, "Electromagnetic Inverse Scattering of Perfectly Electric Conductors by the Subspace-based Optimization Method", *Progress In Electromagnetics Research Symposium (PIERS)*, Suzhou, China, 2011.

10) Xudong Chen, **Xiuzhu Ye**, "Reconstructing Perfect Electric Conductors by Subspace-based Optimization Method with Continuous Variables", *Applied Inverse Problems Conference (AIPC)*, TAMU, USA, 2011.

1 INTRODUCTION

1.1 Overview of Inverse Scattering Problem

The inverse problem is general framework of utilizing the measurement data at hand to recover the physical description and information about an object or system that cannot be accessed directly. It is of great practical importance to modern techniques. We call two problems inverse to each other if the formulation of each of them requires full or partial knowledge of the other [1]. Practically, the one which is already thoroughly investigated and theoretically easier to be solved is defined as the forward problem. On the contrary, the one which is less studied and hard to be solved is called the inverse problem. Another important difference between the forward and inverse problem is the ill-poseness. Inverse problems are mostly ill-posed while the corresponding forward problems are usually well-posed. In Hadamard's sense [2], a problem is well-posed if the following conditions are satisfied:

1. The solution exists (existence)
2. The solution is unique (uniqueness)
3. The solution depends in a continuous manner on the data (stability)

On the contrary, a problem is ill-posed if one of the properties above fails.

This thesis aims to deal with the electromagnetic inverse scattering problem, i.e. to image or reconstruct the spatial distribution of refraction index of the unknown scatterers from the knowledge of the measured scattering data. Electromagnetic

inverse scattering problem is of essential importance in many fields, such as biomedical imaging, non-destructive testing, remote sensing, geological exploration, radar processing, civilian engineering, national security, microscopy, etc.

In all these applications, the scatterers to be reconstructed are assumed to be known *a priori* inside one certain domain of interest. To get the scattering data for reconstruction, the experimental step is to firstly probe the domain of interest by using several electromagnetic (EM) waves (cylindrical wave, spherical wave or plane wave) from different directions. The wave travels through the domain of interest, onto the scatterers and is scattered off. Then several receivers located outside the domain of interest (mostly in the far field) record down the measured scattered field.

In this thesis we discuss the case where the frequencies of the wave are in *resonance region* [3], i.e., the sizes of the unknown scatterers under consideration are compatible to wavelength of the EM wave. Such kind of inverse scattering problems are both ill-posed and nonlinear. The number of unknowns (number of subunits in the discrete model) is always larger than that of measurement points. The mapping operator from the induced current to the scattered field outside is compact. In addition the scattered field depends in a highly nonlinear manner on the unknown configurations, i.e. the permittivity, permeability, conductivity, shape and quantity of the scatterers.

The existence of solution for inverse scattering problem can be guaranteed by properly choosing the data space. Since the mapping from induced currents to the scattered field is compact, there could be non-unique solutions to the induced current

given one scattered field. Thus the spatial distribution of the unknown scatterers cannot be uniquely determined by only one incidence [4]. Even though the ambiguity of the induced current changes along with different incident waves, the material properties of the scatterer do not change. Thus the uniqueness of the solution for material properties can be guaranteed by several incidences from different angles [3].

The most difficult part of inverse scattering problems comes mainly from the instability of the solution. Instability can be understood in the sense that the solution of the problem is quite sensitive to the input data, such that a slight change in the input data will cause a severe change in the reconstruction result. Practically, noise is always present in the measured data. As a result, regularization schemes are needed to stabilize the solution.

Till now, the nature of the inverse scattering problem is discussed—nonlinearity and ill-poseness. Algorithms for solving such kind of problem usually involve optimization scheme, in which the unknown configurations are parameterized and being determined by minimizing a cost function containing the measured and calculated scattered fields. In the meanwhile, iterative scheme are commonly needed, such as the distort Born iteration method (DBIM) [5, 6], modified gradient method (MGM) [7-11], the contrast source inversion method (CSI) [12-15] and subspace based optimization method (SOM) [16-23]. Besides, regularization schemes should also be included to stabilize the optimization, such as the Tikhonov regularization method [24-28] and the truncated singular value decomposition (SVD) [29-31].

Two different categories of scatterers are considered in this thesis. The first one is the perfectly electric conducting (PEC) scatterer which is impenetrable by the EM wave. There is no electric or magnetic field inside the scatterer, and induced currents (that are conducting currents) only exist on the surface of the PEC scatterer. The second one is the dielectric scatterer which is penetrable by the EM wave and the induced currents (that are contrast displacement currents) exist throughout the whole volume of scatterer. Hence, depending on the properties of scatterers to be reconstructed, two different kinds of problems are discussed in this thesis. The first one is the inverse scattering problem for PEC scatterers only. The property of the scatterers to be reconstructed is known as *a priori* information. Only the locations and boundaries for the PEC scatterers need to be reconstructed. Methods for solving such kind problem will be reviewed in section 1.2. The second problem is the mixed boundary inverse problem which involves reconstruction of PEC and dielectric scatterers together. In this mixed boundary inverse scattering problem, we will identify PEC scatterers and determine their boundaries while at the same time identify dielectric scatterers and determine the spatial distribution of their refractive index.

1.1 Outline of the thesis

This section serves to provide an outline of this thesis. In the subsequent sections of Chapter 1, the difficulties in solving inverse scattering problem are indicated. In section 1.2, we briefly review the methods that were used to solve dielectric inverse scattering problem and the methods of solving PEC scattering

problem. Then in section 1.3, we briefly describe the objectives of this thesis which lie in three subjects—the PEC inverse scattering problem, the mixed boundary inverse scattering problem, and the separable obstacle problem (SOP).

Chapter 2 presents the PEC inverse scattering problem. Section 2.1 serves as an introduction of the PEC inverse scattering problem and presents the gap of the contemporary methods which we intend to fill by SOM. Then section 2.2 presents a new forward model based on the surface integral equation which enables the construction of the cost function for SOM. Section 2.3 introduces the discrete-type SOM which utilizes the steepest gradient method as the optimization scheme. Various numerical results are given to validate the method. Section 2.4 introduces a continuous-type SOM which is developed based on the same forward model with the discrete-type SOM but with a different optimization scheme. Then in section 2.5, the optimization process of the continuous-type SOM is further discussed. Comparisons are made between the discrete-type SOM and the continuous-type SOM to give a theoretical explanation of the better performance of continuous-type SOM over the discrete-type SOM.

Chapter 3 presents the mixed boundary inverse scattering problem under the modeling scheme of *T*-matrix method. In Section 3.1, the challenges lying in solving such kind of problem are analyzed and the reasons for choosing the *T*-matrix method are discussed. In section 3.2, we derive the formulas for the forward model of *T*-matrix method in solving the mixed boundary problem. Then in section 3.3, the modification of SOM to the specific mixed boundary problem is indicated. The

criteria of classifying the PEC and dielectric scatterers are also presented in this section. Section 3.3 presents various numerical results to validate the proposed approach.

Chapter 4 presents the application of SOM in solving the specific SOP. Section 4.1 presents a brief review of the problem. And a modified SOM which well utilizes the prior information of the separable obstacle is introduced. The SOP-homo for dielectric scatterers is firstly derived from the electric field integral equation (EFIE) model. Comparisons are made between the contemporary methods to show a good performance of SOP-homo. Then in section 4.2 the SOP-homo is further extended to the *T*-matrix SOM to solve the mixed boundary SOP. Various numerical results are presented to validate the proposed approach.

Finally in Chapter 5, summary of this thesis is presented, as well as discussions of some aspects of the future work that may further improve the solver of electromagnetic inverse scattering problem.

1.2 Methodology

The methodologies for solving the dielectric scatterers and PEC scatterers are reviewed and discussed respectively in this section. For the dielectric scatterers we focus mainly on discussing the iterative methods. For PEC scatterers, we focus mainly on discussing the modeling methods which is the key issue in solving the PEC inverse scattering problem. It is highlighted that in all the works to be reviewed in the latter sections, the properties of scatterers to be reconstructed are implicitly known *a priori*.

1.2.1 Existing methods for dielectric scatterers

Methods for solving the dielectric scatterer inverse scattering problems are mostly in the framework of the EFIE. The relationship between the unknown material properties and the scattered field is highly nonlinear. Two types of iterative algorithms based on whether the forward model is linearized are introduced.

Born approximation [10, 32-39] is a linearization method in the condition that the contrast of the material is relatively low. The field inside the scatterer is replaced by the incident field and the multiple scattering effect is neglected. However, when dealing with the high contrast scatterers, the nonlinear nature of the scattering phenomena must be taken into account. Thus the Born iteration method (BIM) and DBIM are introduced as an "intermediate" solution by keeping the higher order terms of the Born expansion. In BIM [24], the Green's function, the kernel of the integral operator is fixed through the whole iteration process, and only the field inside the scatterers is updated. Besides the updating of the field inside the scatterer, the DBIM [5, 6] also updates the Green's function in each step of iteration. The cost functions of both BIM and DBIM are consisted solely by the mismatch of the scattered field measured at receivers, and repetitive recall of forward solver in each step of iteration is needed. Thus, the Born related iterative algorithms have the drawback of the highly computational cost due to the repetitive forward solution.

To overcome the burdensome forward solver calculation, a complete nonlinear model which avoids the forward solver in each iteration step is firstly realized by the MGM [7-11]. This nonlinear iteration method has properly taken into account of all multiple scattering effects, which enhances the reconstructing ability of the method.

Besides, in MGM, the cost function is constructed by two equally weighted mismatches from both the state equation which involves the total electric field inside the scatterer and the field equation which involves the scattered field measured at receivers. The regularizer is realized by the usage of state equation itself. The iterative process involves simultaneous updating of the material contrast and the field using two conjugate gradient (CG) methods running concurrently. MGM serves as an important milestone for the state and field equation type iteration algorithms.

Until now, all the methods mentioned above are Field Type methods which only involve the calculation of the fields outside and inside the scatterers. A Source Type method under the framework of source type integral equation (STIE) is introduced and developed by [40-42]. The scattering behaviors of the scatterers are well described by the introduction of the secondary or induced contrast displacement currents throughout the volume of scatterer. Two linear equations, which describe the relationship between the induced current and the material contrast, and the relationship between the induced current and the scattered field, serve as the state equation and field equation respectively. The STIE method in [40] has used the concept of radiating and non radiating currents [43]. The total induced current is a linear combination of two orthogonal complementary parts—the radiating current and the non-radiating current. The solution for the induced current is non-unique, and cannot be remedied by simply adding more experiments because of the existence of the non-radiating currents which produce zero external electric field. Thus [40] firstly extracts the radiating current from the scattered field data in the minimum norm sense

and then iteration process is involved to seek for the non-radiating current. Other methods that also use the concept of radiating and non-radiating sources are presented in [29, 44-47]. However, this work performs poorly in the presence of noise due to the fact that the zero residue in the field equation produces large error in the state equation as shown in [48].

The CSI [12-15] is a variant of the STIE based on non-forward solver idea from MGM. The cost function is consisted by both the field equation and the state equation. Two steps of CG are involved in the alternatively updating process of the induced current and material contrast. Instead of separating the induced current into two parts, CSI updates the induced current as a whole. Due to its ease of realization, the CSI method is one of the most widely used iterative methods nowadays.

Subspace based optimization method

Recently, SOM [16-23] is proposed based on the STIE to solve the dielectric scatterer inverse scattering problem.

Similar to the CSI, the cost function of SOM is also consisted by both the mismatches from field equation and state equation. SOM decomposes the induced current into two orthogonally complementary parts: the deterministic part and the ambiguous part. However the deterministic and ambiguous parts of the induced current are different from the physical radiating and non-radiating currents as in [40]. SOM studies the SVD of the mapping from induced current to the scattered field, and mathematically classify the induced current into the deterministic part which is in the span of the right singular vectors corresponding to the first L leading singular

values, and the remaining ambiguous part which is retrieved by the optimization. L is the total number of singular values that are above a predefined noise-dependent threshold. L serves as a regularization parameter. The choice of L is a consecutive range rather than a single value which makes the SOM more robust against noise than the contemporary methods.

Since the deterministic induced current is uniquely defined and serves as a good initial guess to the induced current, the number of unknowns is greatly reduced as compared to the entire induced current space in CSI. Thus the convergence speed is increased drastically. The iteration scheme alternatively updates the material contrast and the ambiguous part of induced current by using the CG, and thus full forward solver calculation in each iteration step is avoided.

Owing to all the merits discussed above, SOM serves as a good solver for the inverse scattering problem. SOM has already effectively solved the inverse problem of anistropic scatterers [16], transverse electric (TE) wave illumination[19], transverse magnetic (TM) wave illumination [17, 22], through wall imaging problem [18], inhomogeneous background problem [49] and three-dimensional case [23]. In this thesis we will further extend the application of SOM to the PEC scatterer and mixed boundary inverse scattering problems.

Besides the EFIE, another modeling scheme that is based on the *T*-matrix method serves as an alternative choice for the forward model in dielectric inverse scattering problem. Firstly introduced by Waterman [50], the *T*-matrix is derived directly from the boundary condition and well describes relationship between the

multipole expansion coefficients of the incident field and scattered field. *T*-matrix scattering coefficient is in a nonlinear relationship with the relative permittivity, however it can be linearized under the assumption of small electrical size of the scatterer [51]. *T*-matrix method has been successfully developed for both forward problems [52, 53] and inverse problems [51, 54]. Iterative methods such as the CG minimization scheme and the DBIM have been applied to the *T*-matrix inverse problems [51, 54]. However there is no published work yet that falls into the category of state and field equation based iterative method for the *T*-matrix based model. In this thesis, the extension of SOM to the modeling scheme of *T*-matrix will also fill in this gap.

1.2.2 Existing methods for PEC scatterers

The main difference between the PEC and dielectric scatterer inverse scattering problem is the method for modeling or parameterizing the unknowns. As discussed before, the boundary condition of PEC scatterer, i.e., no field appears inside the scatterer and induced current appears only on the boundary, has posed difficulty in the modeling of inverse problem. Meanwhile, the iterative methods for the dielectric case are also applicable to the PEC inverse scattering problem as long as it is properly modeled or parameterized. Therefore we will mainly focus on the discussion about methods for modeling PEC inverse scattering problem.

Similar to the Born approximation for dielectric scatterers, linearization method called the Kirchhoff's method (KM) has been developed for the PEC scatterers. By assuming the large smooth convex and closed shape of the scatterer,

KM neglects both the mutual interactions on the illuminated side of the scatterers and the induced surface current in their shadow region. Several works developed based on KM are reported [55-57]. However, this method can only reconstruct the parts facing the illumination and the complete reconstruction is not available.

Based on integral equations used to describe the scattering behavior of PEC scatterers, there are two main categories of modeling methods developed for the complete nonlinear model—the volume based method and the surface based method. The volume based method uses volume based pixels to estimate the surface of the scatterers. The main merit of this kind of method is that no prior information on the approximate centers and the quantity of the scatterers is required. Physical parameters such as the material contrast and *T*-matrix are used to describe the PEC scatterers. The surface based method involves the usage of the surface integral equation (EFIE for PEC scatterers). Most methods falling in this kind require prior information on the locations and quantity of the scatterers. Mathematical shape functions are commonly used to fit the surface of PEC scatterers. Both volume and surface based modeling methods have been proven to efficiently solve the PEC inverse scattering problem. In the following part we will discuss these two categories separately.

Volume based method

There are two kinds of parameters used to represent the PEC scatterers in the volume based method, i.e., material contrast and *T*-matrix. In [58], the concept of reconstructing conductivity for penetrable lossy scatterers is further extended to the case of PEC scatterers. Since the material contrast of PEC scatterer is dominated by

an infinity positive imaginary part, the real part can be neglected. Only a finite pure imaginary contrast is used to approximately describe the scatterer. Thus by using this pure imaginary material contrast, iterative methods for dielectric scatterers can be extended to the PEC scatterers. Then in [59], the proposed imaginary contrast modeling method is further tested by the MGM and CSI. The proposed modeling method can well cooperates with the iterative methods for dielectric scatterers. When both the real part and imaginary part of the material contrast are considered, the method can also deal with the mixed boundary problem [60, 61]. The two kinds of scatterers are distinguished by the difference of magnitude of the imaginary permittivity. However the reconstructed PEC scatterers are not significantly different from lossy dielectric scatterers.

As discussed in Section 1.2.1, the *T*-matrix is a function of relative permittivity which depends only on the boundary condition. When the relative permittivity of PEC scatterers tends to infinity, the *T*-matrix stays a finite valued parameter. In [62, 63], a binary local shape function (LSF) is assigned to each subunit to determine whether this subunit is PEC or not. Further, this binary LSF is relaxed into a real number, i.e., magnitude of the complex number that equals to the reconstructed *T*-matrix scattering coefficient divided by the true value (which is known *a priori* because the scatterers are known to be PEC). However, relaxation of LSF has caused a severe blur in the reconstruction results, which is due to the spread out of the LSF. Thus in [64, 65], the LSF is restricted as a binary number and the nonlinear discrete optimization is realized by the Genetic algorithm (GA). However,

when dealing with the irregular shaped scatterer, the crossover and mutation processes need to be specially designed to obtain the desired result, which poses burdensome extra work.

Surface based method

The surface integral equation involves the integration of the surface induced current over the contour of PEC scatterer, which however is unknown in the inverse problem. Thus mathematical expressions of the contour called the shape functions are needed to fit the surface of PEC in the updating process. The shape function can either be the Fourier series [66, 67], or the Spline function [68-76], both of which are functions of azimuth angles based on the local polar coordinate system of each scatterers. Therefore in most of the surface type methods prior information or initial guess of the quantity and centers of the scatterers are essential in the optimization process. In [70] the prior information concerning the centers of scatterers are avoided by including the centers as an extra parameter in the iterative process. Even though no prior knowledge is needed, a first guess of the number of scatterers, to which the reconstruction result is quite sensitive, is still necessary. The reconstruction results are worse when the gap between the guessed number and exact number increases. Then in [71] the quantity of the scatterers is also included as a dynamic parameter into the optimization. Thus the prior information on the quantity and centers of the scatterers is avoided. However the computational cost increases severely with the quantity of the scatterers, thus an initial guess of the maximum quantity is still needed. Another weakness of the proposed shape function method is that due to the mathematical

nature of the shape functions, some concave or sharp angular structures cannot be reconstructed by this method.

Until now, all the methods discussed above deal with only closed contoured objects which have non-empty interiors. However some very thin structures or open arcs (infinitely thinner than wavelength) are commonly encountered in the crack detecting problems. Open contoured PEC objects are investigated and successfully reconstructed in [77-79]. However there is no method reported yet that is able to reconstruct both the closed contour and open contour PEC scatterers simultaneously. In the proposed SOM for PEC, we will also fill in this gap.

1.3 Research Objectives

The subject of this thesis lies in three topics: Firstly, to investigate the SOM for solving electromagnetic inverse scattering problems for PEC scatterers. Secondly, to investigate SOM for solving the mixed boundary problem, so as to provide a full reconstruction of both shape of PEC scatterers and spatial distribution of relative permittivity of the dielectric scatterers. Thirdly, to investigate the SOM for solving the SOP, both dielectric scatterers and mixed boundary scatterers are considered, so as to provide an effective method to solve the SOP.

The original contributions for the three subjects are:

1) We developed a modeling method suitable for SOM to solve the PEC inverse scattering problem, which is the first algorithm able to simultaneously reconstruct line shaped (open contoured) scatterers and closed contour scatterers. The

modeling method falls into the category of surface based method which utilizes the EFIE. However no prior information or initial guess regarding the quantity of the scatterers or the approximate centers is needed. Further a binary vector indicating the property of the subunit is introduced to enable the construction of the state equation.

Two editions of optimization methods are developed. We call the first edition the discrete-type SOM and call the second edition the continuous-type SOM. In the first edition, considering the binary unknown vector, a discrete type optimization which utilizes the steepest descent method is applied to solve the inverse problem. Even though the proposed method is able to yield the reconstruction in just a few iteration steps, the regularization parameter does not behave smoothly and the computing time is quite long due to the full forward solver in each step of iteration. Thus in the second edition, the binary vector is approximated by a continuous function of another real valued vector. The alternative two-step CG optimization method is applied to solve the continuous type optimization. Due to the continuous behavior of the optimization, the regularization parameter behaves continuously for a consecutive range, which makes this edition of method more robust. Since no full forward solver is needed in the updating process, the continuous-type SOM is more time saving than its last version.

2) The SOM is further extended to the *T*-matrix modeling method, to fully reconstruct the mixed boundary problem. The *T*-matrix is chosen as the modeling method representing both the PEC and dielectric scatterers by a uniform volume based model. In the forward data calculation, it should be noted that even though a

single multipole is sufficient enough in describing the scattering behavior of either PEC scatterer or the dielectric scatterer, it is inaccurate to use only one multipole term to describe the mixed boundary problem because of the much stronger scattering behavior of the PEC scatterers. We give a reasonable *T*-matrix forward model for the mixed boundary problem. The iterative process which consists of retrieving the *T*-matrices is solved by SOM. Then the criterion of classifying PEC and dielectric scatterers is given based on the determination of the monopole term in *T*-matrix. The relative permittivity of the dielectric scatterer is retrieved through optimization from the *T*-matrix. We also give a reasonable representation of both dielectric scatterers and PEC scatterers in the reconstruction pattern. The *T*-matrix SOM is proved to effectively solve the mixed boundary problem.

3) SOM is reformulated to solve the SOP. The practical problem of imaging scatterers that are *separable* from the known obstacles is addressed. Such problem is commonly encountered in the non-destructive evaluation of the optical fiber as well as some through wall imaging application. Using such *a priori* information, the obstacle is regarded as a known scatterer rather than part of the background and can be excluded from the retrieving process by reformulating the cost function. As a result, the proposed method transforms the problem into an inverse scattering problem with homogeneous background, and avoids the computationally intensive calculation of the Green's function for inhomogeneous background. As a result, we call our proposed method SOP-homo. Meanwhile, the factors that influence the imaging quality for such kind of problem are also analyzed. Comparisons are made with the SOM that

uses Green's function with inhomogeneous background. The SOP-homo is proved to be valid for dielectric SOP as well as the mixed boundary SOP. The dielectric SOP is solved under the model of EFIE while the mixed boundary SOP is solved under the model of *T*-matrix method.

2 THE INVERSE SCATTERING PROBLEM OF PEC SCATTERERS

In this chapter, reconstruction of PEC scatterers by SOM is presented. Apart from the information that the unknown object is PEC, no other prior information such as the number of the objects, the approximate locations or the centers is needed. The background medium, together with scatterers of arbitrary number and arbitrary shapes, is effectively expressed as a binary vector that enables to build up the objective function.

The steepest descent method is firstly used to solve the discrete-type optimization problem. Then the binary representation of the PEC scatterer is approximated by a continuous function of another vector such that the alternative two-step CG optimization method can be applied to solve the continuous-type optimization problem. Several numerical simulations are chosen to validate the proposed methods. In particular, a combination of a line shape (very thin) object and a closed shape object are successfully reconstructed. The SOM for PEC scatterer is found to be more complex than its counterpart for dielectric scatterers. The continuous-type SOM is found to be more robust against noise and faster convergence than the discrete-type SOM.

2.1 Introduction

The inverse scattering problem of PEC scatterers, i.e., to reconstruct the locations, contours and the exact number of PEC objects by utilizing the information of scattering data, has found wide applications in many areas, such as biomedical imaging, non-destructive testing and remote sensing.

Several methods have been developed to solve such kind of problem. One conventional method is to use the shape function (Spline function or Fourier series) under local coordinate to represent the contour of the scatterers, when given an initial guess of the number and the approximate locations of the scatterers [66, 70]. This method may fail in the case when no such prior information is provided. Another method which can avoid an initial guess of the number and locations is to discretize the domain of interest into square volume pixels and consequently PEC objects of arbitrary numbers and shapes can be represented by choosing certain pixels to be PEC [64, 65] . However, when dealing with line-shape structures (such as the “L” shape), one has to use very small squares in order to give a good modeling, which may significantly increase the computational cost.

In this chapter, we are interested in reconstructing PEC scatterers of arbitrary number and arbitrary shapes, without requiring *a priori* information on the number of the scatterers and their approximate locations. In addition, both closed-contour and line-shape scatterers are considered in the inverse scattering problem. The aforementioned conditions pose significant difficulties in not only representing the geometry of scatterers but also building up the objective function. Due to the

boundary condition on the PEC scatterer, the methods for solving the PEC inverse scattering problems are significantly different from those for the dielectric scatterers. In dielectric case, both scatterers and the background medium can be represented by permittivities such that the EFIE can be applied to the whole domain of interest. Therefore the objective function can be constructed into the function of the permittivity which can represent both the background medium and the scatterers. In the case of PEC, the EFIE is only applicable to the boundary of PEC scatterer which is however unknown in inverse problem. Therefore the objective function for the PEC case is quite different from the one used in the dielectric case.

Firstly, a discrete-type SOM for reconstructing PEC is proposed [20]. In this method, the whole domain is discretized into segments of current lines. Both the background medium and scatterers of arbitrary number and arbitrary shapes are represented by a binary mathematical vector, which enables to construct the objective function. The steepest descent method is used to solve the discrete optimization problem. This discrete-type SOM has exhibited several good properties, such as taking just a few steps of iteration to converge and being able to reconstruct both closed-contour and line-shape PEC scatterers.

Secondly, by introducing a continuous expression of the binary indicator of PEC boundary, the discrete type optimization can be converted into a continuous type, which can be solved by the alternative two-step CG optimization method with much lower computational cost. Other advantages of the continuous-type SOM over the discrete-type SOM include better robustness against noise and less dependence on the

number of leading singular values. Several numerical results are given to verify the validity of the proposed methods. The proposed continuous-type SOM for PEC scatterers not only inherits the merits of its previous version but also possesses the virtue of its counterpart of the dielectric inverse scattering, which paves the way for a high resolution reconstruction of the PEC scatterers.

2.2 Forward Problem

The inverse scattering problem under investigation is in two-dimensional setting with TM time harmonic illuminations. In another word, the whole domain of interest including the unknown scatterers as well as the incident electrical field is invariant along the z axis. Suppose that the unknown PEC scatterers are located in a given domain $D \subset R^2$. The background medium is free space, and its permittivity and permeability are denoted as ε_0 and μ_0, respectively. There are N_{inc} plane waves given by $\mathbf{E}_p^{\text{inc}}(\mathbf{r}) = \hat{z}e^{i\mathbf{k}_p \cdot \mathbf{r}}$, $p = 1, 2, ..., N_{\text{inc}}$, incident from different angles onto the domain of interest D, where $\mathbf{k}_p$ is the wave vector for the pth incidence. For each incidence, the scattered field is detected by N_{r} antennas symmetrically located around a circle with positions $\mathbf{r}_q'$, $q = 1, 2..., N_{\text{r}}$. The domain of interest is discretized into small square subunits, and side edges of square rather than the square itself are used as the elements to represent PEC scatterers. After such discretization, the method of moments (MoM) can be applied to calculate the scattered field [80].

Define a vector $\bar{J} = [J(\mathbf{r}_1), J(\mathbf{r}_2), ..., J(\mathbf{r}_N)]^{\text{T}}$ as the induced current density on the line elements, where N is the total number of line elements in the domain

and the center of each line-element is located at $\mathbf{r}_n,\ n=1,\ 2,...,N$. $\bar{E}^{\text{tot}}=[E^{\text{tot}}(\mathbf{r}_1),E^{\text{tot}}(\mathbf{r}_2),...,E^{\text{tot}}(\mathbf{r}_N)]^{\text{T}}$ and $\bar{E}^{\text{inc}}=[E^{\text{inc}}(\mathbf{r}_1),E^{\text{inc}}(\mathbf{r}_2),...,E^{\text{inc}}(\mathbf{r}_N)]^{\text{T}}$ denotes the total electric field and the incident electric field upon each element inside the domain D respectively. The relationship between them is given in a compact form,

$$\bar{E}^{\text{tot}}=\bar{E}^{\text{inc}}+\bar{\bar{G}}_{\text{D}}\cdot\bar{J} \tag{2.1}$$

where $\bar{\bar{G}}_{\text{D}}$ denotes the mapping from the induced current to the scattered field inside the domain of interest. For $m,\ n=1,\ 2,\ldots,\ N$, the entries of $\bar{\bar{G}}_{\text{D}}$ are given by $\bar{\bar{G}}_{\text{D}}(n,m)=-\frac{k\eta}{4}wH_0^{(1)}(k|\mathbf{r}_n-\mathbf{r}_m|)$, when $m\neq n$, and $\bar{\bar{G}}_{\text{D}}(n,m)=-\frac{k\eta w}{4}\{1+i\frac{2}{\pi}[\ln(\frac{\gamma kw}{4})-1]\}$ when $m=n$. Here k is the free space wave number, η is the impedance of the free space, $H_0^{(1)}$ is the Hankel function of the first kind of order zero, w is the length of the line element, and $\gamma=1.781$[80]. The scattered field received by the antennas is given by

$$\bar{E}^{\text{sca}}=\bar{\bar{G}}_{\text{s}}\cdot\bar{J} \tag{2.2}$$

where $\bar{E}^{\text{sca}}=[E_z^{\text{sca}}(\mathbf{r}_1'),E_z^{\text{sca}}(\mathbf{r}_2'),...,E_z^{\text{sca}}(\mathbf{r}_{N_{\text{r}}}')]^{\text{T}}$, $\bar{\bar{G}}_{\text{s}}(q,m)=-\frac{k\eta}{4}wH_0^{(1)}(k|\mathbf{r}_q'-\mathbf{r}_m|)$ for $q=1,\ 2,...,N_{\text{r}}$ and $m=1,\ 2,...,N$. It is clear that $\bar{\bar{G}}_{\text{s}}$ is the mapping from the current in D to the scattered field measured at receivers. Eqs. (2.1) and (2.2) are referred to as the state equation and the field equation, respectively.

2.3 A Binary Variable Subspace Based Optimization Method

2.3.1 Discrete-type SOM

For inverse problem, all the PEC boundary elements are unknown so that Eq. (2.1) cannot be explicitly established. The counterpart of Eq.(2.1) in dielectric

scatterer scenario is referred to as the state equation [17, 22, 81, 82]. In PEC scatterer scenario, the absence of an explicit state equation makes it impossible to directly apply the SOM developed for dielectric scatterer scenario.

We define an N-dimensional vector $\bar{P}$, which consists of only 1 and 0, as a judgment of whether the edge belongs to the PEC boundary. In another word, the dimension of vector $\bar{P}$ equals to the total number of line elements in domain D and a '1' element represents the PEC element and a '0' element represents the free space area. Noticing the fact that $\bar{E}^{\text{tot}}$ vanishes on the PEC boundary and in the meanwhile $\bar{J}$ equals to zero for the elements which do not belong to the boundary, we are able to arrive at the following relative residue equation, which is the counterpart of the relative residue in the state equation in the dielectric scatterer scenario [17, 22, 81],

$$\Delta^{\text{sta}} = \frac{\left\| (\sim \overline{\overline{P}}) \cdot \bar{J} \right\|^2}{\left\| \bar{J}^{\text{s}} \right\|^2} + \frac{\left\| (\overline{\overline{P}}) \cdot \bar{E}^{\text{tot}} \right\|^2}{\left\| \bar{E}^{\text{d}} \right\|^2}, \tag{2.3}$$

where $\|\cdot\|$ is the Euclidean length of a vector, $\overline{\overline{P}}$ is the diagonal matrix with $\bar{P}$ in the diagonal, and $\sim \overline{\overline{P}}$ is the diagonal matrix with the complement of $\bar{P}$ in the diagonal. $\bar{J}^{\text{s}}$ is the deterministic part of the induced current which will be introduced later. $\bar{E}^{\text{d}} = \overline{\overline{G}}_{\text{D}} \cdot \bar{J}^{\text{s}}$ is electric field generated by deterministic part of the induced current.

The SVD of $\overline{\overline{G}}_{\text{s}}$ reads $\overline{\overline{G}}_{\text{s}} = \overline{\overline{U}} \cdot \overline{\overline{\sum}} \cdot \overline{\overline{V}}^{*}$, where $\overline{\overline{U}}$ is of size $N_{\text{r}} \times N_{\text{r}}$ and is composed of the left singular vectors $\bar{u}_q$, $\overline{\overline{V}}$ is of size $N \times N$ and is composed of the right singular vectors $\bar{v}_n$. $\overline{\overline{\sum}}$ is a diagonal matrix composed of singular values

σ_n and the subscript $*$ denotes the Hermitian [83]. A basic property of SVD is $\bar{\bar{G}}_{\mathrm{s}} \cdot \bar{v}_n = \sigma_n \bar{u}_n$. The vector of scattered field $\bar{E}^{\mathrm{sca}}$ can be represented as the span of left singular vectors, and the vector of induced current density $\bar{J}$ can be represented as the span of right singular vectors $\bar{J} = \bar{\bar{V}} \cdot \bar{\alpha}$, where $\bar{\alpha}$ is an N-dimensional vector. The induced current density is decomposed into two orthogonally complementary parts: the deterministic part $\bar{J}^{\mathrm{s}}$ and the ambiguous part $\bar{J}^{\mathrm{n}}$. The subscripts s and n denote deterministic and ambiguous parts resp ectively. The equation can be expressed as $\bar{J} = \bar{J}^{\mathrm{s}} + \bar{J}^{\mathrm{n}} = \bar{\bar{V}}^{\mathrm{s}} \bar{\alpha}^{\mathrm{s}} + \bar{\bar{V}}^{\mathrm{n}} \bar{\alpha}^{\mathrm{n}}$, where $\bar{\bar{V}}^{\mathrm{s}}$ is the signal subspace that contains the first L columns of $\bar{\bar{V}}$, $\bar{\bar{V}}^{\mathrm{n}}$ is the noise subspace composed of the last $M-L$ columns of $\bar{\bar{V}}$, and L is the number of the total singular values that are above a predefined noise-dependent threshold (method for choosing L will be discussed later). Even though the total induced current density cannot be uniquely determined from the scattered field, the deterministic part can be uniquely determined, with the coefficients,

$$\alpha_j^{\mathrm{s}} = \frac{u_j^* \cdot \bar{E}^{\mathrm{sca}}}{\sigma_j}, \; j = 1, 2, \ldots, L. \tag{2.4}$$

After $\bar{J}^{\mathrm{s}}$ is determined from the Eq.(2.4) by the SVD, the residue due to the mismatch of the scattering data in field equation can be expressed as

$$\Delta^{\mathrm{fie}} = \frac{\left\| \bar{\bar{G}}_{\mathrm{s}} \cdot \bar{\bar{V}}^{\mathrm{n}} \cdot \bar{\alpha}^{\mathrm{n}} + \bar{\bar{G}}_{\mathrm{s}} \cdot \bar{J}^{\mathrm{s}} - \bar{E}^{\mathrm{sca}} \right\|^2}{\left\| \bar{E}^{\mathrm{sca}} \right\|^2}. \tag{2.5}$$

And we can call it the field residue. The optimal solution of $\bar{\alpha}^n$ in the least square sense is given by,

$$\bar{\bar{\alpha}}_{\text{opt}}^{\text{n}} = \bar{\bar{A}}^{-1} \cdot \bar{B}, \tag{2.6}$$

where $\bar{\bar{A}} = \left\| \bar{E}^{\text{d}} \right\|^2 [(\bar{\bar{\sim}} P) \cdot \bar{\bar{V}}^{\text{n}}]^* \cdot [(\bar{\bar{\sim}} P) \cdot \bar{\bar{V}}^{\text{n}}] + \left\| \bar{J}^{\text{s}} \right\|^2 (\bar{\bar{P}} \cdot \bar{\bar{G}}_{\text{D}} \cdot \bar{\bar{V}}^{\text{n}})^* \cdot (\bar{\bar{P}} \cdot \bar{\bar{G}}_{\text{D}} \cdot \bar{\bar{V}}^{\text{n}})$,

$\bar{B} = -\left\| \bar{E}^{\text{d}} \right\|^2 [(\bar{\bar{\sim}} P \cdot \bar{V}^{\text{n}})^* \cdot (\bar{\bar{\sim}} P \cdot \bar{J}^{\text{s}})] - \left\| \bar{J}^{\text{s}} \right\|^2 [(\bar{\bar{P}} \cdot \bar{\bar{G}}_{\text{D}} \cdot \bar{V}^{\text{n}})^* \cdot [\bar{\bar{P}} \cdot (\bar{E}^{\text{inc}} + \bar{\bar{G}}_{\text{D}} \cdot \bar{J}^{\text{s}})]$, and the inverse is understood as the pseudoinverse.

The total relative residue is defined to be

$$\Delta^{\text{tot}} = \Delta^{\text{fie}} + \Delta^{\text{sta}}. \tag{2.7}$$

For each of the incidence $\bar{E}_p^{\text{inc}}$, the total relative residue can be calculated as Δ_p^{tot}, $p = 1, 2, \ldots, N_{\text{inc}}$. The vector $\bar{P}$ can be obtained by minimizing the following objective function

$$f(\bar{P}) = \sum_{p=1}^{N_{\text{inc}}} \Delta_p^{\text{tot}} \quad . \tag{2.8}$$

Since we have already represented $\bar{\alpha}^{\text{n}}$ as the function of $\bar{P}$, there is only one unknown argument $\bar{P}$ left in the optimization equation. The steepest descent optimization method is chosen to minimize the objective function Eq.(2.8). Let the initial guess of $\bar{P}$ to be a vector of zeros, i.e., all the line elements in the domain are considered as free space. In each iteration step, we change each element of $\bar{P}$ into its complement and check whether the objective function decreases, and keep the value which gives smaller residue in the objective function. It is worth mentioning that in the objective function, the relative residue in the state equation can be regarded as some kind of regularization term, and thus no additional regularization method is needed in minimizing Eq.(2.8), as has been done in the previous versions of SOM [81].

2.3.2 Numerical Examples

In this section, we give four numerical simulations to validate the algorithm. The domain D is a square of dimension $0.6\lambda \times 0.6\lambda$ and is discretized into 15×15 square cells. In all the figures, the original contour of the PEC is represented in red lines while the other line elements are represented by yellow ones, and the light-blue line with triangle vertex stands for the reconstructed PEC line elements. A total number of $N_{\text{inc}} = 10$ incident waves are evenly distributed in $[0, 2\pi)$, with $\mathbf{k}_p = k(\hat{x}\cos\phi_p + \hat{y}\sin\phi_p),\ p = 1, 2, \ldots, N_{\text{inc}}$. $N_{\text{r}} = 30$ receivers are equally distributed on a circle of radius 5λ. The MoM is used to generate the forward scattering data $\bar{\bar{E}}^{\text{sca}}$, which is recorded in the format of the multistatic response (MSR) matrix with the size of $N_{\text{r}} \times N_{\text{inc}}$. Then white Gaussian noise $\bar{\bar{\kappa}}$ is added to the MSR matrix, and the resultant noisy matrix $\bar{\bar{K}} + \bar{\bar{\kappa}}$ is treated as the measured MSR matrix and is used to reconstruct scatterers. The noise level is quantified by the noise-to-signal ratio defined as $\frac{\| \bar{\bar{\kappa}} \|_F}{\| \bar{\bar{K}} \|_F}$, where $\|\cdot\|_F$ denotes the Frobenius norm of a matrix. The initial guess in the optimization problem is free space, i.e. $\bar{\bar{P}} = 0$. Since the PEC scatterer is impenetrable, it does not change the scattered field whether the internal edges are detected as PEC or air as long as the boundary is correctly detected as PEC. The

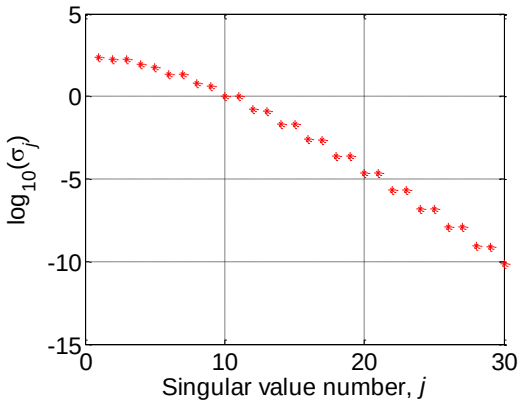

Fig. 2-1. Singular values of the matrix $\overline{\overline{G}}_s$ in all numerical simulations

singular values of $\overline{\overline{G}}_s$ are as shown in Fig. 2-1. The units for the label of coordinates in the reconstruction figures in all simulation results are λ.

Criteria of choosing number of leading singular values

The number of leading singular values, the integer *L*, was found to dominantly affect the performance of SOM for dielectric scatterers [17, 84]. The criteria to determine the value of *L* as in the previous versions of SOM are listed as follows:

1. The value of *L* balances the relative residues in the field equation and in the state equation. The larger the value of *L* is, the smaller is the relative residue in the field equation. However, if the *L* is so large that the relative residue in the field equation is smaller than the noise level, the relative residue in the state equation will be large and cannot be remedied by optimization. On the other hand, a small value of *L* does not produce a non-remediable large relative residue in the state equation, but the simultaneous minimization of both relative residues in the field equation and in the state equation takes longer time to converge.

2. The noise level affects the value of *L*. Generally speaking, the value of *L* in low-noise case is larger than that in high-noise case.
3. An important and encouraging conclusion is that there is a consecutive range of integer *L*, instead of a single value that can be chosen, with different *L* resulting in different convergence speed. Note that this important property means that the value of *L* doesn't critically depend on any other parameter.
4. An empirical method, which is obtained through numerical simulations for various profiles and noise levels, is that unless the noise is very high, a good candidate of *L* takes the value where singular values noticeably change the slope in the spectrum.

Similarly, we can also take the criteria of choosing *L* in dielectric case as a reference to choose the *L* in PEC case.

The first numerical example is a circle with radius 0.15λ located in the middle of the region, as shown in Fig. 2-2(a). Assume the scattered field is obtained without any noise added. From the spectrum of matrix $\overline{\overline{G}}_s$ as shown Fig. 2-1 the value of L is chosen to be 11. After 10 iterations the PEC boundary is reconstructed completely as shown in Fig. 2-2(b), and totally coincides with the original boundary.

In the second numerical example, two squares of side length 0.14λ are located at $(-0.17\lambda, 0.17\lambda)$ and $(0.17\lambda, -0.17\lambda)$, respectively as shown in Fig. 2-3(a). For convenience, we refer to the square on the left as number one and the one on the right as number two. The separation from the right lower corner of square number one to the left upper corner of square number two is about 0.3λ. 10% white Gaussian noise is added to the exact scattering data. The L chosen here is 4 because of the added

noise. After 26 iterations the corresponding contour of the reconstructed pattern is plotted in Fig. 2-3(b). It is clearly seen that the region in between the squares are indentified as free space while there are two rectangular-liked shaped PEC scatterers located around $(-0.17\lambda, 0.17\lambda)$ and $(0.17\lambda, -0.17\lambda)$. The sizes of the reconstructed scatterers are almost the same as the original ones. The result is satisfactory, considering the close distance of scatterers and the presence of 10% noise.

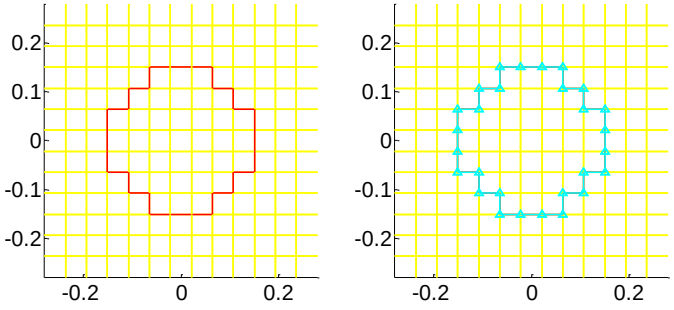

(a) (b)

Fig. 2-2. A circle with radius 0.15λ (a) Exact contour. (b) Reconstructed contour.

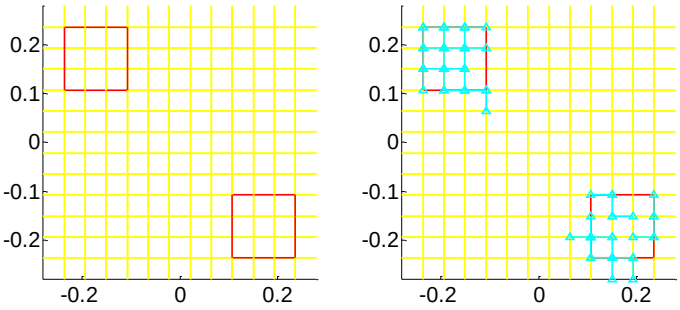

(a) (b)

Fig. 2-3.Two squares separated by 0.3λ (a) Exact contour. (b) Reconstructed contour under 10% white Gaussian noise

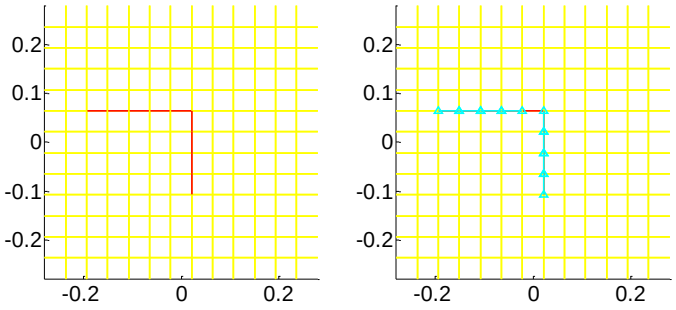

(a) (b)

Fig. 2-4.Single line shaped scatterer (a) Exact contour. (b) Reconstructed contour under 5% white Gaussian noise

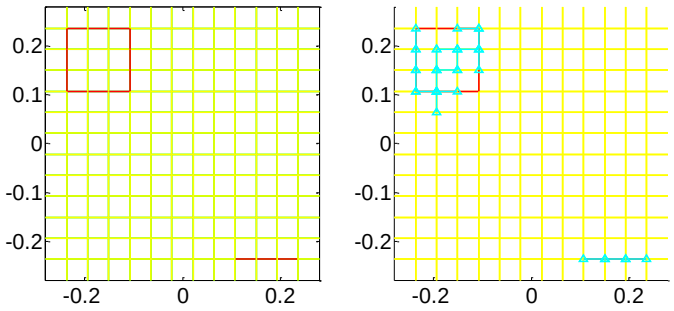

(a) (b)

Fig. 2-5. A combination of a square and a single straight line (a) Exact contour. (b) Reconstructed contour under 10% white Gaussian noise

In the third example we deal with a line-shape scatterer, which resembles an "L" (Fig. 2-4(a)). In presence of 5% noise, we successfully reconstructed the single line with only one segment missing after 16 iterations. And the L chosen here equals to 6.

In the last example, we test the proposed method for reconstructing a combination of a closed-contour scatterer and a line-shape scatterer. A rectangular and a straight line PEC scatterer are located in the domain as shown in Fig. 2-5(a). 10% white Gaussian noise is added. L is chosen to be 4 which is the same as in the second example. After 54 iterations, from the reconstructed figure we can clearly see

that there is a single line and a rectangular shaped scatterer located in the domain with an obvious gap.

2.4 A Continuous Variable Subspace Based Optimization Method

2.4.1 Continuous-type SOM

We notice that the discrete-type SOM suffers from two drawbacks. (1) Although it takes just a few steps of iteration to converge, the computational cost is heavy since there is matrix inversion in each step of iteration. (2) The method is not robust in the sense that the performance of the algorithms depends, in a non-continuous manner, on the number of leading singular values.

To overcome these drawbacks of the discrete-type SOM, we propose a modified version of the SOM. The proposed modified version is different from the discrete-type SOM in the following three aspects: (1) The representation of the unknown is different: In the discrete-type version, the unknown parameter is expressed as a binary vector, whereas in the modified version, the binary unknown is expressed as a function of another unknown that is real and thus continuous. For convenience, we refer to the proposed improved SOM as the continuous-type SOM. (2) The unknowns to be reconstructed are different: The unknown is only a binary vector in the discrete-type SOM, whereas both the indicator of PEC boundary and the contrast current are unknowns in the continuous-type SOM. (3) The optimization solvers are different: The steepest descent optimization method is chosen to minimize the objective function in the discrete-type SOM, whereas the continuous-type SOM uses the alternative two-step CG method, where two types of unknowns (i.e.,

continuous expression of the PEC boundary indicator and the coefficient of contrast current) are alternatively updated and no matrix-inversion is involved in the updating process. The alternative two-step CG optimization method used in our research follows the version developed by SOM [17].

The alternative two-step CG optimization method was proposed to reconstruct dielectric scatterers. The basic idea of the alternative two-step CG optimization method is to construct an objective function and then to minimize the objective function by alternatively updating the contrast and the induced current using the CG. The alternative two-step CG optimization method is an effective inversion method and has been used extensively for synthetic as well as experimental data for acoustic- and electromagnetic-wave problems. However, the alternative two-step CG optimization method cannot be directly applied to deal with PEC scatterer problems in the discrete-type SOM since the unknowns are of binary type.

The difficulty in applying SOM to PEC case lies in constructing the relative residue in the state equation [81]. To overcome this difficulty, we introduce a mathematical parameter $\bar{P}$, an N-dimensional vector, as the indicator of PEC for line elements in the domain of interest. $\bar{P}$ can further be expressed as the function of the variable vector $\bar{x}$,

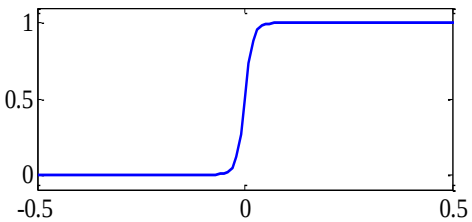

Fig. 2-6. *P* as a function of *x*

$$\bar{P} = \frac{1}{1+e^{-a\bar{x}}} \tag{2.9}$$

where a is a large positive number, such that for each element $x_m, m = 1, 2, \ldots, N$, if $x_m > 0$, $P_m \approx 1$ and if $x_m < 0$, $P_m \approx 0$. The changing trend of the function is depicted as in Fig. 2-6. As in the discrete-type SOM [20], the vector $\bar{P}$ is (approximately) a binary vector, which is used as the indicator of PEC, i.e., a '1' element in $\bar{P}$ represents a PEC element and a '0' element a non-PEC element. The proposed method differs from the previous method by expressing the $\bar{P}$ in Eq.(2.9) as a function of a continuous real variable $\bar{x}$. Thus we can apply the optimization method for such continuous variables so as to solve the PEC inverse scattering problem. A similar idea can be found in [11] and [85], where the binary representation of the scatterer was also approximated into a smooth function and thus the continuous-type optimization was applied.

We are able to construct the relative residue in the state equation as follows,

$$\Delta^{\text{cur}} = \frac{\left\| (\bar{\bar{I}} - \bar{\bar{P}}) \cdot \bar{J} \right\|^2}{\left\| \bar{J}^{\text{s}} \right\|^2} + \frac{\left\| (\bar{\bar{P}}) \cdot \bar{E}^{\text{tot}} \right\|^2}{\left\| \bar{E}^{\text{d}} \right\|^2} \tag{2.10}$$

where $\bar{\bar{P}}$ is the diagonal matrix with $\bar{P}$ in the diagonal, and $\bar{\bar{I}}$ is the identity matrix.

The relative residue in the field equation is the same with the previous version. After we add all the residues for each incidence together, the vector $\bar{P}$ can be obtained by minimizing the following objective function,

$$f(\bar{\alpha}_1^{\text{n}}, \bar{\alpha}_2^{\text{n}}, \ldots, \bar{\alpha}_{N_{\text{inc}}}^{\text{n}}, \bar{x}) = \sum_{p=1}^{N_{\text{inc}}} \left(\frac{\left\| \bar{\bar{G}}_{\text{s}} \cdot \bar{\bar{V}}^{\text{n}} \cdot \bar{\alpha}_p^{\text{n}} + \bar{\bar{G}}_{\text{s}} \cdot \bar{J}_p^{\text{s}} - \bar{E}_p^{\text{sca}} \right\|^2}{\left\| \bar{E}_p^{\text{sca}} \right\|^2} + \frac{\left\| (\bar{\bar{I}} - \bar{\bar{P}}) \cdot \bar{J}_p \right\|^2}{\left\| \bar{J}_p^{\text{s}} \right\|^2} + \frac{\left\| (\bar{\bar{P}}) \cdot \bar{E}_p^{\text{tot}} \right\|^2}{\left\| \bar{E}_p^{\text{d}} \right\|^2} \right)$$

(2.11)

Since the $\bar{P}$ is now expressed as a function of $\bar{x}$, the objective function is now a function of $\bar{\alpha}_p^{\mathrm{n}}$, $p = 1, 2, \ldots, N_{\mathrm{inc}}$ and $\bar{x}$, all of which are unknowns to be optimized. The optimization method we choose is the alternative two-step CG optimization method developed by SOM [17], which is suitable for the continuous-parameter optimization. The optimization procedure of the proposed SOM is implemented as follows:

Step 1: Calculate $\bar{\bar{G}}_{\mathrm{D}}$, $\bar{\bar{G}}_{\mathrm{s}}$ and the SVD of $\bar{\bar{G}}_{\mathrm{s}}$. Obtain $\bar{J}_p^{\mathrm{s}}$, $p = 1, 2, \ldots, N_{\mathrm{inc}}$.

Step 2: Initialization: $n = 0$, set $\bar{x}_0 = 0$, obtain $\bar{\alpha}_{p,0}^{\mathrm{n}}$ from Eq. (2.6) evaluated at $\bar{P}\big|_{\bar{x}_0 = 0}$, and set the search direction $\bar{\rho}_{p,0} = 0$.

Step 3: $n = n + 1$.

Step 3.1: Update $\bar{\alpha}_{p,n}^{\mathrm{n}}$: Calculate gradient (Frechet derivative) $\bar{g}_{p,n} = \nabla_{\bar{\alpha}_p^{\mathrm{n}}} f \big|_{\bar{\alpha}_{p,n-1}^{\mathrm{n}}, \bar{x}_{n-1}}$; Determine the search directions $\bar{\rho}_{p,n} = \bar{g}_{p,n} + \dfrac{\mathrm{Re}[(\bar{g}_{p,n} - \bar{g}_{p,n-1})^* \cdot \bar{g}_{p,n}]}{\left\| \bar{g}_{p,n-1} \right\|^2} \bar{\rho}_{p,n-1}$. Plug $\bar{\alpha}_{p,n}^{\mathrm{n}} = \bar{\alpha}_{p,n-1}^{\mathrm{n}} + d_{p,n} \bar{\rho}_{p,n}$ into the objective function, which is quadratic in terms of $d_{p,n}$, to obtain the parameter $d_{p,n}$ which makes the cost function minimum. Then update $\bar{\alpha}_{p,n}^{\mathrm{n}} = \bar{\alpha}_{p,n-1}^{\mathrm{n}} + d_{p,n} \bar{\rho}_{p,n}$.

Step 3.2: Update $\bar{x}_n$: for the mth line element, $m = 1, 2, \ldots, N$, update induced current $(\bar{J}_{p,n})_m = (\bar{J}_p^{\mathrm{s}})_m + (\bar{\bar{V}}^{\mathrm{n}} \cdot \bar{\alpha}_{p,n}^{\mathrm{n}})_m$. Then update the total field on the mth subunit, $(\bar{E}_{p,n}^{\mathrm{tot}})_m = (\bar{E}_p^{\mathrm{inc}})_m + (\bar{\bar{G}}_{\mathrm{D}} \cdot \bar{J}_{p,n})_m$. The objective function has an analytical derivative with respect to $(\bar{x}_n)_m$ and the optimal solution of $(\bar{x}_n)_m$ is given by

$$(\bar{x}_n)_m = -\frac{1}{a}\ln[\sum_{p=1}^{N_{\text{inc}}} \frac{\left|(\bar{E}^{\text{tot}}_{p,n})_m\right|^2}{\left\|\bar{E}^{\text{d}}_p\right\|^2} \Big/ \sum_{p=1}^{N_{\text{inc}}} \frac{\left|(\bar{J}_{p,n})_m\right|^2}{\left\|\bar{J}^{\text{s}}_p\right\|^2}] \tag{2.12}$$

Step 4: Stop iteration if there is no obvious change in the objective function for continuous three iterations. Otherwise, go to Step 3.

Step 5: Determine binary result $\bar{P}$ from $\bar{x}$: for each element x_m, $m = 1, 2, \ldots, N$, if $x_m > 0$, set $P_m = 1$ and if $x_m < 0$, set $P_m = 0$.

2.4.2 Numerical Examples

In this part, we give several numerical simulations to validate the proposed algorithm. The domain of interest D is a square and is discretized into square cells, the four edges of which are represented by the yellow lines. The contour of the PEC objects located inside the domain of interest is represented in red lines. In all the examples, to avoid the inverse crime [3], the discretization of the computational domain in solving inverse problems is coarser than that in the forward problem. The reconstructed pattern is represented by the light blue lines with triangle vertex.

A total number of $N_{\text{inc}} = 10$ incident waves are evenly distributed in $[0, 2\pi)$. $N_{\text{r}} = 30$ receivers are equally distributed along a circle with radius 5λ. Throughout all simulations, we use $a = 20$ for the parameter $\bar{P}$ in Eq.(2.9). According to our experience, the performance of the algorithm (convergence speed and results) does not sensitively depend on the value of a as long as a is large enough (which will be discussed in Section 2.5.1).

Four numerical simulations will be presented. In the first and third simulations, the computational domain is a square with size of $\lambda \times \lambda$, and the domain in the 2nd

and 4th numerical simulation is $2\lambda \times 2\lambda$, all of which are discretized into 20×20 cells in solving the inverse problem. The units for the label of coordinates in the reconstructed figures are λ. The singular values of matrix $\overline{\overline{G}}_s$ for domain size of $\lambda \times \lambda$ and $2\lambda \times 2\lambda$ are shown in Fig. 2-7 and Fig. 2-8 respectively.

The first numerical example is a circle with radius 0.25λ located in the middle of the region D as shown in Fig.2-9(a). First, we test on the noise-free synthetic data. Analyzing the spectrum of $\overline{\overline{G}}_s$ as shown in Fig. 2-7, the value of L is chosen to be 12, where the slope of the singular value changes dramatically. The reconstructed pattern is shown in Fig.2-9(b), where we see that the reconstruction is successful. Then 100% Gaussian white noise is added to the synthetic data. In this case, L is chosen to be 6 due to the level of the noise. The reconstructed result is shown in Fig.2-9(c), which is quite acceptable considering the 100% noise.

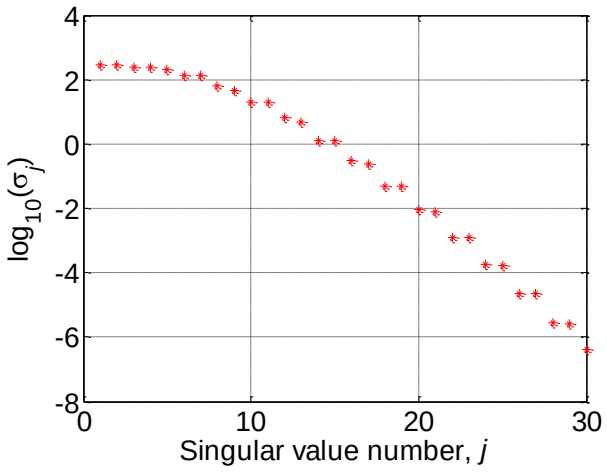

Fig. 2-7. Singular values of the matrix $\overline{\overline{G}}_s$ in the 1st and 3rd numerical simulation.

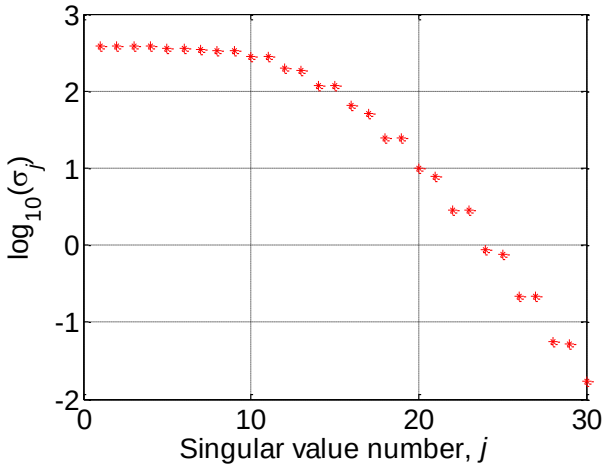

Fig. 2-8. Singular values of the matrix $\overline{\overline{G}}_s$ in the 2nd and 4th numerical simulation.

In the second numerical example, four squares with side length 0.3λ are located at the four corner of the $2\lambda \times 2\lambda$ domain, as shown in Fig. 2-10(a). With noise-free synthetic data and $L = 12$, according to Fig. 2-8, the reconstructed result is plotted in Fig. 2-10(b). It is clearly seen that the region in between the squares are indentified as free space while there are four rectangular-liked shaped PEC scatterers located at four corners of the domain. The sizes of the reconstructed scatterers are almost the same as the original ones. Then 50% Gaussian white noise is added into the scattered field and $L = 8$. The reconstructed result is plotted in Fig. 2-10 (c). We see that the four squares are satisfactorily identified.

In the third example, we use a line-shape PEC object, a reversed 'L', as shown in Fig. 2-11(a). Fig. 2-11 (b) is the reconstructed result with noise-free data and $L = 12$. Fig. 2-11 (c) shows the reconstructed result when 10% Gaussian white noise is added and $L = 10$. These results show that the proposed algorithm is able to reconstruct the line-shape PEC scatterer.

In the fourth example, we test the proposed method for reconstructing a combination of a closed-contour scatterer and a line-shape scatterer. A rectangular and a line-shaped PEC scatterer are located in the domain as shown in Fig. 2-12(a). Fig. 2-12 (b) shows the reconstructed result by using noise-free data and choosing $L=12$ while Fig. 2-12 (c) for the case with 10% noise and $L=10$. From the reconstructed results we clearly see that there is an 'L' shaped scatterer and a rectangular scatterer located in the domain.

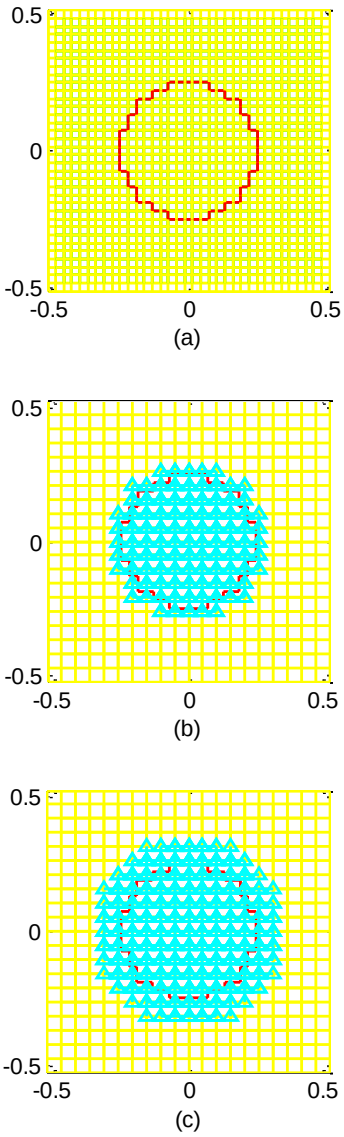

Fig.2-9. A circle with radius 0.25λ (a) Exact contour. (b) Reconstructed contour with noise-free synthetic data. (c) Reconstructed contour under 100% white Gaussian noise.

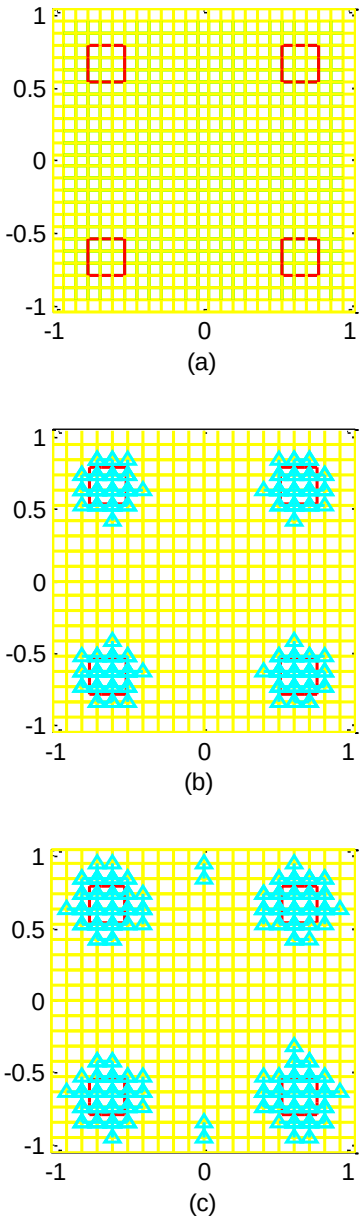

Fig. 2-10. Four separated squares (a) Exact contour. (b) Reconstructed contour with noise-free data. (c) Reconstructed contour under 50% white Gaussian noise.

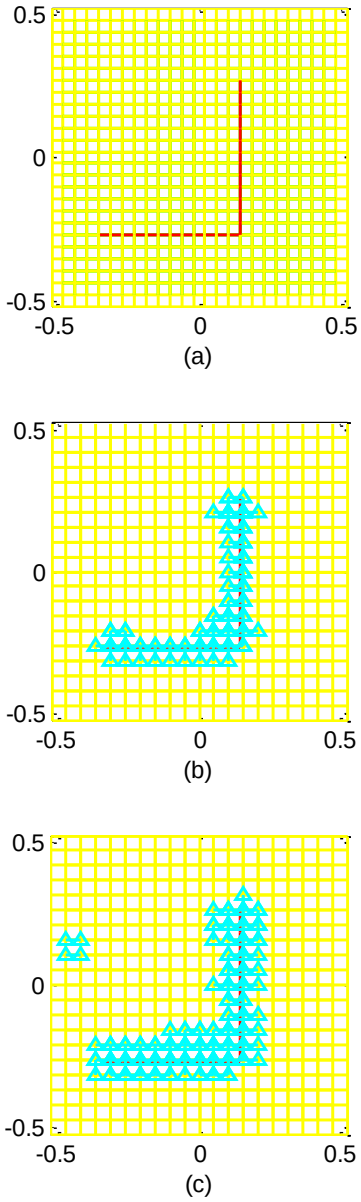

Fig. 2-11. A reversed ‘L’ shape PEC scatterer (a) Exact contour. (b) Reconstructed contour with noise-free data. (c) Reconstructed contour under 10% white Gaussian noise.

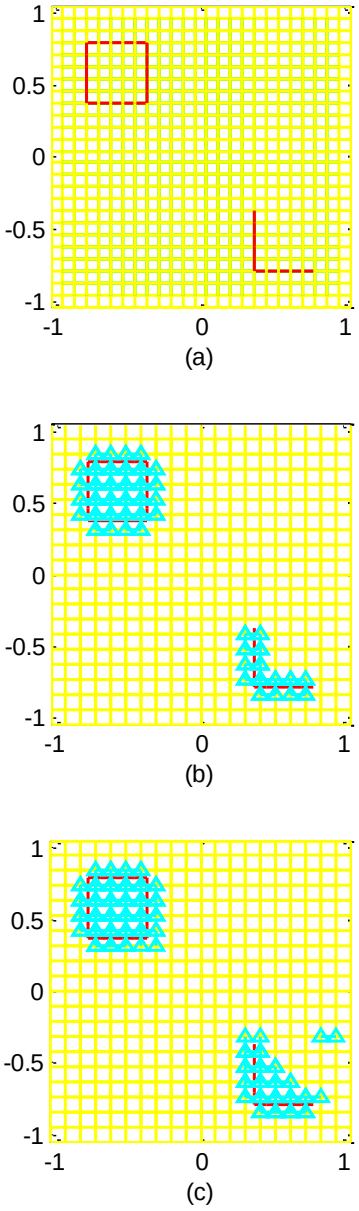

Fig. 2-12. Both the closed-contour and line shape PEC scatterers. (a) Exact contour. (b) Reconstructed contour with noise-free data. (c) Reconstructed contour under 10% white Gaussian noise.

2.5 Discussion

2.5.1 Investigation of the optimization progress for continuous-type SOM

A. Coefficient *a*

The coefficient a is a large positive number to make $\bar{P}_i,\ \ i=1,2,\ldots,N$ as a function of $\bar{x}_i,\ \ i=1,2,\ldots,N$ behave approximately as a step function. The influence of a on the shape of the function is plotted in Fig. 2-13. It is clear that the larger a is, the faster $\bar{P}_i$ changes from 0 to 1 when $\bar{x}_i$ approaches from negative to positive numbers.

We aim to investigate the influence of coefficient a on the optimization process. The numerical setup of the experiment is just the same as the first example in the Section 2.4.2: a circle with radius 0.25λ is located in the middle of the domain of size $\lambda\times\lambda$ and no noise is added. Different values of a are chosen. The time used for 400 iteration steps and the values of the objective function in the 400^{th} iteration step are listed in Table 2-1 . No significant change of the convergence speed is observed and the objective function values are almost the same for different values of a. Therefore, the optimization does not sensitively depend on the value of a as long as a is large enough.

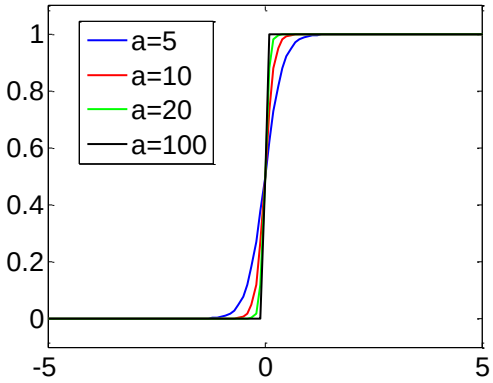

Fig. 2-13. P as a function of a

Table 2-1 Effect of a to the optimization process

	Time used for 400 iteration(s)	**Objective function value**
a=5	103.075261	0.0018257
a=10	102.283269	0.0018257
a=20	100.852451	0.0018257
a=100	100.678244	0.0018257

B. The investigation of the filled-up parts inside the scatterer

From Eq.(2.10) the residue in state equation, we see that the diagonal matrix $\bar{\bar{P}}$ complimentarily restricts the two terms $\bar{J}$ and $\bar{E}^{\text{tot}}$ to be zero. It can be explicitly seen from the state residue that when there is a zero valued total electric field there is non-zero valued induced current, which in fact happens at the boundary of PEC scatterer. However the state residue has no explicit requirement on the induced currents that are in the interior of the scatterer.

In addition, an interesting phenomenon can be seen from the reconstructed patterns in continuous-type SOM: when the boundary of the unknown object is correctly recognized, the interior of each scatterer is also filled up by PEC elements or recognized as '1' elements in the retrieved $\bar{\bar{P}}$. Since the PEC scatterer is impenetrable, it does not change the scattered field no matter the internal edges are

detected as PEC or air as long as the boundary is correctly detected. However, further investigation is needed to theoretically explain this phenomenon. We aim to see what happens to the electric field and induced current on these "filled-up" edges.

The numerical set up is same as the first example in Section 2.4.2: as shown in Fig. 2-14 (a), one circle with the radius of 0.25λ is located in the center of the domain of interest with size $\lambda \times \lambda$ and the domain is discretized into 20×20 cells. No noise is contained in the scattered field and $a = 20$. The red bars in figures represent the exact contour of the objects and yellow bars represent the side edges of square mesh. Light blues bars with triangle vertex stand for the reconstructed PEC line elements. The setups of transmitters and receivers are the same as all the numerical examples in the previous section.

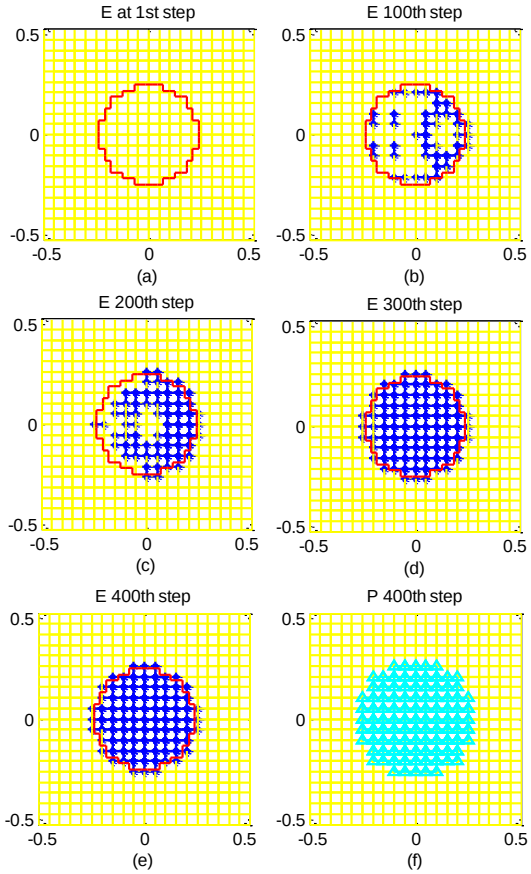

Fig. 2-14. Red bars represent the exact contour of objects and yellow bars represent the side edges of square mesh. Dark blue bars with star vertex represent bars with zero electric field and light blue bars represent '1' elements in $\bar{P}$. (a) ~ (e) The total electric field for each step of iteration. (f) The reconstruction pattern for $\bar{P}$.

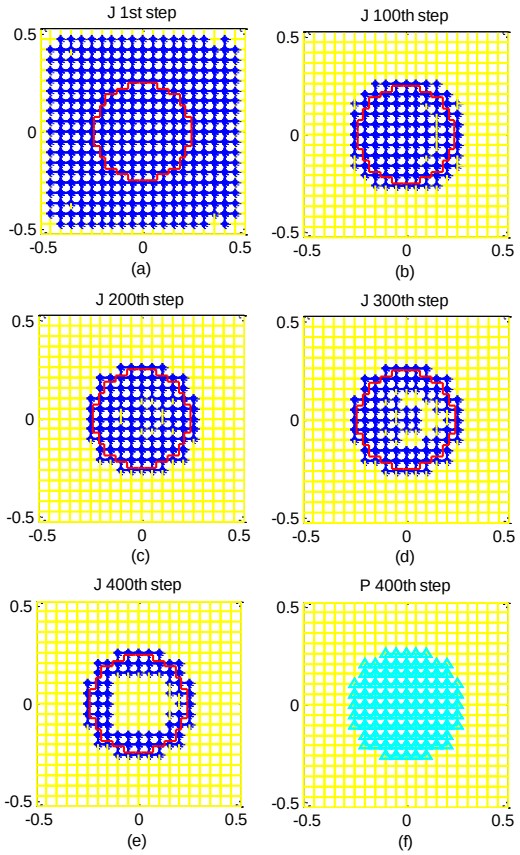

Fig. 2-15. Red bars represent the exact contour of objects and yellow bars represent the side edges of square mesh. Dark blue bars with star vertex represent bars with non-zero induced current and light blue bars represent '1' elements in $\bar{P}$. (a) ~ (e) The induced current for each step of iteration. (f) The reconstruction pattern for $\bar{P}$.

In Fig. 2-14(a) ~ (e), we pick out the line elements with 'zero' electric field along with the iteration steps and observe the trend of changing in $\bar{E}^{\text{tot}}$. The criterion is that if the magnitude of the total electric field on a line element is smaller than 1/200 of the magnitude of the incident field, it will be approximately considered to be zero. The line elements on which the total electric fields equal to zero are represented by the dark blue bars with star vertex in Fig. 2-14. As a comparison to the final result, in Fig. 2-14 (f) we give out the reconstruction pattern at the 400th iteration step, where the light blue bars with triangle vertex represent the edge with '1' element in

vector $\bar{P}$. From Fig. 2-14 (b) ~ (e), we observe that the total electric field inside the scatterer is approaching to zero gradually.

In Fig.2-15(a) ~ (e), we pick out the line elements with 'non-zero' induced current along with the iteration steps and observe the trend of changing in $\bar{J}$. The criterion is that if the magnitude of the induced current density on a line element is bigger than 1/100 of the average magnitude of induced current density throughout the domain, the current density on this line element will be considered as non-zero. The line elements on which the induced currents with non-zero values are picked out, and are represented by the dark blue bars with star vertex in Fig.2-15. As a comparison to the final result, in Fig.2-15 (f) we give out the reconstruction pattern at the 400th iteration step. From Fig.2-15 (a) ~ (e), we observe that the current density is gradually becoming the surface current around the boundary.

Therefore, even though the interior of the scatterer is filled up, i.e., the corresponding elements are recognized as '1' in $\bar{\bar{P}}$, the boundary condition is still satisfied and the products of $(\bar{\bar{P}})\cdot\bar{E}^{\text{tot}}$ and $(\bar{\bar{I}}-\bar{\bar{P}})\cdot\bar{J}$ are negligibly small. Thus the influence of the filled up part of scatterer to the objective function is negligible. It does not matter whether the optimization fills up the inside of the scatterer or not. Since the PEC scatterer is impenetrable, it does not change the scattered field no matter the internal edges are detected as PEC or air as long as the boundary is correctly detected.

2.5.2 The investigation of regularization term for continuous-type SOM

After we express the binary vector $\bar{P}$ into function of $\bar{x}$, the alternative two-step CG optimization method is applied to solve the continuous-type optimization problem. The optimization coefficients behave in a continuous manner. There is no need to choose a best value of *L* in the proposed continuous-type SOM, and there is a successive range of integer value of *L* that can be chosen to ensure a successful reconstruction.

For instance, a square with a side length of 0.8λ is located inside the domain of size $2\lambda \times 2\lambda$ as shown in Fig. 2-17(a). 10% noise is added to the exact scattered field. The convergence trajectories in the first 300 iterations for different values of L are shown in Fig. 2-16. There exists a range of L, from 3 to 17, which can be used to reconstruct the PEC scatterer successfully. However, if L is too large or too small, the optimization fails to converge to the wanted solution. The reconstructed pattern after 300 iterations for the different value of L is shown in Fig. 2-17 (b) to (f). From these results, we see that, in $L=1$ case, the optimization fails to converge to a good result, and this is due to the fact that the information in the deterministic part of the induced current is not enough so that the optimization converges in a very slow way. As the value of L increases, for the cases $L=3$ to $L=17$, the convergences of the optimizations are similar to each other, as shown in Fig. 2-16. Besides, we also see there is no much difference between the reconstructed results, such as for $L=6$ and $L=11$ cases shown in Fig. 2-17. However, if we further increase the value of L to 20 or even higher, 25, the noise in the deterministic part of the induced current spoils

the optimization and there are some unwanted disturbances shown in the reconstructed results, as shown in Fig. 2-17. Such phenomenon is accordance with the one for the dielectric scatterers case mentioned in Section 2.3. Therefore the continuous-type SOM for PEC is robust in choosing the regularization parameter L.

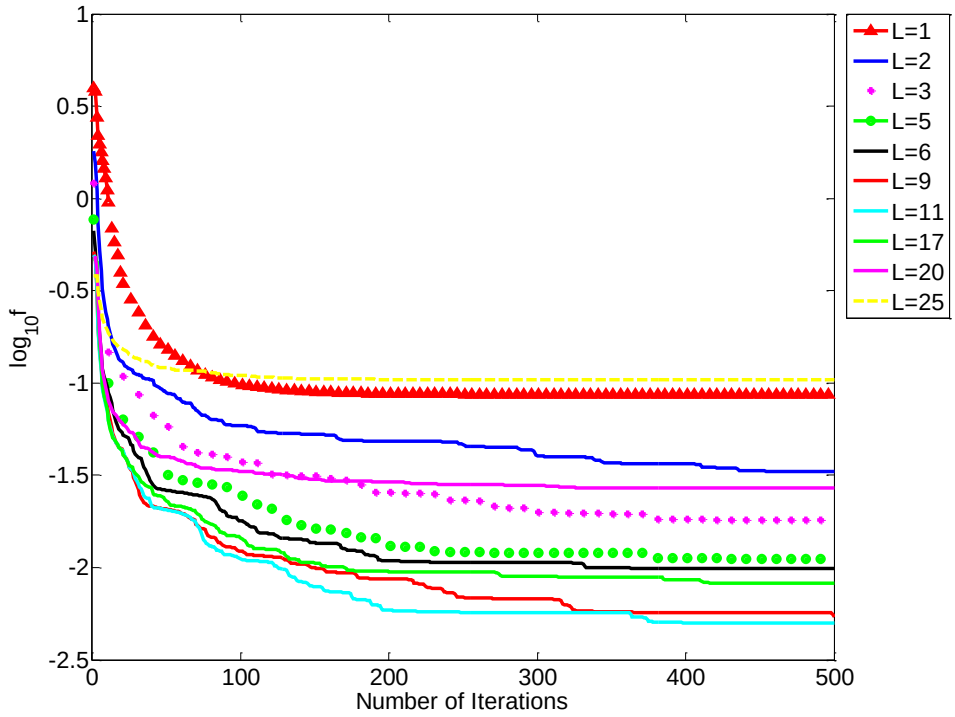

Fig. 2-16. The convergence trajectories in the first 300 iterations for different values of L

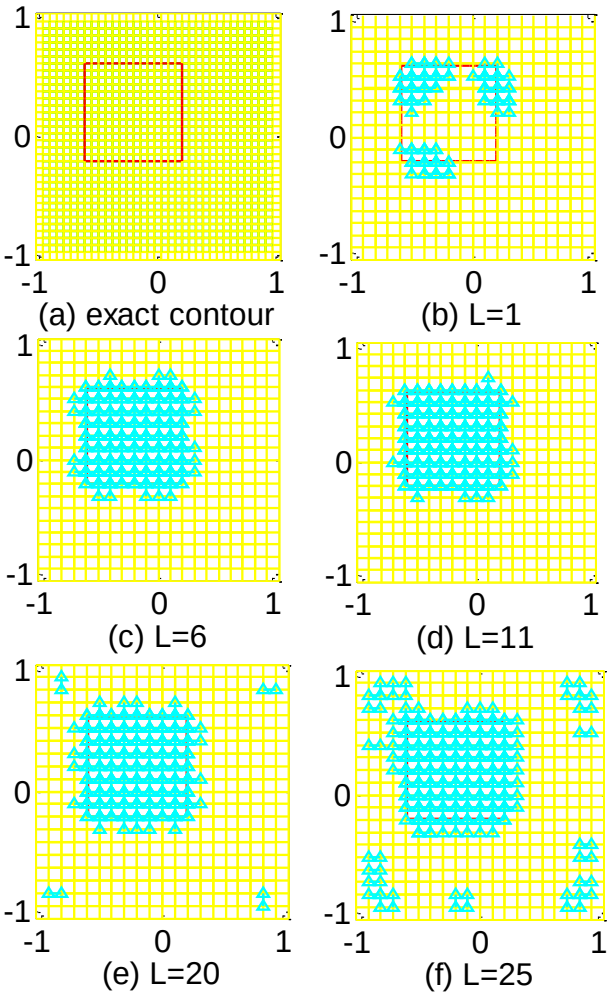

Fig. 2-17. The reconstruction pattern for different values of L

2.5.3 The Comparison of discrete-type SOM and continuous-type SOM

A. Comparison of the computing time

The steepest descent optimization method used in the discrete-type SOM needs matrix inversion to calculate the searching direction, so that the computational cost is high and the speed for each iteration step is quite slow. On the other hand, the descent method searches for the steepest descent direction such that it takes fewer steps of iteration to converge. The continuous-type SOM finds searching direction using the CG, which does not involve any matrix-inversion and alternatively updates the vector $\bar{x}$ and the unknown coefficient $\bar{\alpha}^{n}$. The speed for each iteration step is much faster than the original version, but it takes more iteration steps to converge.

For example, we compare the computational time for the discrete-type SOM and continuous-type SOM under the same experimental set up as indicated in the first numerical example in Section 2.4.2, in which no noise is added and $L=12$. When the objective function is minimized to be 0.0027 in the 46th iteration, the time used in the discrete-type SOM is around 8900 seconds CPU time. While the continuous-type gets a 0.0018 in only 100.8 seconds CPU time after 400 iterations. The average time used for one step of iteration is only 0.252 second for the continuous-type SOM, while the discrete-type SOM uses around 193 seconds for each step of iteration. The reconstructed patterns for both methods are in Fig. 2-18. Thus even at a cost of more iteration steps, the total time used for the continuous-type SOM is still much less than the one used by the discrete-type SOM. Continuous-type SOM is more time saving than the discrete-type SOM.

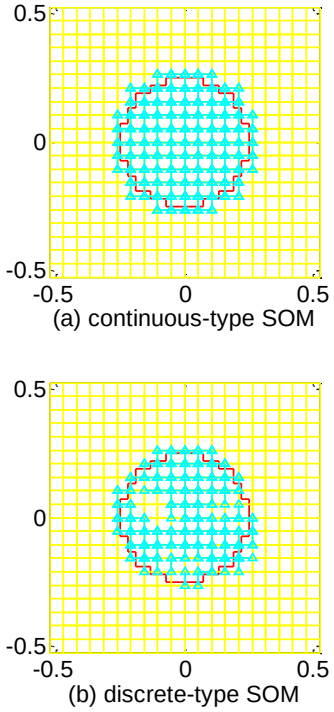

Fig. 2-18. Reconstructed pattern for both SOM methods, $L=12$ (a) continuous-type SOM. (b) discrete-type SOM.

B. Comparison of the regularization term

In the discrete-type SOM, the vector $\bar{P}$ is a binary vector, and the optimization method is chosen as the steepest descent optimization. In various numerical simulations, we notice the following problems associated with the binary-type optimization. First, the performance of the algorithm depends, in a non-continuous manner, on the number of leading singular value L. Thus, in practice, to implement the binary-type SOM, we have to try several different values of *L*. Second, in some simulations, we observe that the optimization method is trapped at a cyclic solution, i.e., the solution cyclically repeats itself during the optimization iterations. This is a typical problem in binary optimization problems.

In comparison, these two problems do not present in the proposed continuous-type SOM. The essence of the continuous-type SOM is to introduce the binary vector $\bar{P}$ as well as to express it into a continuous form and then to apply the alternative two-step CG optimization method. As shown in Section 2.5.2, the regularization term behaves smoothly in optimization.

For example, we compare the optimization process for the discrete-type SOM and continuous-type SOM under the same experimental set up as indicated in the first numerical example in Section 2.4.2, in which no noise is added. Then in Fig. 2-19 and Fig.2-20, we draw the convergence trajectories of a consecutive range of $L = 8 \sim 10$ for discrete-type SOM and continuous-type SOM respectively. We can observe in continuous-type SOM, the optimization converge smoothly and consecutive values of L behave almost the same. While in discrete-type SOM, the optimization fluctuates

severely and sometimes traps into local minimum. Consecutive values of L have totally different convergence behaviors. Therefore in continuous-type SOM, it is always safe to choose from a consecutive range of L and the cost function is always dropping in optimization. Continuous-type SOM is more robust than the discrete-type SOM.

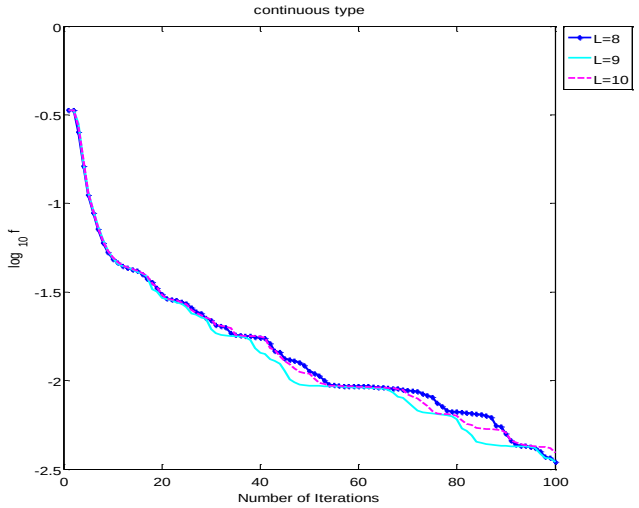

Fig. 2-19 Continuous-type SOM: Convergence trajectories in the first 100 iterations for different values of L

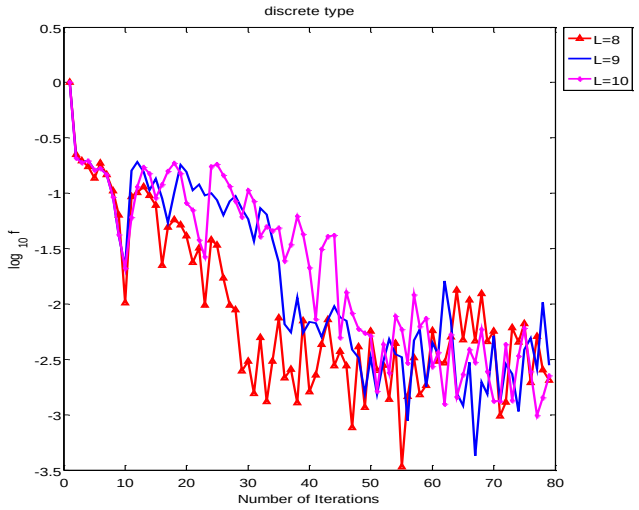

Fig.2-20 Discrete-type SOM: Convergence trajectories in the first 100 iterations for different values of L

2.6 Summary

In this chapter, we have investigated the reconstruction of PEC scatterers of arbitrary number and arbitrary shapes, without requiring *a priori* information on the number of the scatterers and their approximate locations. In addition, both closed-contour and line-shape scatterers are considered in the inverse scattering problem. The background medium, together with scatterers is effectively expressed as a vector that enables to construct the objective function. The discrete-type SOM succeeded in reconstructing the PEC objects. The continuous expression of the PEC indicator enables the application of alternative two-step CG optimization method into the optimization in solving the inverse problem. Numerical simulations conducted in two dimensional geometry show that the continuous-type SOM works well for the PEC inverse scattering problem and is more robust and more computationally economic than the discrete-type version.

3 THE INVERSE SCATTERING PROBLEM OF MIXED BOUNDARY SCATTERERS

In this chapter, a *T*-matrix SOM is proposed to solve inverse scattering problem of reconstructing a mixture of PEC and dielectric scatterers, under the two dimensional TM incidence setting. Both the dipole and monopole elements of the *T*-matrix are retrieved directly and the monopole element of *T*-matrix is used to distinguish the PEC from dielectric scatterer. Numerical simulations validate the proposed method, showing that it works well in sub-wavelength setting and is quite robust against noise.

3.1 Introduction

The inverse scattering problem has been studied for decades and the methods have already been well developed for either dielectric scatterer [32, 86] or PEC [87, 88]. The modeling scheme in inverse scattering problem is often based on the EFIE [80]. The dielectric scatterer problem is solved by volumetric model [17, 22, 81], while the PEC scatterer problem is commonly solved by surface model due to different boundary conditions [20, 21, 70, 87, 89]. However in inverse problem, the properties of scatterers are unknowns to be solved such that it is quite difficult to reconstruct the PEC and dielectric scatterers together under the EFIE model. One solution is to use complex relative permittivity representing both PEC and dielectric scatterers [60, 61]. The PEC scatterer is approximated by lossy dielectric scatterer and

distinguished by the larger imaginary permittivity. However the reconstructed PEC scatterer is not significantly different from lossy dielectric scatterers.

In this Chapter, we will employ the *T*-matrix method to model the scattering behavior of the mixed boundary problem. The *T*-matrix method was firstly developed by Waterman in 1965 [50]. The scattered and incident fields are firstly expanded as functions of multipoles, and then scattered field coefficient is related to the incident field coefficient by *T*-matrix only utilizing the boundary condition. Different kinds of scatterers have different valued *T*-matrices. Thus, the *T*-matrix method provides a possibility of solving the mixed boundary problem. In this chapter, the SOM [17, 20, 21] is applied to the *T*-matrix method to solve the mixed boundary problem consisted of both the PEC and dielectric scatterers of arbitrary number and shape. We refer to this newly developed method as the *T*-matrix SOM.

The proposed method shares several similarities with the original SOM [17] in following aspects: 1) Both *T*-matrix SOM and the original SOM study the spectral property of the linear mapping from the induced current/ amplitude of the induced multipole to the scattered field. Then the unknown vectors are decomposed into two parts---the deterministic part which is uniquely determined by this mapping as well as the scattered field, and the ambiguous part which is solved via optimization. 2) The structures of the cost functions for both methods are similar, both of which are composed by the residue of the field equation and the residue of the state equation. 3) The method of choosing the singular value truncation number L in the original SOM is also applicable to the new *T*-matrix SOM.

The proposed method differs from the original SOM in the following aspects: 1) In the original SOM, we analyze the singular value spectrum of the mapping from induced current in the domain to the scattered field. While in the *T*-matrix SOM, we analyze the singular value spectrum of the mapping from the amplitude of the induced multipoles to the scattered field. 2) In the original SOM, the relative permittivity is the unknown physical parameter representing the dielectric scatterer [17, 22] and a binary type vector is the unknown mathematical parameter to represent the PEC scatterer [20, 21]. In comparison, in the *T*-matrix SOM, the *T*-matrix is the unknown physical parameter and both the PEC and dielectric scatterers can be represented as *T*-matrix. 3) The number of unknowns in the original SOM equals to the number of subunits inside the domain. The number of unknowns in *T*-matrix SOM equals to the number of subunits inside the domain multiplied by the number of multipoles chosen for representing the scattered field in each subunit.

The improvement of the proposed method compared to the original *T*-matrix inverse method is as follows. Chew and others have developed a *T*-matrix based inverse scattering method, for either the PEC case [62] or the dielectric scatterer case [51, 54]. However, as *a priori* knowledge, scatterers are known to be perfectly conducting in [62] and to be dielectric in [51, 54]. Thus, only single leading multipole term is used in the modeling in these three papers. To be specific, only the monopole term is used in [62] to model the scattering of PEC scatterers for 2D E_z incidence, whereas only the dipole term is used to model the scattering of dielectric scatterers for 2D H_z incidence [54] and 3D case [51]. In our research, we consider a mixture of two

kinds of scatterers for 2D E_z incidence. It is stressed that although the monopole term is leading for both PEC and dielectric scatterers individually, it is inaccurate to use only monopole term to model the scattering behavior for a mixture of two kinds of scatterers, due to the fact that dipole term of PEC scatterer is comparable in magnitude to the monopole term of dielectric scatterer. In this thesis, we use both the monopole and dipole terms for both types of scatterers to describe the field, which is more accurate for the mixed boundary case.

In [54], *T*-matrix is approximated by small term polynomial during optimization, and the relative permittivity is retrieved directly from optimization. In comparison, in our method the *T*-matrix (without approximation) for both PEC and dielectric is directly solved for via optimization, and then another optimization is needed to retrieve the relative permittivity from the *T*-matrix, which is more accurate compared to directly solving the relative permittivity from the approximated polynomial. Other advantages of the two-step optimization are that: the first step uses the alternative two-step CG optimization method [17] which avoids the time consuming matrix inversion during the optimization; moreover, a reasonably good initial guess for the second step drastically increases the speed of convergence so that the univariate optimization problem in this step is straightforward.

In [62] the PEC scatterer is known as *a priori* knowledge. A LSF proportional to the exact PEC *T*-matrix is assigned to each subunit during reconstruction. In our method, the monopole element in *T*-matrix of each subunit works similarly as the LSF.

However it is used to classify the PEC scatterers from the dielectric ones. No *a priori* information is needed in classifying these two kinds of scatterers.

The main contributions of the proposed *T*-matrix SOM are: Firstly, the PEC and dielectric scatterers are reconstructed simultaneously by the *T*-matrix method, without *a priori* information on the property or number and shape of scatterers. Secondly, the SOM has been applied in the framework of *T*-matrix method by analyzing the linear mapping from the amplitude of the induced multipole to the scattered field, showing that the SOM is not limited to using the linear mapping from induced current to scattered field. Thirdly, various numerical simulations show that the proposed *T*-matrix SOM inherits good properties of the original SOM, i.e., fast convergence, robust against noise, and high-resolution imaging ability.

3.2 Forward Solution for Mixture of PEC and Dielectric Scatterers

We consider the inverse scattering problem in a two dimensional setting under the TM time harmonic illuminations. The setup of this problem is depicted as in Fig.

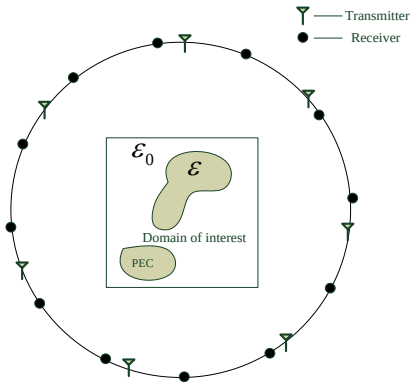

Fig. 3-1 The geometry for inverse scattering measurements: the dielectric scatterer with permittivity ε and the PEC scatterer coexist in the domain of interest.

3-1.

Suppose the unknown scatterers are located inside a domain of interest $D \subset R^2$. The background is air and k_0 denotes the wave number in free space. A total number of N_{inc} unit plane waves that are evenly distributed around a circle impinge on the domain. The scattered field is received by N_{r} antennas, which are symmetrically located around a circle. Thus there are totally $N_{\text{r}} \times N_{\text{inc}}$ points of data recorded in the scattered field matrix. The whole domain of interest is discretized into square meshes with N subunits and in numerical simulations the scattering behavior of each cell can be well approximated by a circle of the same area such that the analytical form of *T*-matrix [52] can be used. The equivalent radius of each subunit is R and the centers are located at $\boldsymbol{\rho}_i = (r_{0,i}, \theta_{0,i})$, $i = 1, 2, \ldots, N$, under the global coordinate system.

Applying the multipole expansion to both the incident field and the scattered field under local coordinate of the ith sub-unit [52], we get the total field,

$$E_z^{\text{tot}}(\mathbf{r}_i) = \mathbf{Rg}\boldsymbol{\psi}^{\text{t}}(k_0, \mathbf{r}_i) \cdot \mathbf{e}_i + \sum_{j=1}^{N} \boldsymbol{\psi}^{\text{t}}(k_0, \mathbf{r}_j) \cdot \mathbf{a}_j, \quad i = 1, 2, \ldots, N. \tag{3.1}$$

On the right hand side, the first term is the incident field on the ith subunit and the second term indicates the scattered field from all the subunits. The observation point is at $\mathbf{r}$ with respect to the global coordinate and $\mathbf{r}_i = \mathbf{r} - \boldsymbol{\rho}_i$ is the observation point under the local coordinate of the ith sub-unit, where $\mathbf{r}_i = (r_i, \phi_i)$, $i = 1, 2, \ldots, N$. $\left[\boldsymbol{\psi}^{\text{t}}(k_0, \mathbf{r}_i)\right]_m = H_m^{(1)}(k_0 r_i) e^{\text{i}m\phi_i}$, and $\mathbf{Rg}$ stands for the regular part, i.e., $\left[\mathbf{Rg}\boldsymbol{\psi}^{\text{t}}(k_0, \mathbf{r}_i)\right]_m = J_m(k_0 r_i) e^{\text{i}m\phi_i}$, $m = -M, \ldots, M$. M is the truncation number of multipoles [53]. Here $\mathbf{a}_j$, $j = 1, 2, \ldots, N$ are referred to as the vectors of amplitude of

the induced multipole. The explicit form of $\mathbf{e}_i$ is $[\mathbf{e}_i]_m = \mathrm{i}^m e^{\mathrm{i}k_0 r_{0,i}\cos(\theta_{0,i}-\theta_{\mathrm{inc}})} e^{-\mathrm{i}m\theta_{\mathrm{inc}}}$, where θ_{inc} is the angle that the incident wave number makes with the x-axis.

To obtain the scattered field $\mathbf{E}_z^{\mathrm{sca}}$ received on the antennas, the total incident field on the ith subunit can be expressed as the summation of the incident field and the multiple scattered fields from other subunits. We can split Eq.(3.1) into the total incident field on the ith subunit (the first two terms in Eq.(3.2)) and the scattered field on the ith subunit.

$$E_z^{\mathrm{tot}}(\mathbf{r}_i) = \mathbf{Rg}\boldsymbol{\psi}^{\mathrm{t}}(k_0,\mathbf{r}_i)\cdot\mathbf{e}_i + \sum_{\substack{j\neq i\\ j=1}}^{N} \boldsymbol{\psi}^{\mathrm{t}}(k_0,\mathbf{r}_j)\cdot\mathbf{a}_j + \boldsymbol{\psi}^{\mathrm{t}}(k_0,\mathbf{r}_i)\cdot\mathbf{a}_i. \tag{3.2}$$

The translational addition theorem enables one to represent the scattered field from other scatterers as a form of the incident field to one scatterer. $\boldsymbol{\psi}^{\mathrm{t}}(k_0,\mathbf{r}_j) = \mathbf{Rg}\boldsymbol{\psi}^{\mathrm{t}}(k_0,\mathbf{r}_i)\cdot\bar{\bar{\alpha}}_{ij}$ (Appendix I). After some derivation by using the addition theorem we get,

$$\mathbf{a}_i = \bar{\bar{T}}_i[\mathbf{e}_i + \sum_{\substack{j=1\\ j\neq i}}^{N} \bar{\bar{\alpha}}_{ij}\cdot\mathbf{a}_j], \quad i = 1,2,\ldots,N, \tag{3.3}$$

where $\bar{\bar{\alpha}}_{ij}$ is the translational matrix. $\bar{\bar{\alpha}}_{ij}(m,n) = H_{m-n}^{(1)}(kd_{ij})e^{-i(m-n)\phi_{ij}}$, where d_{ij} is the distance between the ith and jth subunit and ϕ_{ij} is the angle of the jth subunit under the local coordinate of the ith subunit. $\bar{\bar{T}}_i$ is the T-matrix of the ith subunit which relates the total incident field coefficient to the amplitude of the induced multipole. For a dielectric subunit, the T-matrix can be calculated by [52],

$$[T]_m = \frac{\sqrt{\varepsilon_{\mathrm{r}}}J_m(k_0R)J_m'(\sqrt{\varepsilon_{\mathrm{r}}}k_0R) - J_m(\sqrt{\varepsilon_{\mathrm{r}}}k_0R)J_m'(k_0R)}{H_m^{(1)\prime}(k_0R)J_m(\sqrt{\varepsilon_{\mathrm{r}}}k_0R) - \sqrt{\varepsilon_{\mathrm{r}}}J_m'(\sqrt{\varepsilon_{\mathrm{r}}}k_0R)H_m^{(1)}(k_0R)}, \quad m = -M,\ldots,M. \tag{3.4}$$

And for a PEC subunit,

$$[T]_m = -\frac{J_m(k_0 R)}{H_m^{(1)}(k_0 R)}, \quad m = -M, \ldots, M \,. \tag{3.5}$$

Combining the N equations for all the subunits into one matrix equation, we then obtain amplitude of the induced multipole as,

$$\bar{\mathbf{a}} = [\hat{O} \cdot \bar{\bar{A}} + \bar{\bar{I}}]^{-1} \cdot \hat{O} \cdot \bar{\mathbf{e}} \,, \tag{3.6}$$

where $\bar{\mathbf{a}}$ is an $N(2M+1)\times 1$ dimension vector consisting of $\mathbf{a}_i, i = 1, 2, \ldots, N$ along its column and $\hat{O}$ is a square matrix of size $N(2M+1)\times N(2M+1)$, with the *T*-matrices for each subunit being arranged along its diagonal and zeros being in off-diagonal. Matrix $\bar{\bar{A}}$ is the combination of translational matrices where $[\bar{\bar{A}}]_{ij} = -\bar{\bar{\alpha}}_{ij}$ for $i \neq j$ and zero otherwise. $\bar{\mathbf{e}}$ is an $N(2M+1)\times 1$ column vector consisting of $\mathbf{e}_i, i = 1, 2, \ldots, N$ along its column. Eq.(3.6) is referred to as the state equation, similar to [17]. Note that in [17] the state equation is composed by the induced current while Eq.(3.6) is composed by amplitude of the induced multipole $\bar{\mathbf{a}}$.

The scattered field on the antennas can be solved by,

$$\mathbf{E}_z^{\mathbf{sca}} = \sum_{j=1}^{N} \boldsymbol{\psi}^{\mathrm{t}}(k_0, \mathbf{r}_j) \cdot \mathbf{a}_j = \bar{\boldsymbol{\psi}}^{\mathrm{t}} \cdot \bar{\mathbf{a}} \,. \tag{3.7}$$

Eq.(3.7) is referred to as the field equation.

3.3 The Inverse Problem for Mixture of PEC and Dielectric Scatterers

3.3.1 *T*-matrix SOM

Two steps of optimization processes are involved in the inverse scattering problem. The first process is to retrieve the *T*-matrices or matrix $\hat{O}$ from the given

scattering data. The retrieved monopole element of the *T*-matrix works as the classification of the PEC scatterers from the dielectric ones. The second optimization consists of retrieving the relative permittivity of the dielectric scatterers, which is a univariate optimization problem at each subunit.

A. The *T*-matrix SOM

The essence of SOM lies in that it decomposes the induced current into two orthogonally complementary parts: the deterministic part and the ambiguous part, by doing SVD to the mapping from induced current in domain to the field on receivers. To reconstruct the induced current, the optimization is carried out in a smaller subspace of the current space in SOM.

Similarly, we can also apply the SOM to the *T*-matrix method. The matrix $\bar{\bar{\boldsymbol{\psi}}}^{\mathrm{t}}$ of dimension $N_{\mathrm{r}} \times (2M+1)N$ in Eq.(3.7) refers to the mapping from amplitude of the induced multipole $\bar{\mathbf{a}}$ to the scattered field on the receivers. $\bar{\bar{\boldsymbol{\psi}}}^{\mathrm{t}}$ is defined uniquely by the domain of interest and the positions of the receivers. It works in a way similar to the $\bar{\bar{G}}_{\mathrm{S}}$ as in the original SOM [17].

We do SVD to $\bar{\bar{\boldsymbol{\psi}}}^{\mathrm{t}} = \bar{\bar{U}} \cdot \bar{\bar{\Sigma}} \cdot \bar{\bar{V}}^{*}$. After analyzing the spectrum of singular values, the deterministic part of $\bar{\mathbf{a}}$ is uniquely defined by the scattered field as $\bar{\mathbf{a}}^{\mathrm{s}} = \sum_{j=1}^{L} \frac{\bar{u}_j^{*} \cdot \bar{E}^{\mathrm{sca}}}{\sigma_j} \bar{v}_j$, where the definition of the parameters are similar to Chapter 2. $\bar{\mathbf{a}}$ is decomposed as $\bar{\mathbf{a}} = \bar{\mathbf{a}}^{\mathrm{s}} + \bar{\mathbf{a}}^{\mathrm{n}} = \bar{\mathbf{a}}^{\mathrm{s}} + \bar{\bar{V}}^{\mathrm{n}} \cdot \bar{\alpha}^{\mathrm{n}}$, where $\bar{\bar{V}}^{\mathrm{n}}$ is composed of $(2M+1)N - L$ right singular vectors and $\bar{\alpha}^{\mathrm{n}}$ is a $(2M+1)N - L$ dimensional vector to be solved for by optimization.

Due to the truncation of the singular values, the residue in the field equation can be defined as,

$$\Delta^{\text{fie}} = \left\| \bar{\boldsymbol{\psi}}^{\text{t}} \cdot \bar{\mathbf{a}}^{\text{s}} + \bar{\boldsymbol{\psi}}^{\text{t}} \cdot \bar{\bar{V}}^{\text{n}} \cdot \bar{\alpha}^{\text{n}} - \bar{E}^{\text{sca}} \right\|^2, \tag{3.8}$$

Similarly, the residue in the state equation (3.6) is defined to be [17],

$$\Delta^{\text{sta}} = \left\| \bar{\bar{C}} \cdot \bar{\alpha}^{\text{n}} - \bar{D} \right\|^2, \tag{3.9}$$

where $\bar{\bar{C}} = \bar{\bar{V}}^{\text{n}} + \hat{O} \cdot \bar{\bar{A}} \cdot \bar{\bar{V}}^{\text{n}}$ and $\bar{D} = \hat{O}[\bar{\mathbf{e}} - \bar{\bar{A}} \cdot \bar{\mathbf{a}}^{\text{s}}] - \bar{\mathbf{a}}^{\text{s}}$. The total relative residue is defined to be

$$\Delta^{\text{tot}} = \Delta^{\text{fie}} / \left\| \bar{E}^{\text{sca}} \right\|^2 + \Delta^{\text{sta}} / \left\| \bar{\mathbf{a}}^{\text{s}} \right\|^2. \tag{3.10}$$

For each incidence $\bar{E}_p^{\text{inc}}$, the total relative residue can be calculated as Δ_p^{tot}, $p = 1, 2, \ldots, N_{\text{inc}}$. The $\hat{O}$ is the unknown parameter to be solved for in the first step of optimization process, which is a square matrix of dimension $N(2M+1) \times N(2M+1)$. The $\hat{O}$ matrix can be obtained by minimizing the following objective function

$$f(\hat{O}) = \frac{1}{2} \sum_{p=1}^{N_{\text{inc}}} \Delta_p^{\text{tot}}. \tag{3.11}$$

In solving the cost function, the alternative two-step CG optimization method [17] is adopted as the optimization scheme, i.e. alternatively updating $\bar{\alpha}^{\text{n}}$ and the $\hat{O}$ matrix. The steps of the algorithm are summarized as follows,

Step 1: Calculate $\bar{\boldsymbol{\psi}}^{\text{t}}$ and the SVD of it. Obtain $\bar{\mathbf{a}}_p^{\text{s}}$, $p = 1, 2, \ldots N_{\text{inc}}$.

Step 2: Initialization: $n = 0$, set $\hat{O}_0 = 0$, $\bar{\alpha}_{p,0}^{\text{n}} = 0$, and set the search direction $\bar{\rho}_{p,0} = 0$.

Step 3: $n = n + 1$.

Step 3.1: Update $\bar{\alpha}^{\mathrm{n}}_{p,n}$: Calculate gradient (Frechet derivative) $\bar{g}_{p,n} = \nabla_{\bar{\alpha}^{\mathrm{n}}_{p}} f$ evaluated at $\bar{\alpha}^{\mathrm{n}}_{p,n-1}$ and $\hat{O}_{n-1}$. Determine the search directions $\bar{\rho}_{p,n} = \bar{g}_{p,n} + \dfrac{\mathrm{Re}[(\bar{g}_{p,n} - \bar{g}_{p,n-1})^{*} \cdot \bar{g}_{p,n}]}{\left\|\bar{g}_{p,n-1}\right\|^{2}} \bar{\rho}_{p,n-1}$. Plug $\bar{\alpha}^{\mathrm{n}}_{p,n} = \bar{\alpha}^{\mathrm{n}}_{p,n-1} + d_{p,n}\bar{\rho}_{p,n}$ into the objective function, which is quadratic in terms of $d_{p,n}$, to get the solution of parameter $d_{p,n}$. Then update $\bar{\alpha}^{\mathrm{n}}_{p,n} = \bar{\alpha}^{\mathrm{n}}_{p,n-1} + d_{p,n}\bar{\rho}_{p,n}$.

Step 3.2: Update $\hat{O}_{n}$: for the ith element, $i = 1, 2, \ldots, N(2M+1)$, update the vector of amplitude of the induced multipole $(\bar{\mathbf{a}}_{p,n})_i = (\bar{\mathbf{a}}^{\mathrm{s}}_{p})_i + (\bar{\bar{V}}^{\mathrm{n}} \cdot \bar{\alpha}^{\mathrm{n}}_{p,n})_i$. Then update the coefficient for the total field $(\bar{\mathbf{e}}_p)_i - (\bar{\bar{A}} \cdot \bar{\mathbf{a}}_{p,n})_i$. The objective function has an analytical derivative with respect to $(\hat{O}_n)_i$ and the solution of $(\hat{O}_n)_i$ is given by

$$(\hat{O}_n)_i = \sum_{p=1}^{N_{\mathrm{inc}}} \frac{[(\bar{\mathbf{e}}_p)_i - (\bar{\bar{A}} \cdot \bar{\mathbf{a}}_{p,n})_i]^{*} \cdot (\bar{\mathbf{a}}_{p,n})_i}{\left\|\bar{\mathbf{a}}^{\mathrm{s}}_{p}\right\|^{2}} \Bigg/ \sum_{p=1}^{N_{\mathrm{inc}}} \frac{[(\bar{\mathbf{e}}_p)_i - (\bar{\bar{A}} \cdot \bar{\mathbf{a}}_{p,n})_i]^{*} \cdot [(\bar{\mathbf{e}}_p)_i - (\bar{\bar{A}} \cdot \bar{\mathbf{a}}_{p,n})_i]}{\left\|\bar{\mathbf{a}}^{\mathrm{s}}_{p}\right\|^{2}}, \tag{3.12}$$

where $i = 1, 2, 3, \ldots, (2M+1)N$.

Step 3.3: If termination condition is satisfied, stop iteration. Otherwise, go to Step 3.

B. Choice of multipole truncation number

For TM incidence, with the fine meshing assumption ($k_0 R << 1$), $M = 0$ is sufficient enough to represent the multipole scattering effects on either the dielectric or the PEC subunits. For dielectric subunit, the small term polynomial approximations (Appendix II) for elements in *T*-matrix are $[T]_0 = \dfrac{\pi (k_0 R)^2}{4\mathrm{i}} (1 - \varepsilon_r)$ and $[T]_1 = \dfrac{\pi \mathrm{i}}{32} (\varepsilon_r - 1)(k_0 R)^4$, respectively ($[T]_{-1} = [T]_1$). While for PEC subunit, the small

term polynomial approximations for elements in *T*-matrix are $[T]_0 = \frac{\pi \mathrm{i}}{2\ln(k_0 R)}$ and $[T]_1 = \frac{\pi}{4\mathrm{i}}(k_0 R)^2$, respectively. From the approximation polynomial, we see that the monopole element is leading in magnitude for both PEC and dielectric scatterers individually. However it is inaccurate to use only monopole element to model the scattering problem for a mixture of two kinds of scatterers. The dipole element in *T*-matrix for PEC is on the same order of $k_0 R$ as the monopole element of dielectric subunit. Therefore in the mixed boundary inverse problem, $M = 1$ should be chosen as the truncation number of multipoles, to accurately represent the multipole scattering effects on both the PEC and dielectric subunit.

To accelerate the optimization process, $M = 0$ is firstly chosen to get a rough initial guess of the leading monopole elements in *T*-matrixes. Then $M = 1$ is used to retrieve the whole matrix $\hat{O}$. It is worth mentioning that because of the symmetric property, the two dipole elements $[T]_1$ and $[T]_{-1}$ in the *T*-matrix equal to each other. Therefore in matrix $\hat{O}$ the $(2i-1)$th and $(2i+1)$th elements, $i = 1, 2, \ldots, N$, should equal to each other. Thus the unknowns are reduced by one third in optimization step 3.2.

C. The classification criterion

After $\hat{O}$ is retrieved by the first step of optimization process, the retrieved *T*-matrix for the ith cell can be expressed as $\overline{\overline{T_i}}$, $i = 1, 2, \ldots, N$, which includes the dipole elements $[T]_{\pm 1}$ and the monopole element $[T]_0$. We further study the elements in *T*-matrices for PEC and dielectric scatterers, to provide a criterion for differentiating the PEC and dielectric scatterers.

From Eq.(3.5), we know that the monopole element in the *T*-matrix for PEC is $[T]_0 = -\frac{J_0(k_0R)}{H_0^{(1)}(k_0R)}$, where $H_0^{(1)}(k_0R) = J_0(k_0R) + \mathrm{i}Y_0(k_0R)$. Under the small term assumption $k_0R << 1$, $J_0(k_0R)$ approaches to one, and $Y_0(k_0R)$ approaches to negative infinity [90]. Therefore, when $k_0R << 1$, the imaginary part of $[T]_0$ is a negative real number.

The elements of *T*-matrix for dielectric scatterer is nonlinear with respect to ε_{r}. Under the small term assumption $k_0R << 1$, the monopole element for dielectric can be approximated by the linear polynomial,

$$[T]_0 = \frac{\pi(k_0R)^2}{4\mathrm{i}}(1-\varepsilon_{\mathrm{r}}). \tag{3.13}$$

We consider only dielectric scatterers, the real part for relative permittivity of which is larger than one. Thus from Eq.(3.13), we see that the imaginary part of $[T]_0$ for a dielectric scatterer is larger than zero. When implementing the said classification criterion, special attention should also be paid to the case where the imaginary parts of the retrieved $[T]_0$ are of the value between $-\frac{\pi(k_0R)^2}{4}$ and 0, which indicates that the real part of the optimized relative permittivity is between zero and one. Considering that there are only dielectric scatterers with $\mathrm{real}(\varepsilon_{\mathrm{r}}) > 1$ and PEC scatterer with $|\varepsilon_{\mathrm{r}}| \to \infty$ inside the domain of interest and also due to the continuous property of the numerical optimization, these pixels should be classified as air.

To summarize the criterion of classifying the PEC from the dielectric scatterer, when determining the property of a subunit from the elements in $\overline{\overline{T}}_i$, $i = 1, 2, \ldots, N$, if the imaginary part of $[T]_0$ is a positive number, the subunit is determined to be dielectric scatterer. N_{die} is the number of dielectric subunits determined by $[T]_0$.

If the imaginary part of $[T]_0$ is between $-\frac{\pi(k_0R)^2}{4}$ and zero, the subunit is determined to be air. Otherwise, the subunit is determined to be PEC.

D. The univariate optimization

The second step of optimization process is a univariate optimization. We aim to retrieve the relative permittivity of each dielectric subunit from $\overline{\overline{T}}_i$, $i=1,2,\ldots,N_{\text{die}}$. A good initial guess for the second step of optimization process can be obtained from Eq.(3.13),

$$\varepsilon_{\text{r}} = 1 - \frac{4\text{i}[T]_0}{\pi(k_0R)^2}. \tag{3.14}$$

In this optimization, we reserve the nonlinearity between the *T*-matix and ε_{r}, getting a more accurate ε_{r} compared to [54], where the ε_{r} is solved directly from the polynomial approximation. The *T*-matrix for each subunit is independent of the others. For each subunit, the cost function is defined as

$$f_i(\varepsilon_{\text{r},i}) = \left|[T_i]_{0(\text{retrieved})} - [T_i]_0\right|^2 + \left|[T_i]_{1(\text{retrieved})} - [T_i]_1\right|^2, \quad i=1,2,\ldots,N_{\text{die}}, \tag{3.15}$$

where $[T_i]_0$ and $[T_i]_1$ are given by Eq.(3.4).

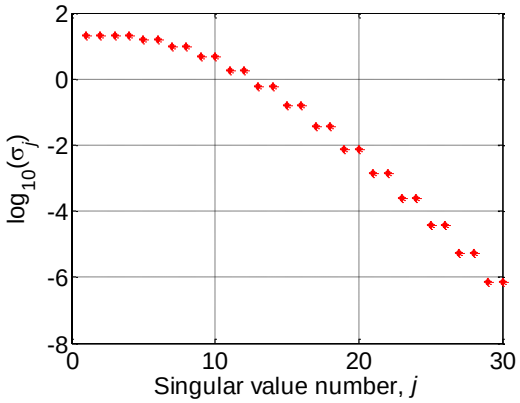

Fig.3-2. Singular values of the matrix $\bar{\Psi}^t$

Then the relative permittivity can be retrieved directly using Levenberg–Marquardt (LM) algorithm, with the initial guess given by Eq.(3.14).

3.3.2 Numerical Examples

The domains of interest for the first three numerical examples under investigation are squares of size $\lambda \times \lambda$, which are discretized into $N = 45 \times 45$ square subunits. The domain of interest for the last example is of size $\lambda \times 0.5\lambda$ and is discretized into $N = 60 \times 30$ square subunits. $N_{\text{inc}} = 10$ plane incident waves are evenly distributed on $[0, 2\pi)$. $N_{\text{r}} = 30$ receivers are symmetrically located on a circle of radius 5λ. To avoid the inverse crime, the multipole numbers used in getting the forward data is more than that used in the inverse part. The synthetic data is calculated by T-matrix method with $M = 2$.

In the inverse problem, $M = 1$ is the truncation number of the multipoles. $[T]_{\pm 1}$ do not numerically exist for $\varepsilon_{\text{r}} = 0$. Therefore in figures of numerical examples, we use $\varepsilon_{\text{r}} = 0$ to mark the PEC scatterers. Note that this practice only serves to visually distinguish PEC from dielectric scatterers in the relative permittivity

pattern. The singular value spectrum of the matrix $\bar{\psi}^t$ for $M=1$ is shown in Fig.3-2.

The numerical reconstruction does not yield a clear cut between PEC and air due to the feature of continuous parameter optimization. Instead, reconstructed image shows a gradual change from PEC into air. The imaginary parts of $[T]_0$ for the background pixels around PEC are also optimized to be negative. After applying the classification criterion as proposed in Section 3.3.1 to reconstruct the relative permittivity pattern, the size of the PEC scatterer should be enlarged a little bit, which can be accepted considering the optimization feature. Thus we also plot the patterns for the imaginary parts of $[T]_0$. To be specific, when estimating the reconstruction, we should refer to the pattern of imaginary parts of $[T]_0$ to get the information of PEC objects, while refer to the pattern for relative permittivity to get the information for dielectric scatterers.

In the first numerical example, we have two circles with radius 0.1λ placed inside the domain with centre distance 0.5λ, as shown in Fig. 3-3(a). The PEC circular scatterer is on the right side and is marked as $\varepsilon_r = 0$. The dielectric circular scatterer with $\varepsilon_r = 4$ is placed on the left side. Note that distance of the two scatterers is less than half wavelength. The synthetic data includes 10% white Gaussian noise to the exact scattered field. According to the criteria presented in Section 2.3.1, the number of leading singular values is chosen to be $L=8$. From the reconstructed pattern shown in Fig. 3-3 (b), the two objects are clearly identified with PEC on the right and dielectric on the left. To be specific, in Fig. 3-3 (c) we also draw

the imaginary part of $[T]_0$, from which we can clearly see the difference between the subunits of PEC and dielectric scatterers. The result coincides with our analysis in Section 3.3.1.

In the second example, two dielectric squares with relative permittivities $\varepsilon_r = 4$ and $\varepsilon_r = 2.5$ respectively are placed inside domain of interest as shown in Fig. 3-4(a). A PEC square is placed on left top of the domain. 10% white Gaussian noise is added to the exact scattered field and the number of truncated leading singular values is $L = 8$. From Fig. 3-4(b) we can clearly see two dielectric objects of different permittivities at around $\varepsilon_r = 4$ and $\varepsilon_r = 2.5$ respectively as well as a PEC object on top of the domain. Even though a little bit blurred, the approximate shape and the position of the PEC object are correctly reconstructed.

In the third example, a dielectric ring with $\varepsilon_r = 4$ is placed in the domain of interest as shown in Fig. 3-5(a). The outer radius is 0.25λ and inner radius is 0.15λ. A small square PEC object is placed on the upper right corner of the dielectric ring. 10% white Gaussian noise is added to the exact scattered field and $L = 8$. From Fig. 3-5(b) and Fig. 3-5(c), both the ring and PEC objects are correctly indentified and the hole of the ring is clearly seen.

In the last example, both PEC and dielectric lossy scatterer with $\varepsilon_r = 4 + 6\mathrm{i}$ coexist in the domain of interest. The shapes for both PEC and dielectric scatterers are circulars with radius 0.1λ. 10% white Gaussian noise is added to the exact scattered field and $L = 8$. From both the patterns for real parts and imaginary parts of the

relative permittivity as shown in Fig. 3-6, we can see the *T*-matrix SOM has successfully distinguished the PEC scatterer from a lossy dielectric scatterer.

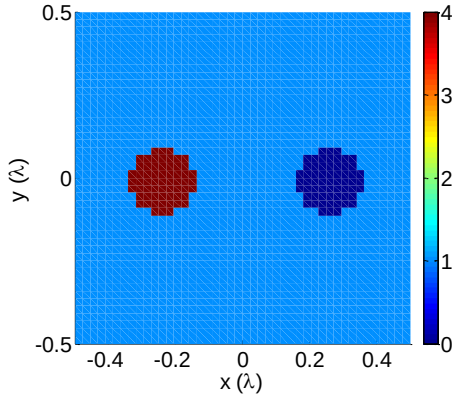

(a)

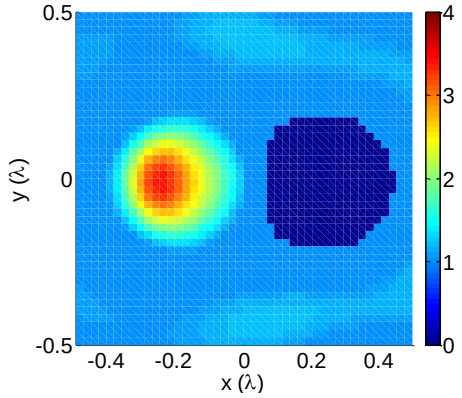

(b)

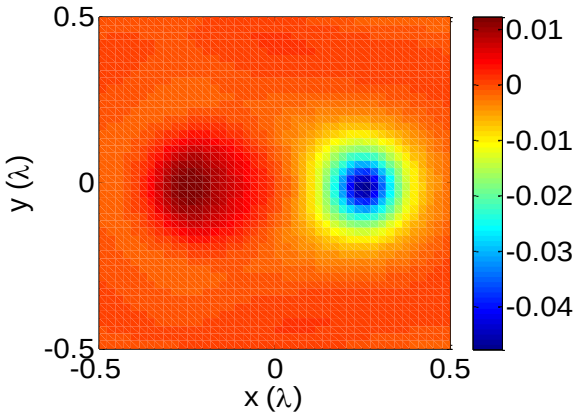

(c)

Fig. 3-3. Two circular objects: one PEC and one dielectric scatterer (a) original pattern. (b) reconstructed pattern. (c) the imaginary part of $[T]_{0.}$

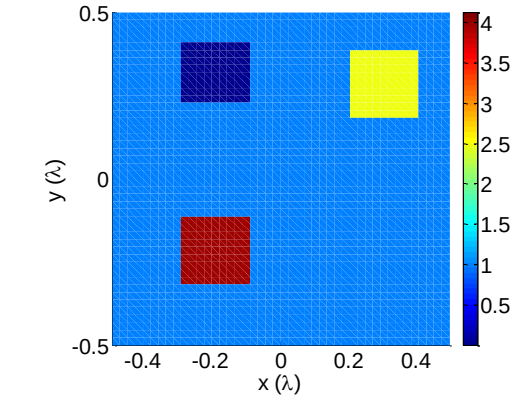

(a)

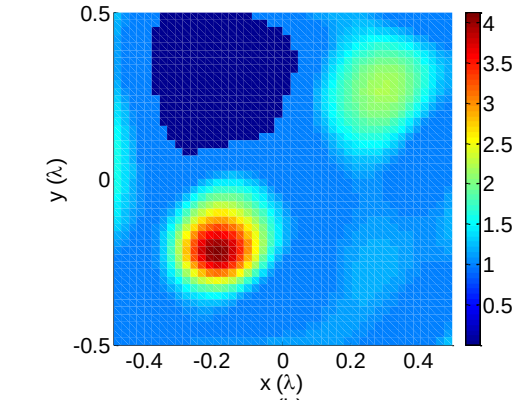

(b)

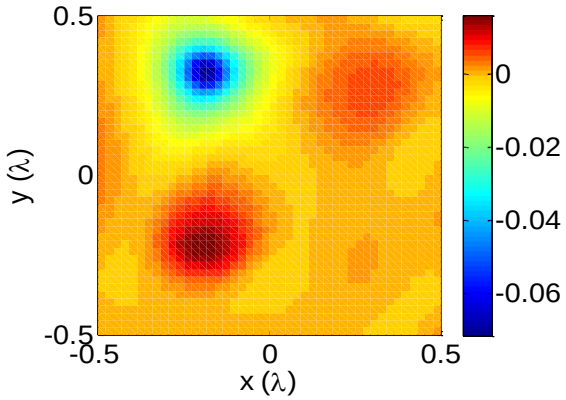

(c)

Fig. 3-4. Three square objects: one PEC and two dielectric scatterers with different permittivities (a) original pattern. (b) reconstructed pattern. (c) the imaginary part of $[T]_{0.}$

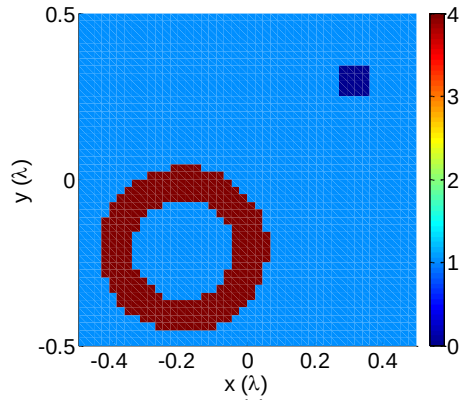

(a)

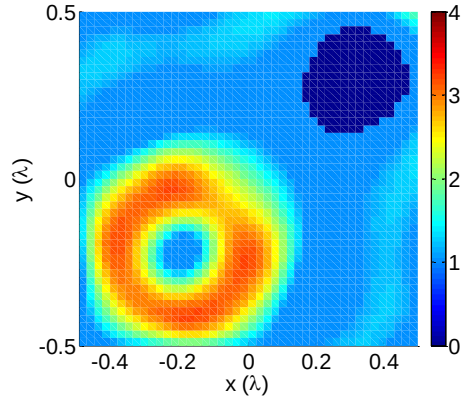

(b)

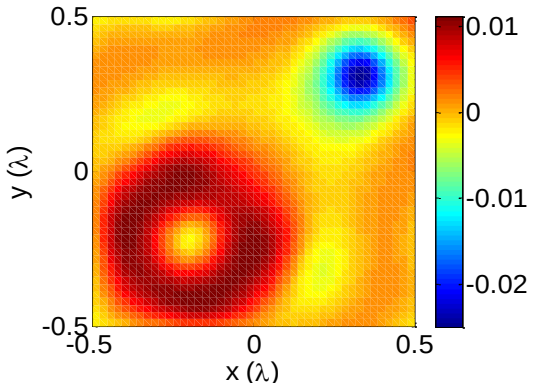

(c)

Fig. 3-5. A ring dielectric object and a PEC small square (a) original pattern. (b) reconstructed pattern. (c) the imaginary part of $[T]_0$.

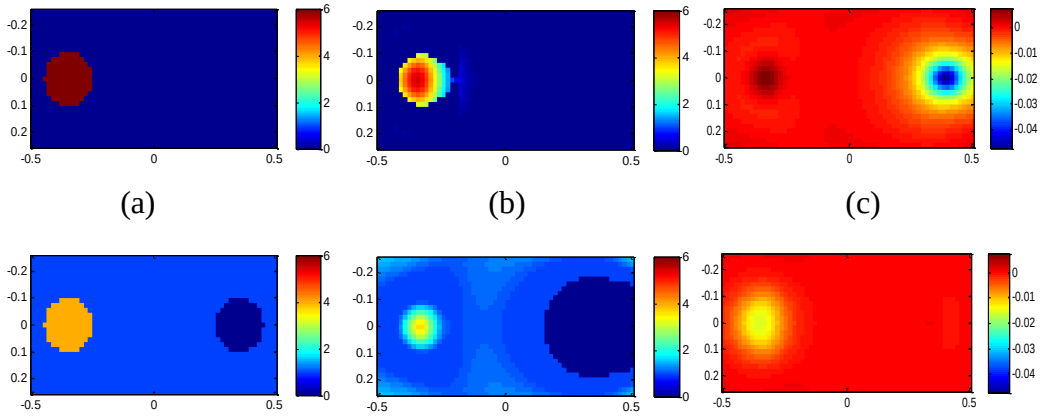

Fig. 3-6. A lossy dielectric scatterer and a PEC scatterer (a) original pattern for imaginary part of relative permittivity (b) reconstructed pattern for imaginary part of relative permittivity (c) the imaginary part of $[T]_0$ (d) original pattern for real part of relative permittivity (e) reconstructed pattern for real part of relative permittivity (f) the real part of $[T]_0$.

3.4 Summary

In this chapter we proposed an approach of using SOM to reconstruct the mixed boundary problem in two dimensional setting. The proposed algorithm is an extension of SOM to a new modeling scheme—*T*-matrix method. Numerical results show that the proposed method works well for the mixed boundary problem in sub-wavelength setting and inherits the merits of the original SOM, i.e., fast convergence, robust against noise, and high-resolution imaging ability.

4 SEPARABLE OBSTACLE PROBLEM

In this Chapter, the separable obstacle problem (SOP) which is encountered often in practice is solved by reformulating the SOM. By treating the inhomogeneous background as a known scatterer that is hosted in a homogeneous background, the computationally intensive calculation of the inhomogeneous background Green's function is avoided. Therefore we call the newly developed method the SOP-homo. Firstly, the SOP-homo is derived and formulated in the dielectric scatterer case based on the EFIE model. Secondly, SOP-homo is further extended to the *T*-matrix model, to solve the mixed boundary SOP where both the obstacle and the unknown scatterers are consisted as a mixture of PEC and dielectrics. Numerical examples indicate that the proposed method works well for SOP and is less computational intensive than the contemporary inhomogeneous model.

4.1 SOP for dielectric scatterer

Inverse scattering problems are of great interest to scientists nowadays [21, 49, 81, 91-96]. They have a wide application in the fields of optical diffraction tomography [95], bio-imaging [92], and non-destructive evaluation [93]. One specific case of inverse scattering problem is described as follows: 1) the problem involves imaging unknown scatterers surrounded by known obstacles. 2) There is no overlap between the scatterers and obstacles. Under these conditions, the obstacles are

separable from the unknown scatterers and we refer to such kind of problem as separable obstacle problem (SOP).

The quality evaluation of the cores in optical fiber cable is a typical SOP. Another example is the non-destructive evaluation of the dielectric slab waveguide, where the middle layer can be seen as the unknown scatterer to be reconstructed and the outer layers are the known obstacles. Some general through wall imaging problems [86, 97] can also be classified as SOP. Thus, the study on SOP is of practical importance.

Traditionally, the SOP is classified as an inhomogeneous background inverse problem [98], because the obstacle is generally regarded as part of the background medium. Thus, the Green's functions used for inhomogeneous background have complex forms [99]. Most of the published works consider only the cases where the (semi-) closed-form expressions of the corresponding Green's functions are available, such as half-space background medium [100, 101] or infinite length layered medium [86, 95]. However, when the obstacle is of arbitrary shape, numerical calculation of the Green's function is needed. In [49], the finite element method (FEM) is adopted as the numerical method, while in [96] the finite difference (FD) approach is involved to calculate the numerical Green's functions. However, the numerical approximations to Green's functions introduce numerical errors into the discrete model and are quite computationally intensive.

In this chapter, we aim to solve the SOP without resourcing to the numerical calculation of Green's functions while still providing good reconstruction results. The

main idea of the proposed approach is that the known obstacle can be treated as ‘known scatterer’ rather than part of the background. Therefore, the background is simply homogeneous and the elements corresponding to the obstacle can be excluded from the retrieving process of the unknowns by applying a mathematical reformulation of the cost function. The Green’s function used has just the analytical form for the homogeneous background. For this reason, we refer to our scheme as SOP-homo. It’s highlighted that the prior information of no overlap between the unknown scatterers and the known obstacles is essential for our method. Such specific condition is fulfilled very often in practice, like the examples presented before. For comparison, we refer to the methods that require numerical calculation of Green’s function (such as FEM/FD related approaches) as the Obstacle Problem-inhomo (OP-inhomo), which is applicable to both separable and non-separable obstacles. Furthermore, if the *a priori* information of separable obstacle is also used in OP-inhomo, we call it Separable Obstacle Problem-inhomo (SOP-inhomo).

We analyze various factors that influence the imaging quality of SOP, and finally give the strategy of choosing proper method for such problem. Various numerical results are given to validate SOP-homo and comparisons are also made with the other two methods mentioned above. Many numerical examples presented in this chapter are much more complex and difficult than existing reported results so far. The numerical results indicate that the SOP-homo works well for SOP and has a

better performance especially in the case of unknown scatterer adjacent to the obstacles.

4.1.1 Forward problem

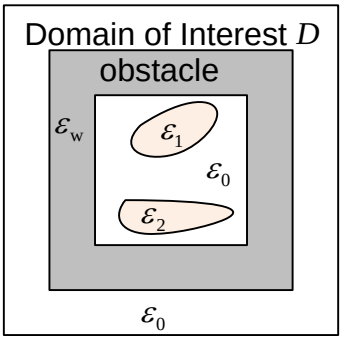

Fig. 4-1. A general scenario for SOP.

The forward problem consists of determining the scattered field on receivers given the information of the scatterers and the incident field. In this section, we present the forward model for dielectric case, which is the foundation of the inverse problem. We consider a two-dimensional problem under TM wave illumination. The setup of the problem is depicted in Fig. 4-1. Inside the domain of interest D, the obstacle of relative permittivity ε_{w} surrounds the unknown scatterers. The wave number in obstacle is denoted as k_{w}. The physical properties of the obstacle are known *a priori*. N_{inc} cylindrical waves symmetrically illuminate the domain of interest. Then the scattered field is received by N_{r} antennas evenly distributed on a circle outside the domain of interest D, the positions of which are $\mathbf{r}_q$, $q = 1, 2, \ldots, N_{\mathrm{r}}$. Thus, there are totally $N_{\mathrm{r}} \times N_{\mathrm{inc}}$ data points of measurements recorded in the scattered field matrix. We discretize the domain of interest into N square-shaped subunits, and the centers of subunits are located at $\mathbf{r}_1, \mathbf{r}_2, \ldots, \mathbf{r}_N$. Out of these N subunits, the number of subunits that belong to the known obstacle is N_{w}.

The scattered field and the incident field at $\mathbf{r}$ satisfy the following Helmholtz equations [102],

$$\left[\nabla^2 + k_b^2(\mathbf{r})\right] E_z^{\text{sca}}(\mathbf{r}) = -[k^2(\mathbf{r}) - k_b^2(\mathbf{r})] E_z^{\text{tot}}(\mathbf{r}), \tag{4.1}$$

$$\left[\nabla^2 + k_b^2(\mathbf{r})\right] E_z^{\text{inc}}(\mathbf{r}) = -S(\mathbf{r}), \tag{4.2}$$

where $k_b(\mathbf{r})$ denotes the background wave number and $k(\mathbf{r})$ is the wave number at point $\mathbf{r}$, $E_z^{\text{tot}} = E_z^{\text{sca}} + E_z^{\text{inc}}$ indicates the total electric field. The primary source is given by $S(\mathbf{r})$.

The integral solutions of Eq. (4.1) and Eq.(4.2) are

$$E_z^{\text{sca}}(\mathbf{r}) = \int_D g(k_b; \mathbf{r}, \mathbf{r}') \left[k^2(\mathbf{r}') - k_b^2(\mathbf{r}')\right] E_z^{\text{tot}}(\mathbf{r}') d\mathbf{r}', \tag{4.3}$$

$$E_z^{\text{inc}}(\mathbf{r}) = \int_D g(k_b; \mathbf{r}, \mathbf{r}') S(\mathbf{r}') d\mathbf{r}'. \tag{4.4}$$

Eq. (4.3) can be rewritten into discrete form, and the total electric field on the mth subunit satisfies the self-consistent equation,

$$E_z^{\text{tot}}(\mathbf{r}_m) = E_z^{\text{inc}}(\mathbf{r}_m) + \sum_{i \neq m} \text{i} k_b \eta_b g(k_b; \mathbf{r}_m, \mathbf{r}_i) \xi_i E_z^{\text{tot}}(\mathbf{r}_m), \quad m = 1, 2, \ldots, N. \tag{4.5}$$

The scattering strength is given by $\xi_i = -\text{i}(k_b / \eta_b) A_i \left[\varepsilon_r(\mathbf{r}_i) - 1\right]$. $\varepsilon_r(\mathbf{r}_i)$ and A_i denote the relative permittivity with respect to the background medium and the area of the ith subunit, respectively, and $\eta_b = \sqrt{\mu_0 / \varepsilon_b}$ is the impedance of the background medium, where μ_0 is the permeability of free space, and ε_b is the permittivity of the background medium.

Then we can write the scattered field on the receivers in a matrix form, which we call the field equation,

$$\bar{E}^{\text{sca}} = \bar{\bar{G}}_{\text{s}} \cdot \bar{I}^{\text{d}}. \tag{4.6}$$

Here $\bar{\bar{G}}_{\mathrm{s}}(q,m) = \mathrm{i}k_b\eta_b g(k_b;\mathbf{r}_q,\mathbf{r}_m)$ for $m = 1,2,\ldots,N$ and $q = 1,2,\ldots,N_{\mathrm{r}}$. Further, $\bar{I}^{\mathrm{d}} = [I_z^{\mathrm{d}}(\mathbf{r}_1), I_z^{\mathrm{d}}(\mathbf{r}_2),\ldots, I_z^{\mathrm{d}}(\mathbf{r}_N)]^{\mathrm{T}}$, $\bar{E}^{\mathrm{sca}} = [E_z^{\mathrm{sca}}(\mathbf{r}_1), E_z^{\mathrm{sca}}(\mathbf{r}_2),\ldots, E_z^{\mathrm{sca}}(\mathbf{r}_{N_{\mathrm{r}}})]^{\mathrm{T}}$. The scattering strength ξ_i relates the total electric field to the induced current/contrast source by $I_z^{\mathrm{d}}(\mathbf{r}_i) = \xi_i E_z^{\mathrm{tot}}(\mathbf{r}_i)$. We get the state equation in a compact form,

$$\bar{I}^{\mathrm{d}} = \bar{\bar{\xi}}(\bar{E}^{\mathrm{inc}} + \bar{\bar{G}}_{\mathrm{D}} \cdot \bar{I}^{\mathrm{d}}) \tag{4.7}$$

where $\bar{\bar{G}}_{\mathrm{D}}(m,i) = (\mathrm{i}k_b\eta_b)g(k_b;\mathbf{r}_m,\mathbf{r}_i)$ and $\bar{E}^{\mathrm{inc}} = [E_z^{\mathrm{inc}}(\mathbf{r}_1), E_z^{\mathrm{inc}}(\mathbf{r}_2),\ldots, E_z^{\mathrm{inc}}(\mathbf{r}_N)]^{\mathrm{T}}$. $\bar{\bar{\xi}}$ is a diagonal matrix composed by ξ_i, $i = 1,2,\ldots,N$.

$\bar{\bar{G}}_{\mathrm{s}}$ and $\bar{\bar{G}}_{\mathrm{D}}$ in the field equation Eq.(4.6) and state equation Eq.(4.7) are matrices of Green's functions, which map the induced current to the scattered field at the points outside and inside the investigation domain, respectively. According to the different definitions of the background medium, two kinds of forward models can be extracted from Eq. (4.1) to (4.7):

Model I: If the obstacle is regarded as part of the background, the background medium is inhomogeneous. The Green's function needs to be calculated by numerical methods such as FEM/FD etc.

Model II: If the obstacle is regarded as the known scatterer rather than the background, the background medium is homogeneous and is simply the free space. The Green's function exists analytically [103].

Table 4-1: Comparison of the Model I and Model II

	k_b	$\bar{\bar{G}}_{\mathrm{D}}$ & $\bar{\bar{G}}_{\mathrm{s}}$	$\bar{E}^{\mathrm{inc}}$	$\bar{E}^{\mathrm{sca}}$
Model I	$k_b(\mathbf{r}) = \begin{cases} k_{\mathrm{w}}, \ \mathbf{r} \in \text{obstacle} \\ k_0, \ \mathbf{r} \in \text{air} \end{cases}$	Numerical–inexact and computationally intensive	Numerical –numerical noise contained	Numerical –numerical noise contained
Model II	k_0	Analytical – exact and easy to compute	Analytical – no numerical noise	Analytical – no numerical noise

According to Eqs.(4.3) and (4.4), the calculated $\bar{E}^{\mathrm{inc}}$ and $\bar{E}^{\mathrm{sca}}$ are totally different in these two models. Comparisons between the two models are made as shown in Table 4-1.

In summary, by avoiding the numerical calculation of the Green's function, the advantages of model II over model I are:

i. The computation complexity is reduced,

ii. The computing time is reduced,

iii. The numerical noise to the inverse model is avoided.

The OP/SOP-inhomo employs the model I while the SOP-homo uses model II.

4.1.2 Inverse problem

The inverse scattering problem is to retrieve the relative permittivity matrix $\bar{\bar{\xi}}$ from the measured scattered field. We use the SOM as a demonstration reconstruction method to show the detail of solving the SOP. Namely, we will do the reformulation on SOM (so as to get the so-called SOP-homo) in order to utilize the prior information of SOP.

A. Outline of standard SOM

The main idea of SOM is to firstly obtain the deterministic part of the induced current $\bar{I}^{\mathrm{s}}$ by using Equ. (2.4) in Section 2.3.1. Then the remaining part of the induced current $\bar{I}^{\mathrm{n}} = \bar{I}^{\mathrm{d}} - \bar{I}^{\mathrm{s}}$ is obtained through optimization. The two terms $\bar{\bar{\xi}}$ and $\bar{I}^{\mathrm{n}}$ are alternatively updated using the CG method. The action of fixing one portion of the induced current first can greatly speed up the optimization process.

The cost function is the sum of residues from both field and state equations,

$$f(\bar{\bar{\xi}}) = \sum_{p=1}^{N_{\mathrm{inc}}} \left(\Delta_p^{\mathrm{fie}} \Big/ \left\| \bar{E}_p^{\mathrm{sca}} \right\|^2 + \Delta_p^{\mathrm{sta}} \Big/ \left\| \bar{I}_p^{\mathrm{s}} \right\|^2 \right), \tag{4.8}$$

The Δ^{fie} denotes the residue in the field equation and is given by

$$\Delta^{\mathrm{fie}} = \left\| \bar{E}^{\mathrm{sca}} - \bar{\bar{G}}_{\mathrm{s}} \cdot \bar{I}^{\mathrm{d}} \right\|^2 . \tag{4.9}$$

The residue in the state equation is defined to be,

$$\Delta^{\mathrm{sta}} = \left\| \bar{I}^{\mathrm{d}} - \bar{\bar{\xi}} (\bar{E}^{\mathrm{inc}} + \bar{\bar{G}}_D \cdot \bar{I}^{\mathrm{d}}) \right\|^2 . \tag{4.10}$$

The algorithm is briefly presented below and we refer the readers to the previous chapters for the details. Here $\bar{I}_{p,n}^{\mathrm{n}}$, $p = 1, 2, \ldots, N_{\mathrm{inc}}$ denotes the remaining part of induced current in the nth step of iteration. And $\bar{\bar{\xi}}_n$ denotes the matrix of scattering strength in the nth step of iteration.

Step 1: Data preparation

Step 2: Initialization: $n = 0$.

Step 3: Iteration: $n = n + 1$.

Step 3.1: Update $\bar{I}_{p,n}^{\mathrm{n}}$, while regarding $\bar{\bar{\xi}}_n$ as a known parameter.

Step 3.2: Update $\bar{\bar{\xi}}_n$, while regarding $\bar{I}_{p,n}^{\mathrm{n}}$ as a known parameter.

Step 4: If termination condition is satisfied, stop iteration. Otherwise, go to Step 3.

B. Reformulation of SOM for SOP:

In this section we introduce how to reformulate the SOM so as to utilize the prior information of SOP. Since no scatterers overlap with the obstacles, the subunits belonging to the obstacles can be fixed throughout the whole updating process. Therefore the number of unknowns in matrix $\bar{\bar{\xi}}$ is actually $N - N_{\mathrm{w}}$ which is the number of non-obstacle elements. Thus in step 1 and 2 of the updating algorithm, the initial guess of $\bar{\bar{\xi}}$ is modified according to the prior information of the obstacle.

In step 3.2, since $\bar{I}^{\mathrm{n}}_{p,n}$ is regarded as a known parameter, the field residue (4.9) is fixed and only state residue changes as a consequence of updating $\bar{\bar{\xi}}_n$. In (4.8), the cost function can be written as summation of each individual element as,

$$f\left(\bar{\bar{\xi}}\right)=\sum_{p=1}^{N_{\mathrm{inc}}}\left(\frac{\Delta_p^{\mathrm{fie}}}{\left\|\bar{E}_p^{\mathrm{sca}}\right\|^2}+\frac{\sum_{i=1}^{N}\left(\Delta_p^{\mathrm{sta}}\right)_i}{\left\|\bar{I}_p^{\mathrm{s}}\right\|^2}\right) \tag{4.11}$$

Thus, we can split the objective function into three parts: the field residue $\left(\Delta_{p,n}^{\mathrm{fie}}\right)$, the state residue corresponding to the obstacle subunits $\left(\Delta_{p,n}^{\mathrm{sta}}\right)^{\mathrm{obs}}$ and the state residue corresponding to the non- obstacle subunits $\left(\Delta_{p,n}^{\mathrm{sta}}\right)^{\text{non-obs}}$, i.e.,

$$f\left[\left(\bar{\bar{\xi}}_n\right)_i\right]=\frac{1}{2}\sum_{p=1}^{N_{\mathrm{inc}}}\left(\frac{\Delta_{p,n}^{\mathrm{fie}}}{\left\|\bar{E}_p^{\mathrm{sca}}\right\|^2}+\sum_{i=1}^{N_{\mathrm{w}}}\frac{\left(\Delta_{p,n}^{\mathrm{sta}}\right)_i^{\mathrm{obs}}}{\left\|\bar{I}_p^{\mathrm{s}}\right\|^2}+\sum_{i=1}^{N-N_{\mathrm{w}}}\frac{\left(\Delta_{p,n}^{\mathrm{sta}}\right)_i^{\text{non-obs}}}{\left\|\bar{I}_p^{\mathrm{s}}\right\|^2}\right). \tag{4.12}$$

On the right hand side of Eq.(4.12), the first two terms are constant with respect to the unknowns (the $(\bar{\bar{\xi}}_n)_i$ on non-obstacle subunits). Thus, only the last term in Eq. (4.12) contributes in the CG update with respect to the unknowns

$(\overline{\overline{\xi}}_n)_i, i=1,2,\ldots,N-N_{\mathrm{w}}$. The details of updating $\overline{\overline{\xi}}_n$ are similar to [49] but with a less number of unknowns.

C. Discussion

Besides the model advantages indicated in section II, the above optimization scheme has another advantage that the number of unknowns is significantly reduced compared to the general SOM model, which results in a faster convergence speed.

Although there are various advantages for the SOP-homo scheme, it is important to note that a trade-off is also involved. Even though we have excluded the obstacle from the updating process of $\overline{\overline{\xi}}$, the currents in the known obstacle and the unknown scatterers, coexist in our scheme. On the other hand, in OP/SOP-inhomo, the obstacle is totally regarded as background and the induced current corresponds to only the unknown scatterer. This is because the multiple scattering effects between the scatterers and obstacles have already been involved in the inhomogeneous background Green's function. As a consequence, the SOP-homo has a higher nonlinearity compared to OP/SOP-inhomo, which may reduce the quality of reconstruction, for example in some cases where the known obstacle has a higher permittivity than the unknown scatterer. However, in the application of optical fiber or waveguide evaluation, the unknown scatterers (core) usually have a higher permittivity than the obstacle (cladding), which indicates that SOP-homo still serves as a good choice for such kind of problem.

In summary, there are two factors that influence the quality of reconstruction in SOP. The first factor is the Green's functions and related numerical inaccuracies.

The second factor is the nonlinearity of the model used for the problem. SOP-homo performs better in the first factor while OP/SOP-inhomo performs better in the second factor.

4.1.3 Numerical examples

We present five numerical examples to validate our method as well as the influencing factors on imaging quality. Since SOM is used in SOP-homo as the optimization scheme, the FEM-SOM in [49] is taken as a comparison method. Depending on whether or not the *separable* obstacle information is applied, we denote the two editions of FEM-SOM as the OP-inhomo and SOP-inhomo, respectively.

The domain of interest for all five numerical examples is square of size $2\lambda \times 2\lambda$ and is discretized into $N = 45 \times 45$ square subunits. $N_{\text{inc}} = 10$ cylindrical waves are used as incident sources. The scattered field is measured by $N_{\text{r}} = 30$ receivers evenly distributed around a circle of radius 5λ. In all the examples, the measurement data are got by MoM and are contaminated by 10% white Gaussian noise. The singular value spectrum for the SOP-homo is drawn in Fig.4-2, and the singular value spectrum for the OP/SOP-inhomo is drawn in Fig. 4-3. For all the three methods (SOP-homo, SOP/OP-inhomo), the truncation number of leading singular values is chosen to be 10 and the optimization stops after 50 iterations. For quantitative comparison, we define the average relative error

$$e = \frac{\sum_{i=1}^{N} \left| \varepsilon_{\text{r\_true},i} - \varepsilon_{\text{r\_rec},i} \right| / \varepsilon_{\text{r\_true},i}}{N}, \tag{4.13}$$

where ε_{r_true} represents the true value of relative permittivity and ε_{r_rec} stands for the reconstructed value. For all the examples, the values of e are listed in Table 2. The units for the label of coordinates in reconstruction figures are λ.

A. Example 1

In this example, we aim to image one concave scatterer as well as one square scatter inside an annulus obstacle.

The outer radii and inner radii of the obstacle are 0.9λ and 0.7λ respectively. The relative permittivity of the obstacle is 1.5. There are two scatterers in the interior area of the obstacle. The first scatterer is an 'n' shaped scatterer with $\varepsilon_r = 2$ and the second scatterer is a square scatterer with $\varepsilon_r = 3$. The shapes and positions of these scatterers are shown in Fig. 4-4(a). Fig. 4-4(b) ~ (d) are the reconstruction results for SOP-homo, OP-inhomo and SOP-inhomo respectively. The reconstructed profiles in Fig. 4-4(b) ~ (d) show that all methods clearly retrieve the positions and permittivities of the scatterers, including the concave area of the "n" shaped scatterer. The reconstruction errors presented in Table 4-2 show SOP-homo performs better than OP/SOP-inhomo. The reason of worse performance of SOP-inhomo than SOP-homo is because of its lower accuracy of Green's function.

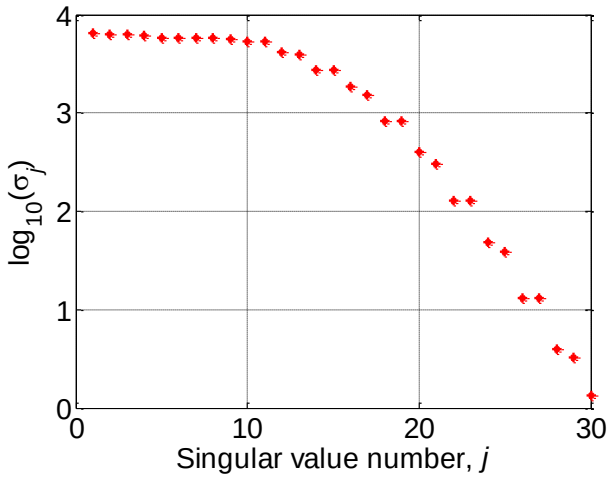

Fig.4-2 Singular values of the matrix $\overline{\overline{G}}_S$ for SOP-homo

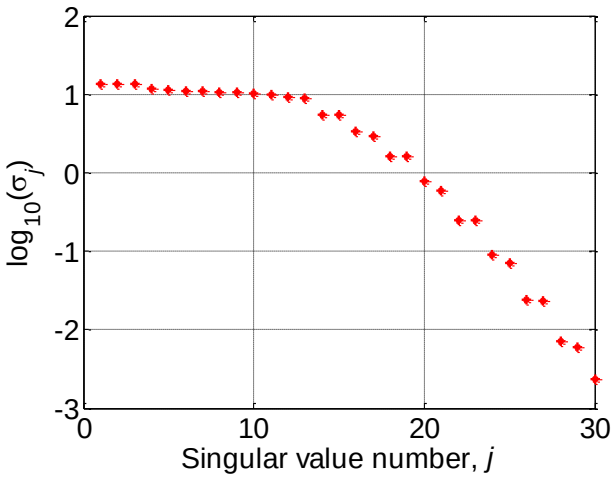

Fig. 4-3 Singular values of the matrix $\overline{\overline{G}}_S$ for OP/SOP-inhomo

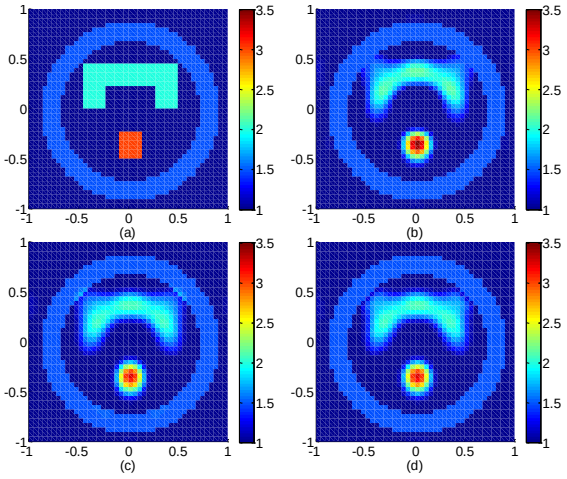

Fig. 4-4. The configuration of scatterer in the first numerical example. The scattering data are contaminated with 10% white Gaussian noise. (a) Exact profile. (b) Reconstructed profile by SOP-homo. (c)Reconstructed profile by OP-inhomo. (d) Reconstructed profile by SOP-inhomo.

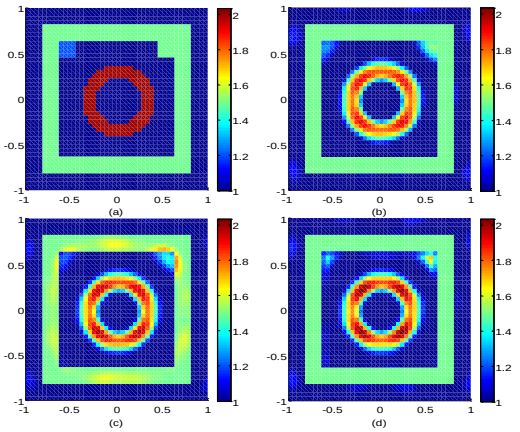

Fig.4-5. The configuration of scatterer in the second numerical example. The scattering data are contaminated with 10% white Gaussian noise. (a) Exact profile. (b) Reconstructed profile by SOP-homo. (c)Reconstructed profile by OP-inhomo. (d) Reconstructed profile by SOP-inhomo.

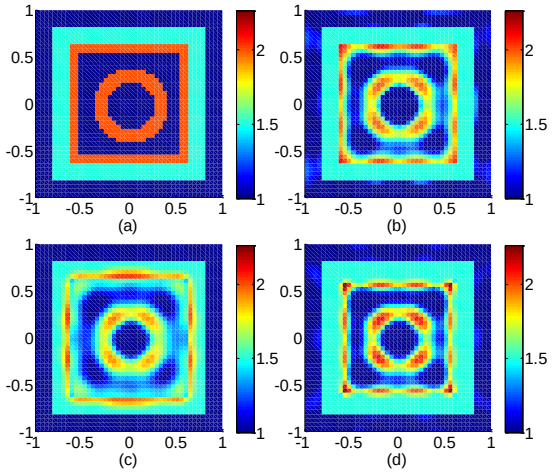

Fig. 4-6. The configuration of scatterer in the third numerical example. The scattering data are contaminated with 10% white Gaussian noise. (a) Exact profile. (b) Reconstructed profile by SOP-homo. (c)Reconstructed profile by OP-inhomo. (d) Reconstructed profile by SOP-inhomo.

B. Example 2

In the second example, we consider scatterers adjacent to the known obstacle. Such scatterers are difficult to reconstruct due to the proximity to the obstacle.

As shown in Fig.4-5(a), the known obstacle is square shaped, with the outer side length 1.63λ and the inner side length 1.26λ, and its relative permittivity is 1.5. There is an annular scatterer in the interior region of the obstacle, with inner and outer radii 0.25λ and 0.4λ, respectively, and its relative permittivity is 2. The centers of both the known square obstacle and the annular scatterer are at the origin.

There are two small scatterers (similar to the presence of unanticipated clutters) adjacent to the known obstacle and in the corner, with the relative permittivities of 1.4 and 1.5 respectively.

Fig.4-5(b)~(d) are the reconstruction results for SOP-homo, OP-inhomo and SOP-inhomo respectively. We see that the position, the shape, as well as the relative permittivity of the annulus inside the obstacle are well reconstructed. Besides, the two objects adjacent to the obstacle are also seen clearly in Fig.4-5(b) and Fig.4-5(d), while the square obstacle appears blurred by the adjacent objects in Fig.4-5(c). This is mainly because in OP-inhomo, the obstacle is regarded as background and the optimization updates the permittivity in the region of the obstacle as well. While in SOP-homo/SOP-inhomo the obstacle is regarded as known scatterer and its permittivity is not allowed to change during the iteration. From Table 4-2 we see that the relative error of SOP-homo is smaller than those of the other two.

C. Example 3

The third example is more challenging. In this example the inner surface of the obstacle is coated with a thin layer of a material with relative permittivity 2. The physical properties of the annular object as well as the obstacle remain the same as in the second example and the thickness of inner layer is 0.07λ, see Fig. 4-6(a).

From the reconstructed pattern in Fig. 4-6(c) which is the obtained by OP-inhomo, we see that the both the obstacle and its inner layer appear blurred. Fig. 4-6(b) and Fig. 4-6(d) for SOP-homo and SOP-inhomo are much better, which prove

again that the usage of the prior information of separable obstacle demonstrates better results in the cases where the object is placed near the obstacle.

D. Example 4

Table 4-2: The relative errors in the reconstructions of examples 1-5.

	SOP-homo	OP-inhomo	SOP-inhomo
1st	0.0364	0.0432	0.0431
2nd	0.0337	0.0368	0.0355
3rd	0.0724	0.1125	0.0769
4th	0.0500	0.0698	0.0477
5th	0.0553	0.0423	0.0420

In the fourth example, the setup is the same as the third example except that the inner layer has a relative permittivity of 1.4, which is lower than the obstacle, as seen in Fig.4-8(a).

From Fig.4-8(b) ~ (d) and Table 4-2, it is clearly seen that SOP-homo and SOP-inhomo reconstruct the inner layer of the obstacle as well as the annulus better than the OP-inhomo.

E. Example 5

As indicated previously, the SOP-homo compromises in nonlinearity to avoid the computationally intensive Green's function calculation. This example highlights the aspect of nonlinearity. In this example the shape of the obstacle and the annulus object remain the same as the previous examples. The only difference is the relative permittivity of the obstacle is 2.5, higher than the unknown scatterer as seen in Fig. 4-7(a).

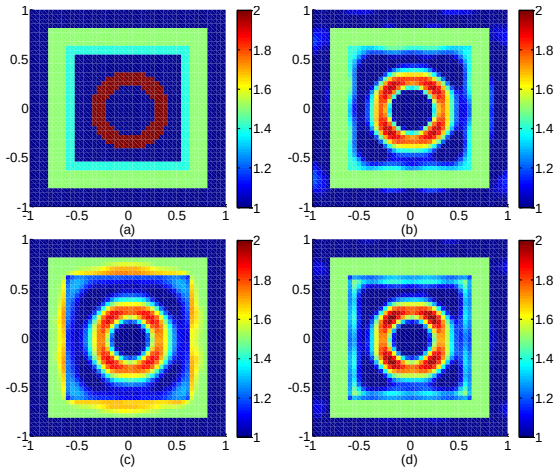

Fig.4-8. The configuration of scatterer in the fourth numerical example. The scattering data are contaminated with 10% white Gaussian noise. (a) Exact profile. (b) Reconstructed profile by SOP-homo. (c)Reconstructed profile by OP-inhomo. (d) Reconstructed profile by SOP-inhomo.

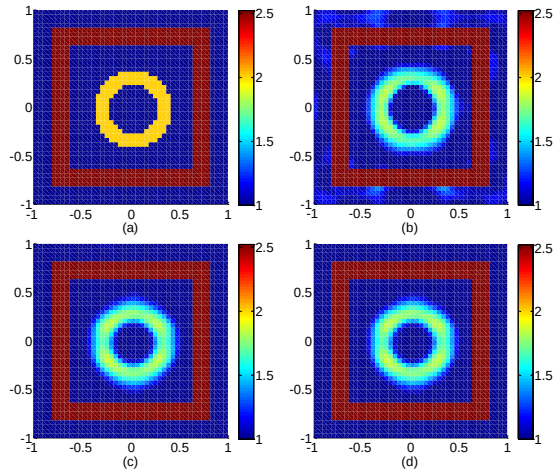

Fig. 4-7. The configuration of scatterer in the fifth numerical example. The scattering data are contaminated with 10% white Gaussian noise. (a) Exact profile. (b) Reconstructed profile by SOP-homo. (c) Reconstructed profile by OP-inhomo. (d) Reconstructed profile by SOP-inhomo.

Comparing the results in Fig. 4-7(b) ~ (d) and also from the errors in Table 4-2, we can see that SOP-homo gives a worse result than OP/SOP-inhomo in this example. This is mainly because the obstacle has a higher relative permittivity than the unknown scatterer, thus the induced current on the obstacle is stronger than that on the scatterer, which results in higher nonlinearity in SOP-homo compared to

OP/SOP-inhomo (where the obstacle is treated as the background and no induced current appears on the obstacle).

F. Further discussion about the results

Table 4-3 : The degrees of nonlinearity for examples 1-5.

	SOP-homo	SOP/OP-inhomo
1st	3.9531	3.9008
2nd	2.5529	2.4385
3rd	2.8552	2.5665
4th	2.5769	2.4538
5th	4.0690	2.6670

In order to verify our analysis about the nonlinearity for the SOP-homo and OP/SOP-inhomo, and also to quantitatively evaluate the nonlinearity for all the numerical examples, degree of nonlinearity [104], which is defined by $\left\| \overline{\overline{\xi}} \cdot \overline{\overline{G}}_{\mathrm{D}} \right\|_2$ in source type model, is calculated in our numerical simulations. Here matrix $\overline{\overline{\xi}}$ is the scattering strength, from which we can see the scattering strengths on the obstacle for OP/SOP-inhomo are zero values, while the scattering strengths on the obstacle in SOP-homo are non-zero values. Thus the degrees of nonlinearity for OP/SOP-inhomo are smaller than those in SOP-homo. In Table 4-3, we list the degrees of nonlinearity. We see the SOP-homo has a larger degree of nonlinearity than the other two methods in all five examples, and the degree contrast is especially sharp in the last example, which coincides with the previous discussion.

Obviously, SOP-inhomo performs better than OP-inhomo in all these examples because it takes use of the separable obstacle information and thus has fewer unknowns compared to the latter one. It is shown that the imaging resolution of

SOP is improved greatly after the use of the prior separable information. In summary, these numerical results verify the theoretical analysis in section 4.1.2. C.

4.1.4 Summary

We provide a comprehensive discussion on the imaging of SOP. We have introduced a new method called SOP-homo which properly utilizes the prior information of separable obstacle. The imaging performance of SOP is influenced by both the accuracy of the Green's function in forward model and the nonlinearity of the inverse model. We conclude that: (1) SOP-homo runs much faster than the SOP/OP-inhomo since the homogeneous background Green's function is applied. (2) For the scatterers with lower contrast than the obstacles, SOP-homo outperforms SOP/OP-inhomo (due to the accuracy of Green's function), whereas for the higher contrast case, the SOP-homo is inferior to the SOP/OP-inhomo (due to the nonlinearity of model).

We also highlight two points. Firstly, although the accuracy of the numerical Green's function can be easily improved by reducing the grid step length, this will also deteriorate the computational burden and increase the computing time severely. Thus, a balance between the two factors (accuracy of Green's function and nonlinearity of model) should be considered in actual situation to choose proper method for such kind of problems. Secondly, although the SOP-homo is introduced in the framework of SOM, other methods based on the field-state equation can also be reformulated to solve such kind of problems as long as the cost function is constructed in a similar form.

4.2 SOP for mixed boundary problem

In practical civil through wall imaging problems, the walls (obstacles) are always embedded with steel rods inside and the walls are commonly separable from the scatterers. Besides, the scatterers enclosed by the obstacle can also be the mixture of PEC and dielectric. Such problems can be cast into the mixed boundary SOP. Most published works deal only with the dielectric obstacles. Therefore investigation of the mixed boundary SOP is of practical importance. Unlike the previous section which focuses mainly on the comparison between SOP-homo and the contemporary works, this section will mainly focus on the realization of solving the mixed boundary SOP.

In this section, to solve the mixed boundary SOP, the *T*-matrix SOM is reformulated based on the idea of SOP-homo, i.e., the *separable* obstacle is treated as a ‘known scatterer’ rather than part of the background. Thus the background medium remains as free space. In addition, the elements corresponding to the obstacle can be excluded from the updating process of the *T*-matrices by reformulating the cost function. For convenience, we call the newly developed method *T*-matrix SOP-homo.

Several numerical examples are given to prove the validity of the *T*-matrix SOP-homo. The results indicate that the SOP-homo can be extended to the *T*-matrix method. The *T*-matrix SOP-homo is able to solve the mixed boundary SOP and is quite robust against noise.

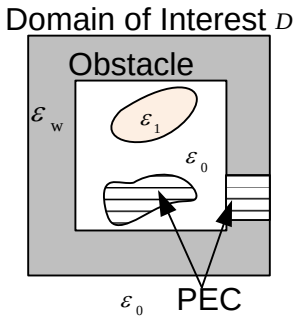

Fig. 4-9: A general scenario for mixed boundary SOP.

4.2.1 Forward problem

As depicted in Fig. 4-9, inside the domain of interest D, the dielectric part of obstacle is of relative permittivity ε_w and PEC rods are embedded inside. The physical properties of the wall are known *a priori*. Scatterers enclosed inside the obstacle can be either dielectric or PEC. N_{inc} plane waves symmetrically illuminate the domain of interest around a circle. Then the scattered field is received by N_r antennas evenly distributed on a circle outside the domain of interest. Thus there are totally $N_r \times N_{inc}$ points of data recorded in the scattered field matrix. We discretize the domain of interest into N square subunits. The number of subunits that belong to the wall is N_w.

Two equations describe the scattering behavior of the scatterers in *T*-matrix model: the state equation and the field equation,

$$\bar{\mathbf{a}} = \hat{O} \cdot \bar{\mathbf{e}} - \hat{O} \cdot \bar{\bar{A}} \cdot \bar{\mathbf{a}} \tag{4.14}$$

$$\mathbf{E}_z^{sca} = \bar{\boldsymbol{\psi}}^t \cdot \bar{\mathbf{a}} \tag{4.15}$$

where $\bar{\boldsymbol{\psi}}^t$ denotes the matrix of multipoles, and $\bar{\mathbf{a}}$ is the vector of amplitudes of induced multipoles. $\hat{O}$ is the combination of all the *T*-matrices for each subunit, with $\bar{\bar{T}}_i, \quad i = 1, 2, \ldots, N$ arranged along its diagonal. $\bar{\bar{A}}$ the translational matrix. $\bar{\mathbf{e}}$ is the

vector for the coefficients of the incident field. The expressions of all the parameters are same with Chapter 3.

In Equs. (4.14) and (4.15), definitions of the mapping operators are changed. $\bar{\bar{\psi}}^{t}$ and $\bar{\bar{A}}$ works similarly to the matrices of Green's function $\bar{\bar{G}}_{s}$ and $\bar{\bar{G}}_{D}$ as in original SOM. However $\bar{\bar{\psi}}^{t}$ is the mapping from the amplitude of induced multipoles to the scattered field on receivers and $\bar{\bar{A}}$ is the mapping to transform the scattered field from other scatterers into a form of the incident field to one scatterer. Whereas in the SOM, the $\bar{\bar{G}}_{s}$ and $\bar{\bar{G}}_{D}$ are the mappings from induced current to the scattered fields outside and inside the domain of interest respectively.

Similar to $\bar{\bar{G}}_{s}$ and $\bar{\bar{G}}_{D}$, $\bar{\bar{\psi}}^{t}$ and $\bar{\bar{A}}$ also require extra calculation if the obstacle is seen as part of the inhomogeneous background. While if we apply the SOP-homo and treat the wall as 'known scatterer' rather than part of the background, $\bar{\bar{\psi}}^{t}$ and $\bar{\bar{A}}$ remain simply as the analytical expressions for free space.

4.2.2 Inverse problem

The inverse scattering problem consists of determining the unknown scatterers located inside the obstacle given the scattered field and the incident field data. Two optimization processes are involved in solving the mixed boundary inverse problem. The first optimization process retrieves the *T*-matrices or matrix $\hat{O}$ from the scattered field matrix. The reformulated SOM, i.e., SOP-homo is adopted as the optimization scheme. Then after classifying the PEC from dielectric subunits by using the monopole term of *T*-matrix, the second optimization process retrieves the relative permittivity from the *T*-matrix by using the LM algorithm. Throughout the whole

optimization processes, the information of the separable obstacle is known as *a priori* information and the corresponding subunits are excluded from the updating process. Thus number of unknowns is further reduced.

Similar to Section 3.3.1, the objective function is defined to be

$$f\left(\hat{O}\right)=\frac{1}{2}\sum_{p=1}^{N_{\text{inc}}}\left(\frac{\Delta^{\text{fie}}}{\left\|\bar{E}^{\text{sca}}\right\|^2}+\frac{\Delta^{\text{sta}}}{\left\|\bar{\mathbf{a}}^{\text{s}}\right\|^2}\right) \tag{4.16}$$

Here $\bar{\mathbf{a}}^{\text{s}}$ is the determined part of vector $\bar{\mathbf{a}}$ defined by SOM, $\bar{\mathbf{a}}=\bar{\mathbf{a}}^{\text{s}}+\bar{\mathbf{a}}^{\text{n}}$ and $\bar{\mathbf{a}}^{\text{n}}$ needs to be solved by optimization. The field residue Δ^{fie} is defined by the residue in the field equation Eq.(4.15),

$$\Delta^{\text{fie}}=\left\|\bar{\boldsymbol{\psi}}^{\text{t}}\cdot\bar{\mathbf{a}}^{\text{s}}+\bar{\boldsymbol{\psi}}^{\text{t}}\cdot\bar{\bar{V}}^{\text{n}}\cdot\bar{\alpha}^{\text{n}}-\bar{E}^{\text{sca}}\right\|^2, \tag{4.17}$$

And state equation Δ^{sta} is define by the residue in the state equation Eq.(4.14),

$$\Delta^{\text{sta}}=\left\|\bar{\mathbf{a}}-\hat{O}\cdot\bar{e}+\hat{O}\cdot\bar{\bar{A}}\cdot\bar{\mathbf{a}}\right\|^2. \tag{4.18}$$

A. Optimization 1.

The SOM is chosen as the optimization scheme, i.e. alternatively update $\bar{\mathbf{a}}^{\text{n}}$ and the $\hat{O}$ matrix. The algorithm is briefly presented below. Here $\hat{O}_n$ denotes the matrix $\hat{O}$ in the nth iteration step, and $\bar{\mathbf{a}}^{\text{n}}_{p,n}$ denotes the matrix $\bar{\mathbf{a}}^{\text{n}}_{p}$, $p=1,2,\ldots,N_{\text{inc}}$ in the nth step of iteration.

Step 1: Data preparation

Step 2: Initialization: $n=0$.

Step 3: updating process: $n=n+1$.

Step 3.1: Update $\bar{\mathbf{a}}^{\text{n}}_{p,n}$, while regarding $\hat{O}_n$ as a known parameter.

Step 3.2: Update $\hat{O}_n$, while regarding $\bar{\mathbf{a}}_{p,n}^{\mathrm{n}}$ as a known parameter:

Step 4: If termination condition is satisfied, stop iteration. Otherwise, go to Step 3.

Since no scatterers overlap with the obstacles, the subunits corresponding to the obstacle can be fixed throughout the whole updating process. Therefore the number of unknowns in matrix $\hat{O}$ is actually $(2M+1)(N-N_{\mathrm{w}})$, where M is the truncation number of multipoles chosen to represent the multiple scattering effect of each subunit and $N-N_{\mathrm{w}}$ is the number of non-obstacle subunits. In step 1 and 2 of the updating algorithm, the initial guess of $\hat{O}$ needs to be modified according to the prior information of the obstacle.

A mathematical reformulation to the objective function can be applied in step 3.2 to further reduce the number of unknowns. We can split the objective function into three parts: the field residue $\left(\Delta_{p,n}^{\mathrm{fie}}\right)$, the state residue corresponding to the obstacle subunits $\left(\Delta_{p,n}^{\mathrm{sta}}\right)^{\mathrm{obs}}$ and the state residue corresponding to the non- obstacle subunits $\left(\Delta_{p,n}^{\mathrm{sta}}\right)^{\text{non-obs}}$, i.e.,

$$f\left[\left(\hat{O}_n\right)_i\right]=\frac{1}{2}\sum_{p=1}^{N_{\mathrm{inc}}}\left(\frac{\Delta_{p,n}^{\mathrm{fie}}}{\left\|\bar{E}_p^{\mathrm{sca}}\right\|^2}+\sum_{i=1}^{(2M+1)N_{\mathrm{w}}}\frac{\left(\Delta_{p,n}^{\mathrm{sta}}\right)_i^{\mathrm{obs}}}{\left\|\bar{\mathbf{a}}_p^{\mathrm{s}}\right\|^2}+\sum_{i=1}^{(2M+1)(N-N_{\mathrm{w}})}\frac{\left(\Delta_{p,n}^{\mathrm{sta}}\right)_i^{\text{non-obs}}}{\left\|\bar{\mathbf{a}}_p^{\mathrm{s}}\right\|^2}\right). \quad (4.19)$$

On the right hand side of Eq. (4.19), the first two terms are constant with respect to the unknowns (the non-obstacle elements). Thus, only the last term contributes to the CG updating of the unknowns, i.e., $\hat{O}_i,\quad i=1,2,\ldots,(2M+1)(N-N_{\mathrm{w}})$. The details of updating $\hat{O}_i$ are similar to Section 3.3.1 but with a less number of unknowns.

B. Optimization 2

After $\hat{O}$ is retrieved by the first optimization process, we adopt the criterion indicated in Section 3.3.1 to classify PEC from dielectric subunits. After classifying the properties of the scatterers, another step of optimization is needed to retrieve the relative permittivity of dielectric scatterers from the *T*-matrix.

The second step of optimization is the same as Section 3.3.1, where the LM algorithm is applied to solve the univariate problem. We omit the details here and refer the reader to Section 3.3.1 for details.

4.2.3 Numerical Examples

The domain of interest for all the numerical examples under investigation is a square of size $2\lambda \times 2\lambda$, which is discretized into $N = 45 \times 45$ square subunits. $N_{\text{inc}} = 10$ plane incident waves are evenly distributed on $[0, 2\pi)$. N_{r}=30 receivers are symmetrically located around a circle of radius 5λ. To avoid the inverse crime, the multipole numbers used in getting the forward data is more than that used in the inverse part. The synthetic data is calculated by *T*-matrix method with $M = 2$ and 10% white Gaussian noise is added into the scattered field. In the inverse problem, $M = 1$ is chosen as the truncation number of the multipoles. $\varepsilon_{\text{r}} = 0$ is used to mark the PEC scatterers in the reconstructed patterns. The singular value spectrum for $\bar{\boldsymbol{\Psi}}^t$ is drawn in Fig. 4-10, and in all the numerical examples the number of leading singular values is chosen to be 10.

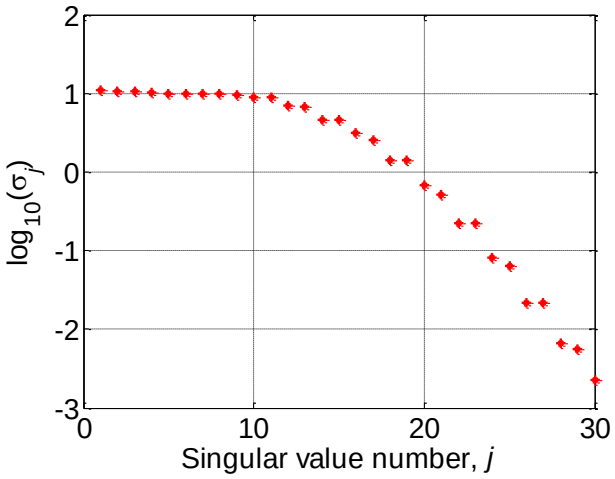

Fig. 4-10 Singular value spectrum for $\bar{\boldsymbol{\psi}}^t$

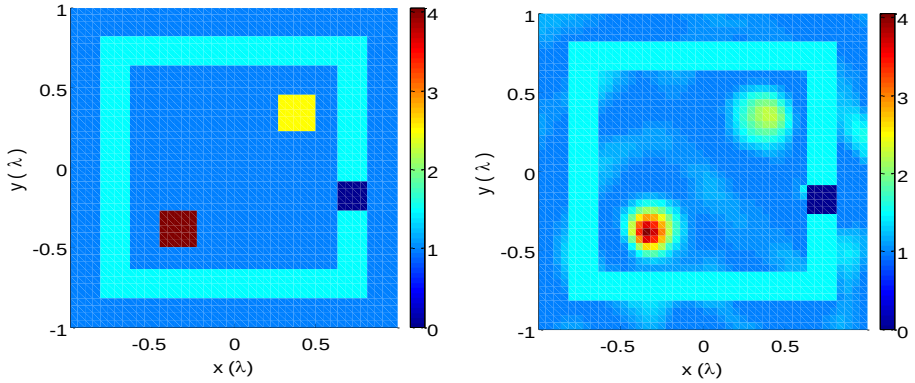

(a) (b)

Fig.4-11. The configuration of scatterer in the first numerical example. The scattering data are contaminated with 10% white Gaussian noise. (a) Exact profile. (b) Reconstructed profile by SOP-homo.

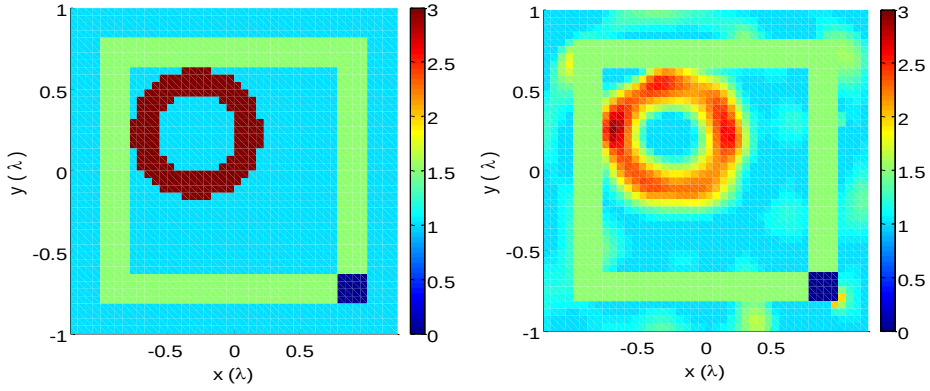

(a) (b)

Fig. 4-12. The configuration of scatterer in the second numerical example. The scattering data are contaminated with 10% white Gaussian noise. (a) Exact profile. (b) Reconstructed profile by SOP-homo.

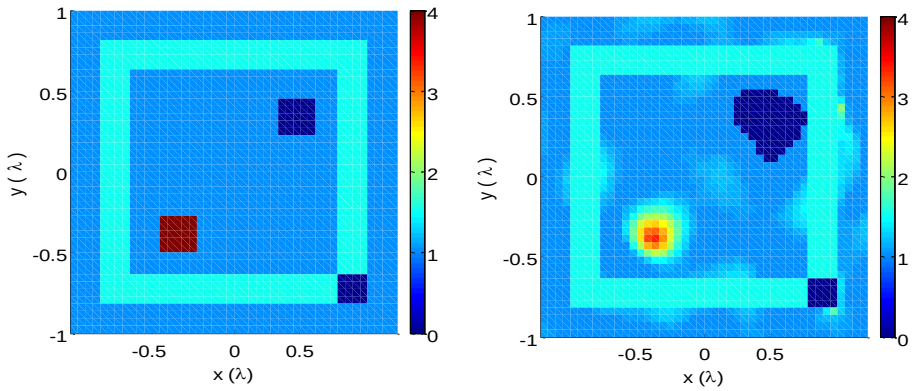

(a) (b)

Fig. 4-13. The configuration of scatterer in the third numerical example. The scattering data are contaminated with 10% white Gaussian noise. (a) Exact profile. (b) Reconstructed profile by SOP-homo.

In the first numerical example the obstacle is square shaped, with the outer side length 1.63λ and the inner side length 1.26λ. The relative permittivity for the dielectric part of obstacle is 1.5. There is one small square metallic rod embedded in the right part of the obstacle, as shown in Fig.4-11 (a). Two square unknown dielectric scatterers are enclosed by the obstacle, with the relative permittivities of 2.5 and 4 respectively. From Fig.4-11 (b), we see that the proposed method has clearly recognized the relative permittivities as well as the positions of the scatterers. The influence of the PEC rod to the reconstruction result is quite small which can be explained by the action of excluding the obstacle from the updating process.

In the second example, a more complicated unknown scatterer is used to test the reconstruction ability of the proposed method. An annulus with the outer radii 0.4λ and inner radii 0.25λ, is located at $(-0.25\lambda, 0.25\lambda)$ in the domain of interest. The relative permittivity of the annulus is 3. The shape and relative permittivity of the obstacle remain the same as the first example except that the square PEC rod is in the right down corner. From the reconstruction result as shown in Fig. 4-12(b), we can

see that despite of the existence of the PEC rod, the annulus shaped scatterer is still successfully reconstructed with the hole clearly seen.

Lastly, we test the algorithm for mixed boundary obstacle as well as the mixed boundary scatterers. The obstacle remains the same as example two. There are two scatterers placed inside the domain of interest as shown in Fig. 4-13(a), one is a square dielectric scatterer with $\varepsilon_r = 4$ and the other is a square shaped PEC scatterer. From Fig. 4-13(b), we can clearly see the PEC scatterer and the spatial distribution of the relative permittivity for the dielectric scatterer. The reconstructed PEC scatterer is blurred due to the expansion of the *T*-matrix to the free space, which is reasonable considering the nature of continuous type optimization scheme.

4.2.4 Summary

The SOP-homo is successfully applied to the *T*-matrix model to solve the mixed boundary SOP. A mathematical reformulation is applied to the *T*-matrix SOM to solve the SOP. The mapping operators remain as the analytical form for free space due to the usage of separable information of the obstacle. The elements corresponding to the obstacle are excluded from the updating process of *T*-matrices. Numerical results indicate that the *T*-matrix SOP-homo works well for the mixed boundary SOP and is quite robust against noise.

5 Conclusion

5.1 Summary of contributions

Three types of problems were studied in this thesis, namely, the PEC inverse scattering problem, the mixed boundary inverse problem, and the SOP. All these problems have been successfully solved by SOM. The essence of original SOM lies in decomposing the induced current into deterministic and ambiguous part. Whereas the deterministic part is obtained by SVD to the mapping operator which maps the induced current to the scattered field on receivers, the ambiguous part is obtained by solving an optimization problem in which the searching dimension is smaller than that of the original problem. This thesis has successfully extended the SOM to these three types of problems. Various numerical results are given to prove the validity of the proposed methods. The conclusions for these three types of problems are made as follows:

1) This thesis has successfully extended the application of SOM from dielectric to PEC scatterers. We have realized the simultaneous reconstruction of both line shape and closed-contour PEC scatterers under the EFIE model, without requiring any prior information on the number or approximate locations of the scatterers. One main contribution of the work is the representation of the scatterers, i.e., using side edges of the square mesh rather than the square itself, which enables the modeling of both line shape and closed contour objects. Proposing the model of the relative state residue is another main contribution

of the work which is realized by the introduction of a binary shape function indicating the property of the subunits.

A. In discrete-type SOM, the shape function is binary, and the optimization problem is a discrete one. This is different from the dielectric case which is a continuous type optimization problem. The optimization method used is the steepest descent method. The discrete-type SOM has several good properties, such as taking just a few steps of iteration to converge and being able to reconstruct both closed-contour and line-shape PEC scatterers.

B. The continuous-type SOM is realized by approximating the binary vector into a function of another real valued and thus continuous changing variable. The alternative two-step CG optimization method is adopted as the optimization scheme for this continuous variable problem. Further investigation of the smooth behavior of regularization term has proved the robustness of the continuous-type SOM. The continuous-type SOM is found to be more robust and time saving than the discrete-type SOM.

2) This thesis has extended the application of SOM to the *T*-matrix method to solve the mixed boundary problem. To represent both the PEC and dielectric scatterers by a uniform volume based model, the *T*-matrix method is chosen as the modeling scheme. Truncation number of the multipole terms has been investigated to accurately model the forward problem. Two steps of optimization processes are necessary to retrieve the *T*-matrix and relative

permittivity respectively. The amplitude of the induced multipoles in the *T*-matrix method works similarly to the induced current in original SOM, which is thus decomposed into the deterministic part and ambiguous part by analyzing the singular value spectrum of the mapping from the amplitude of the induced multipoles to the scattered field. Therefore the deterministic part serves as an initial guess to the amplitude of induced multipoles and reduces the dimension of unknowns in the alternative two-step CG optimization. After the first optimization process, the properties of the subunits are distinguished by the monopole term of *T*-matrix. In addition, another univariate optimization is carried out to retrieve the refraction index for the dielectric scatterers, which conserves the nonlinearity between the *T*-matrix coefficients and refraction index. The PEC and dielectric scatterers are reconstructed simultaneously by using the *T*-matrix method, without *a priori* information on the property or number and shape of the scatterers. The proposed *T*-matrix SOM also inherits the good properties of the original SOM, i.e., fast convergence, robust against noise, and high-resolution imaging ability.

3) Lastly, this thesis has extended the application of SOM to the SOP, a commonly encountered practical problem where the obstacle is separable from the unknown scatterers. The key point in solving the SOP lies in the usage of the prior information of the separable obstacle, so as to treat the obstacle as a known scatterer rather than part of the inhomogeneous background. Thus the background is homogeneous and the subunits corresponding to the obstacle can

be excluded from the retrieving process of the unknowns by properly reformulating the cost function of SOM. The dielectric scatterer SOP is solved by the SOP-homo in the EFIE framework and the mixed boundary SOP is solved by SOP-homo in the *T*-matrix framework. The proposed SOP-homo can be applied to any state-field equation based optimization scheme and is less computational intensive than the contemporary methods for inhomogeneous background.

5.2 Future work and discussion

In summary, the future work involves two points: firstly, the extension of the proposed modeling schemes to the more complicated TE and three dimensional cases; Secondly, the practical application of the proposed method in real life measurements and simulations.

The 2D-TM illumination is the most basic setup for the inverse scattering problem. In practice, many real world problems can be well modeled as the 2D-TM case. In addition, investigation on 2D-TM case provides a theoretical guidance to both the 2D-TE and the 3D cases. There are several challenges lying in extending the proposed models to the 2D-TE case and 3D case.

When implementing the model proposed for PEC to the 2D-TE case, induced currents flow in the transverse direction and one should be careful in choosing the basis for current to avoid discontinuities at the sharp corners or tips of scatterers.

When implementing the PEC SOM to the 3D case, careful study should be paid on the basic elements representing the PEC scatterers.

The *T*-matrix SOM can also be implemented to 2D-TE and 3D cases. The dominant multipole terms in *T*-matrices for dielectric scatterers in both cases are dipoles. However due to the surface currents, in 2D-TE case for PEC scatterers, magnetic monopole which is on the same order of the electric dipole should also be considered. While in 3D case for PEC scatterers, magnetic dipole which is on the same order of the electric dipole should be considered. Moreover, the multipole truncation numbers should also be carefully studied to accurately model the scattering behavior of the corresponding mixed boundary problem.

The SOP-homo is a technique of implementing the prior information of separable obstacles for state-field equation type optimization schemes. The SOP-homo can also be implemented to the TE or 3D cases on the condition that the cost function is constructed in a state-field equation form.

In the practical applications such as through wall imaging and geophysics exploration, the distribution of the transmitters and the receivers may not be arranged in a symmetrical way. Instead, the receivers and transmitters are arranged along a line at one side of the domain of interest. In such case the information may not be sufficient enough to guarantee a clear reconstruction. The multiple frequency hopping technology can be applied to improve the solution for the results. Further, the background mediums may not be air in biomedical imaging or geophysics exploration. However, we can utilize the inhomogeneous background Green's function and

represent the scatterers by the contrast as compared to the background medium. Therefore even though the relative permittivities are high for either the background or the scatterers, the contrast of the scatterer to the background is relatively low. The proposed modeling schemes are still applicable as long as the background medium is known. An agreed viewpoint on all these practical issues is to utilize as much available information as possible in the inversion. Practically, certain amount of the prior information can always be guaranteed. SOM is able to incorporate some prior information by constraining the relative permittivity during iterations or modifying the cost function (such as the method in chapter 4). Thus SOM has the potential of acting as a useful inversion tool in practical applications.

REFERENCE

[1] A. Kirsch, *An introduction to the mathematical theory of inverse problems*. New York: Springer Verlag, 1996.

[2] J. Hadamard, Ed., *Lectures on Cauchy's problem in linear partial differential equations*. New Haven, USA, 1923.

[3] D. L. Colton and R. Kress, *Inverse acoustic and electromagnetic scattering theory*, 2nd ed. New York: Springer, 1998.

[4] A. J. Devaney and G. C. Sherman, "Nonuniqueness in Inverse Source and Scattering Problems," *IEEE Transactions on Antennas and Propagation,* vol. 30, pp. 1034-1037, 1982.

[5] R. Lavarello and M. Oelze, "A study on the reconstruction of moderate contrast targets using the distorted born iterative method," *IEEE Transactions on Ultrasonics Ferroelectrics and Frequency Control,* vol. 55, pp. 112-124, Jan 2008.

[6] C. Lu, J. Lin, W. Chew, and G. Otto, "Image reconstruction with acoustic measurement using distorted Born iteration method," *Ultrasonic Imaging,* vol. 18, pp. 140-156, Apr 1996.

[7] R. E. Kleinman and P. M. Vandenberg, "A modified gradient-method for 2-dimensional problems in tomography," *Journal of Computational and Applied Mathematics,* vol. 42, pp. 17-35, Sep 1992.

[8] A. Baussard, K. Belkebir, and D. Premel, "A markovian regularization approach of the Modified Gradient Method for solving a two-dimensional inverse scattering problem," *Journal of Electromagnetic Waves and Applications,* vol. 17, pp. 989-1008, 2003.

[9] K. Belkebir, A. Baussard, and D. Premel, "Edge-preserving regularization scheme applied to the Modified Gradient Method for the reconstruction of two-dimensional targets from laboratory-controlled data," *Progress in Electromagnetics Research,* vol. 54, pp. 1-17, 2005.

[10] K. Belkebir and A. G. Tijhuis, "Modified gradient method and modified Born method for solving a two-dimensional inverse scattering problem," *Inverse Problems,* vol. 17, pp. 1671-1688, Dec 2001.

[11] L. Souriau, B. Duchene, D. Lesselier, and R. E. Kleinman, "Modified gradient approach to inverse scattering for binary objects in stratified media," *Inverse Problems,* vol. 12, pp. 463-481, Aug 1996.

[12] P. M. van den Berg and R. E. Kleinman, "A contrast source inversion method," *Inverse Problems,* vol. 13, pp. 1607-1620, Dec 1997.

[13] P. M. van den Berg, A. L. van Broekhoven, and A. Abubakar, "Extended contrast source inversion," *Inverse Problems,* vol. 15, pp. 1325-1344, Oct 1999.

[14] A. Abubakar, P. M. van den Berg, and J. J. Mallorqui, "Imaging of biomedical data using a multiplicative regularized contrast source inversion method," *IEEE Transactions on Microwave Theory and Techniques,* vol. 50, pp. 1761-1771, Jul 2002.

[15] R. F. Bloemenkamp, A. Abubakar, and P. M. van den Berg, "Inversion of experimental multi-frequency data using the contrast source inversion method," *Inverse Problems,* vol. 17, pp. 1611-1622, Dec 2001.

[16] K. Agarwal, L. Pan, and C. Xudong, "Subspace-Based Optimization Method for Reconstruction of 2-D Complex Anisotropic Dielectric Objects," *IEEE Transactions on*

Microwave Theory and Techniques, vol. 58, pp. 1065-1074, 2010.

[17] X. Chen, "Subspace-based optimization method for solving inverse scattering problems," *IEEE Transactions on Geoscience and Remote Sensing,* vol. 48, pp. 42-49, 2010.

[18] T. Lu, K. Agarwal, Y. Zhong, and X. Chen, "Through-wall imaging: Application of subspace-based optimization method," *Progress in Electromagnetics Research,* vol. 102, pp. 351-366, 2010.

[19] L. Pan, K. Agarwal, Y. Zhong, S. P. Yeo, and X. Chen, "Subspace-based optimization method for reconstructing extended scatterers: transverse electric case," *Journal of Optical Society of America A,* vol. 26, pp. 1932-1937, 2009.

[20] X. Ye, X. Chen, Y. Zhong, and K. Agarwal, "Subspace-based optimization method for reconstructing perfectly electric conductors," *Progress in Electromagnetics Research,* vol. 100, pp. 119-128, 2010.

[21] X. Z. Ye, Y. Zhong, and X. D. Chen, "Reconstructing perfectly electric conductors by the subspace-based optimization method with continuous variables," *Inverse Problems,* vol. 27, May 2011.

[22] Y. Zhong and X. Chen, "Twofold subspace-based optimization method for solving inverse scattering problems," *Inverse Problems,* vol. 25, Aug 2009.

[23] Y. Zhong, X. Chen, and K. Agarwal, "An improved subspace-based optimization method and its implementation in solving three-dimensional inverse problems," *IEEE Transactions on Geoscience and Remote Sensing,* vol. 48, pp. 3763-3768, 2010.

[24] W. C. Chew and Y. M. Wang, "An iterative solution of two-dimensional electromagnetic inverse scattering problem," *International journal of imaging systems and technology,* vol. 1, pp. 100-108, 1989.

[25] W. C. Chew and Y. M. Wang, "Reconstruction of 2-Dimensional Permittivity Distribution Using the Distorted Born Iterative Method," *IEEE Transactions on medical imaging,* vol. 9, pp. 218-225, Jun 1990.

[26] A. Kirsch, "An introduction to the mathematical theory of inverse problems," *Applied Mathematical Sciences,* vol. 120, pp. 14-41, 1996.

[27] N. Bissantz, T. Hohage, and A. Munk, "Consistency and rates of convergence of nonlinear Tikhonov regularization with random noise," *Inverse Problems,* vol. 20, pp. 1773-1789, Dec 2004.

[28] T. Hohage and M. Pricop, "Nonlinear Tikhonov regularization in Hilbert scales for inverse boundary value problems with random noise," *Inverse Problems and Imaging,* vol. 2, pp. 271-290, May 2008.

[29] S. Caorsi and G. L. Gragnani, "Inverse-scattering method for dielectric objects based on the reconstruction of the nonmeasurable equivalent current density," *Radio Science,* vol. 34, pp. 1-8, Jan-Feb 1999.

[30] H. Abdullah and A. K. Louis, "The approximate inverse for solving an inverse scattering problem for acoustic waves in an inhomogeneous medium," *Inverse Problems,* vol. 15, pp. 1213-1229, Oct 1999.

[31] A. Lakhal and A. K. Louis, "Locating radiating sources for Maxwell's equations using the approximate inverse," *Inverse Problems,* vol. 24, Aug 2008.

[32] A. Abubakar, T. M. Habashy, P. M. van den Berg, and D. Gisolf, "The diagonalized contrast source approach: an inversion method beyond the Born approximation," *Inverse Problems,* vol.

21, pp. 685-702, Apr 2005.

[33] A. Abubakar, P. M. van den Berg, and S. Y. Semenov, "A robust iterative method for Born inversion," *IEEE Transactions on Geoscience and Remote Sensing*, vol. 42, pp. 342-354, Feb 2004.

[34] G. Bozza, C. Estatico, M. Pastorino, and A. Randazzo, "Application of an inexact-Newton method within the second-order born approximation to buried objects," *IEEE Geoscience and Remote Sensing Letters*, vol. 4, pp. 51-55, Jan 2007.

[35] A. Brancaccio, G. Leone, and R. Pierri, "Information content of Born scattered fields: results in the circular cylindrical case," *Journal of the Optical Society of America a-Optics Image Science and Vision*, vol. 15, pp. 1909-1917, Jul 1998.

[36] S. Caorsi, A. Costa, and M. Pastorino, "Microwave imaging within the second-order born approximation: Stochastic optimization by a genetic algorithm," *IEEE Transactions on Antennas and Propagation*, vol. 49, pp. 22-31, Jan 2001.

[37] S. Caorsi, G. L. Gragnani, and M. Pastorino, "Microwave imaging by 3-dimensional Born linearization of electromagnetic scattering," *Radio Science*, vol. 25, pp. 1221-1229, Nov-Dec 1990.

[38] A. J. Devaney, "Inversion formula for inverse scattering within the Born approximation," *Optics Letters*, vol. 7, pp. 111-112, 1982.

[39] A. J. Devaney and M. L. Oristaglio, "Inversion procedure for inverse scattering within the distorted-wave Born approximation," *Physical Review Letters*, vol. 51, pp. 237-240, 1983.

[40] T. M. Habashy, M. L. Oristaglio, and A. T. De Hoop, "Simultaneous nonlinear reconstruction of 2-dimensional permittivity and conductivity," *Radio Science*, vol. 29, pp. 1101-1118, Jul-Aug 1994.

[41] T. M. Habashy, E. Y. Chow, and D. G. Dudley, "Profile inversion using the renormalized source-type integral-equation approach," *IEEE Transactions on Antennas and Propagation*, vol. 38, pp. 668-682, May 1990.

[42] M. D'Urso, T. Isernia, and A. F. Morabito, "On the solution of 2-D inverse scattering problems via source-type integral equations," *IEEE Transactions on Geoscience and Remote Sensing*, vol. 48, pp. 1186-1198, Mar 2010.

[43] A. J. Devaney and E. Wolf, "Radiating and nonradiating classical current distributions and fields they generate," *Physical Review. D Part. Fields*, vol. 8, pp. 1044-1047, 1973.

[44] M. Chiappe and G. L. Gragnani, "An analytical approach to the reconstruction of the radiating currents in inverse electromagnetic scattering," *Microwave and Optical Technology Letters*, vol. 49, pp. 354-360, Feb 2007.

[45] L. L. Li, W. J. Zhang, and F. Li, "The Closed-Form Solution to the Reconstruction of the Radiating Current for EM Inverse Scattering," *IEEE Transactions on Geoscience and Remote Sensing*, vol. 47, pp. 361-369, Jan 2009.

[46] P. Rocca, "Multi-resolution retrieval of non-measurable equivalent currents in microwave imaging problems - Experimental assessment," *Progress in Electromagnetics Research*, vol. 96, pp. 267-285, 2009.

[47] P. Rocca, M. Donelli, G. L. Gragnani, and A. Massa, "Iterative multi-resolution retrieval of non-measurable equivalent currents for the imaging of dielectric objects," *Inverse Problems*, vol. 25, May 2009.

[48] X. Chen, "Regularization method in subspace-based optimization method for solving inverse

scattering problems," presented at the IEEE International Symposium on Antennas Propagation, Charleston, SC, USA, June 2009.

[49] X. D. Chen, "Subspace-based optimization method for inverse scattering problems with an inhomogeneous background medium," *Inverse Problems,* vol. 26, Jul 2010.

[50] P. C. Waterman, "Matrix formulation of electromagnetic scattering," *Proc. IEEE,* vol. 53, pp. 805-811, 1965.

[51] J. H. Lin and W. C. Chew, "Solution of the three-dimensional electromagnetic inverse problem by the local shape function and the conjugate gradient fast Fourier transform methods," *Journal of the Optical Society of America A,* vol. 14, pp. 3037-3045, Nov 1997.

[52] A. Z. Elsherbeni and A. A. Kishk, "Modeling of Cylindrical Objects by Circular Dielectric and Conducting Cylinders," *IEEE Transactions on Antennas and Propagation,* vol. 40, pp. 96-99, Jan 1992.

[53] W. C. Chew, L. Gurel, Y. M. Wang, G. Otto, R. L. Wagner, and Q. H. Liu, "A Generalized Recursive Algorithm for Wave-Scattering Solutions in 2 Dimensions," *IEEE Transactions on Microwave Theory and Techniques,* vol. 40, pp. 716-723, Apr 1992.

[54] G. P. Otto and W. C. Chew, "Inverse Scattering of H-Z Waves Using Local Shape-Function Imaging - a T-Matrix Formulation," *International journal of imaging systems and technology,* vol. 5, pp. 22-27, Spr 1994.

[55] R. D. Marger and N. Bleistein, "An examination of the limited aperture problem of physical optics inverse scattering " *IEEE Trans. Antennas Poppa.,* vol. 26, pp. 695-699, 1979.

[56] F. Soldovieri, A. Brancaccio, G. Leone, and R. Pierri, "Shape reconstruction of perfectly conducting objects by multiview experimental data," *IEEE Transactions on Geoscience and Remote Sensing,* vol. 43, pp. 65-71, Jan 2005.

[57] A. Liseno and R. Pierri, "Imaging perfectly conducting objects as support of induced currents: Kirchhoff approximation and frequency diversity," *Journal of the Optical Society of America a-Optics Image Science and Vision,* vol. 19, pp. 1308-1318, Jul 2002.

[58] R. E. Kleinman and P. M. Van der Berg, "Two-dimensional location and shape reconstruction " *Radio Science,* vol. 29, pp. 1157-1169, 1994.

[59] R. Marklein, K. Balasubramanian, K. J. Langenberg, J. Miao, and S. M. Sinaga, "Applied Linear and Nonlinear Scalar Inverse Scattering: A Comparative Study," presented at the XXVIIth General Assembly of the international URSI, Maastricht, Netherlands, 2002.

[60] O. Feron, B. Duchene, and A. Mohammad-Djafari, "Microwave imaging of inhomogeneous objects made of a finite number of dielectric and conductive materials from experimental data," *Inverse Problems,* vol. 21, pp. S95-S115, Dec 2005.

[61] C. Yu, L. P. Song, and Q. H. Liu, "Inversion of multi-frequency experimental data for imaging complex objects by a DTA-CSI method," *Inverse Problems,* vol. 21, pp. S165-S178, Dec 2005.

[62] G. P. Otto and W. C. Chew, "Microwave Inverse Scattering - Local Shape Function Imaging for Improved Resolution of Strong Scatterers," *IEEE Transactions on Microwave Theory and Techniques,* vol. 42, pp. 137-141, Jan 1994.

[63] W. C. Chew and G. P. Otto, "Microwave imaging of multiple conducting cylinders using local shape functions," *IEEE Microwave and Guided Wave Letters,* vol. 2, pp. 284-286, 1992.

[64] T. Takenaka, Z. Q. Meng, T. Tanaka, and W. C. Chew, "Local shape function combined with genetic algorithm applied to inverse scattering for strips," *Microwave and Optical Technology*

Letters, vol. 16, pp. 337-341, Dec 1997.

[65] Z. Q. Meng, T. Takenaka, and T. Tanaka, "Image reconstruction of two-dimensional impenetrable objects using genetic algorithm," *Journal of Electromagnetic Waves and Applications*, vol. 13, pp. 95-118, 1999.

[66] C. C. Chiu and P. T. Liu, "Image reconstruction of a perfectly conducting cylinder by the genetic algorithm," *IEE Proceedings of Microwaves Antennas and Propagation*, vol. 143, pp. 249-253, Jun 1996.

[67] A. Qing and C. K. Lee, "Microwave imaging of a perfectly conducting cylinder using a real-coded genetic algorithm," *IEE Proceedings-Microwaves Antennas and Propagation*, vol. 146, pp. 421-425, Dec 1999.

[68] A. Y. Oing, "Microwave imaging of parallel perfectly conducting cylinders," *International Journal of Imaging Systems and Technology*, vol. 11, pp. 365-371, 2000.

[69] A. Y. Qing, "An experimental study on electromagnetic inverse scattering of a perfectly conducting cylinder by using the real-coded genetic algorithm," *Microwave and Optical Technology Letters*, vol. 30, pp. 315-320, Sep 2001.

[70] A. Y. Qing, "Electromagnetic inverse scattering of multiple two-dimensional perfectly conducting objects by the differential evolution strategy," *IEEE Transactions on Antennas and Propagation*, vol. 51, pp. 1251-1262, Jun 2003.

[71] A. Y. Qing, "Electromagnetic inverse scattering of multiple perfectly conducting cylinders by differential evolution strategy with individuals in groups (GDES)," *IEEE Transactions on Antennas and Propagation*, vol. 52, pp. 1223-1229, May 2004.

[72] W. Chien and C. C. Chiu, "Cubic-spline expansion with GA for a partially immersed conducting cylinder," in *International Conference on Wireless Communications and Applied Computational Electromagnetics*, Honolulu, HI, 2005, pp. 2223-2228.

[73] W. Chien and C. C. Chiu, "Using NU-SSGA to reduce the searching time in inverse problem of a buried metallic object," *IEEE Transactions on Antennas and Propagation*, vol. 53, pp. 3128-3134, Oct 2005.

[74] W. Chien and C. C. Chiu, "Cubic-spline expansion with GA for half-space inverse problems," *Applied Computational Electromagnetics Society Journal*, vol. 20, pp. 136-143, Jul 2005.

[75] W. Chien, C. H. Huang, and C. C. Chiu, "Cubic-spline expansion for a two-dimensional periodic conductor in free space," *International Journal of Applied Electromagnetics and Mechanics*, vol. 24, pp. 105-114, 2006.

[76] W. Chien, C. C. Chiu, and C. L. Li, "Cubic-spline expansion for a conducting cylinder buried in a slab medium," *Electromagnetics*, vol. 26, pp. 329-343, Jul 2006.

[77] R. Kress, "Inverse Scattering from an Open Arc," *Mathematical Methods in the Applied Sciences*, vol. 18, pp. 267-293, Apr 10 1995.

[78] A. Kirsch and S. Ritter, "A linear sampling method for inverse scattering from an open arc," *Inverse Problems*, vol. 16, pp. 89-105, Feb 2000.

[79] F. Cakoni and D. Colton, "The linear sampling method for cracks," *Inverse Problems*, vol. 19, pp. 279-295, Apr 2003.

[80] A. F. Peterson, S. L. Ray, and R. Mittra, *Computational methods for electromagnetics*. New York: IEEE Press, 1998.

[81] X. Chen, "Application of signal-subspace and optimization methods in reconstructing extended scatterers," *Journal of the Optical Society of America A*, vol. 26, pp. 1022-1026, Apr

2009.

[82] X. Chen, "Signal-subspace method approach to the intensity-only electromagnetic inverse scattering problem," *Journal of the Optical Society of America A*, vol. 25, pp. 2018-2024, Aug 2008.

[83] R. A. Horn and C. R. Johnson, *Matrix analysis*. Cambridge; New York: Cambridge University Press, 1985.

[84] X. Z. Ye and X. D. Chen, "The Role of Regularization Parameter of Subspace-based Optimization Method in Solving Inverse Scattering Problems," *Apmc: 2009 Asia Pacific Microwave Conference, Vols 1-5*, pp. 1549-1552, 2009.

[85] B. Duchene and D. Lesselier, "On modified-gradient solution methods using the binary aspect of the unknown electromagnetic parameters and their application to the Ipswich data," *IEEE Antennas and Propagation Magazine*, vol. 38, pp. 45-47, Jun 1996.

[86] L. P. Song, C. Yu, and Q. H. Liu, "Through-wall imaging (TWI) by radar: 2-D tomographic results and analyses," *Ieee Transactions on Geoscience and Remote Sensing*, vol. 43, pp. 2793-2798, Dec 2005.

[87] A. Qing, C. K. Lee, and L. Jen, "Electromagnetic inverse scattering of two-dimensional perfectly conducting objects by real-coded genetic algorithm," *IEEE Transactions on Geoscience and Remote Sensing*, vol. 39, pp. 665-676, Mar 2001.

[88] C. C. Chiu, C. L. Li, and W. Chan, "Image reconstruction of a buried conductor by the genetic algorithm," *IEICE Transactions on Electronics*, vol. E84C, pp. 1946-1951, Dec 2001.

[89] C. C. Chiu and W. T. Chen, "Inverse scattering of a buried imperfect conductor by the genetic algorithm," *International Journal of Imaging Systems and Technology*, vol. 11, pp. 355-360, 2000.

[90] M. Abramowitz and I. A. Stegun, *Handbook of mathematical functions with formulas, graphs, and mathematical tables*. Washington: , U.S. Govt. Print. Off., 1964.

[91] M. A. Fiddy and M. Testorf, "Inverse scattering method applied to the synthesis of strongly scattering structures," *Optics express*, vol. 14, pp. 2037-2046, Mar 6 2006.

[92] R. J. He, L. Y. Rao, S. Liu, W. L. Yan, P. A. Narayana, and H. Brauer, "The method of maximum mutual information for biomedical electromagnetic inverse problems," *IEEE Transactions on Magnetics*, vol. 36, pp. 1741-1744, Jul 2000.

[93] S. M. Ali, N. K. Nikolova, and M. H. Bakr, "Non-destructive testing and evaluation utilizing frequency-domain EM modeling," *Proceedings of the Second IASTED International Conference on Antennas, Radar, and Wave Propagation*, pp. 29-34, 2005.

[94] J. H. Shen, X. D. Chen, Y. Zhong, and L. X. Ran, "Inverse scattering problem in presence of a conducting cylinder," *Optics express*, vol. 19, pp. 10698-10706, May 23 2011.

[95] P. C. Chaumet, K. Belkebir, and R. Lencrerot, "Three-dimensional optical imaging in layered media," *Optics Express*, vol. 14, pp. 3415-3426, Apr 2006.

[96] A. Abubakar, W. Hu, P. M. van den Berg, and T. M. Habashy, "A finite-difference contrast source inversion method," *Inverse Problems*, vol. 24, Dec 2008.

[97] M. Dehmollaian, M. Thiel, and K. Sarabandi, "Through-the-Wall Imaging Using Differential SAR," *IEEE Transactions on Geoscience and Remote Sensing*, vol. 47, pp. 1289-1296, May 2009.

[98] A. J. Devaney and R. P. Porter, "Holography and the Inverse Source Problem .2. Inhomogeneous-Media," *Journal of the Optical Society of America a-Optics Image Science*

and Vision, vol. 2, pp. 2006-2012, 1985.

[99] J. M. Tualle, J. Prat, E. Tinet, and S. Avrillier, "Real-space Green's function calculation for the solution of the diffusion equation in stratified turbid media," *Journal of the Optical Society of America a-Optics Image Science and Vision*, vol. 17, pp. 2046-2055, Nov 2000.

[100] S. Y. He, L. Zhuang, F. Zhang, W. D. Hu, and G. Q. Zhu, "Investigation of range profiles from buried 3-D object based on the EM simulation," *Optics express*, vol. 19, pp. 12291-12304, Jun 20 2011.

[101] S. Caorsi, A. Massa, M. Pastorino, M. Raffetto, and A. Randazzo, "Detection of buried inhomogeneous elliptic cylinders by a memetic algorithm," *IEEE Transactions on Antennas and Propagation*, vol. 51, pp. 2878-2884, Oct 2003.

[102] W. C. Chew, *Waves and fields in inhomogeneous media*, 2nd ed. New York: IEEE Press, 1995.

[103] J. A. Kong, *Electromagnetic wave theory*. New York: John Wiley and Sons, 1990.

[104] O. M. Bucci, N. Cardace, L. Crocco, and T. Isernia, "Degree of nonlinearity and a new solution procedure in scalar two-dimensional inverse scattering problems," *Journal of the Optical Society of America A*, vol. 18, pp. 1832-1843, Aug 2001.

APPENDIX I

Derivation of the translational addition theorem

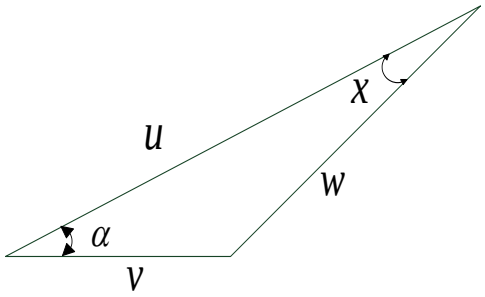

Fig. 6-1 Graf's Law

With the condition of $(|ve^{\pm i\alpha}| < |u|)$, the Graf's law is expressed as page 263 in [90],

$$\begin{matrix} \varsigma_V(w)\cos Vx \\ \sin Vx \end{matrix} = \sum_{n=-\infty}^{n=\infty} \begin{matrix} \varsigma_{V+n}(u)J_n(v)\cos n\alpha \\ \sin n\alpha \end{matrix} \tag{6.1}$$

To derive the translational addition theorem under the cylindrical coordinate, we draw one triangle with the vertexes located at $(\mathbf{r}, \mathbf{r}_j, \mathbf{r}_i)$ in a cylindrical coordinate as shown in Fig.6-2. The vectors of the three edges can be expressed as the subtraction of the vectors denoting the vertexes.

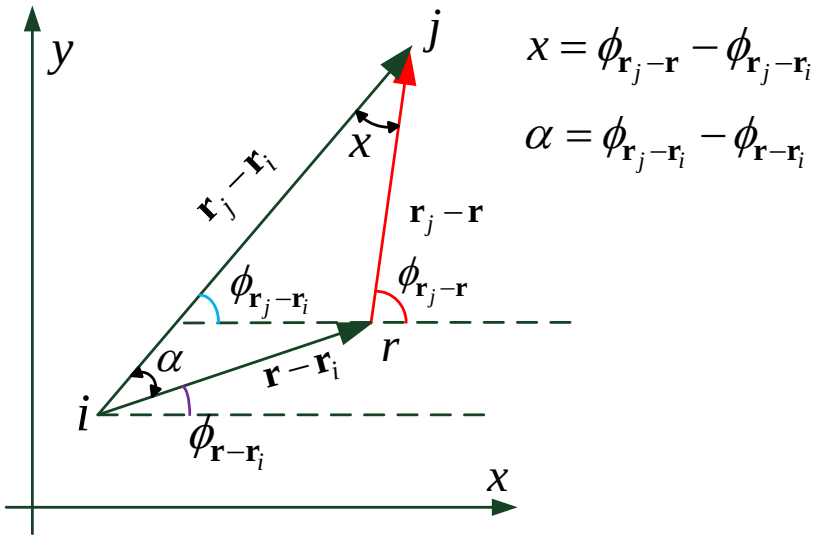

Fig.6-2 Two dimensional addition theorem

The condition for writing this addition theorem from the Graf's law is $|r-r_i|<|r_j-r_i|$,

The angle $\phi_{\mathbf{r}_j-\mathbf{r}_i}$ is the angle of point j made with the x-axis of local coordinate of point i. The angle $\phi_{\mathbf{r}-\mathbf{r}_i}$ is the angle of point r made with the x-axis of local coordinate of point i. The angle $\phi_{\mathbf{r}-\mathbf{r}_j}$ is the angle of point r made with the x-axis of local coordinate of point j.

The addition theorem in this case can be written as:

$$H_m^{(1)}(|r-r_j|)\mathrm{e}^{-im(x=\phi_{r_j-r}-\phi_{r_j-r_i})}=\sum_{n=-\infty}^{n=\infty}H_{n+m}^{(1)}(|r_j-r_i|)J_n(|r-r_i|)\mathrm{e}^{-in(\alpha=\phi_{r_j-r_i}-\phi_{r-r_i})}$$

$$H_m^{(1)}(|r-r_j|)\mathrm{e}^{-im\phi_{r_j-r}}=\sum_{n=-\infty}^{n=\infty}H_{n+m}^{(1)}(|r_j-r_i|)\mathrm{e}^{-i(m+n)\phi_{r_j-r_i}}\bullet J_n(|r-r_i|)\mathrm{e}^{in(\phi_{r-r_i})}$$

m=-m →

$$H_{-m}^{(1)}(|r-r_j|)\mathrm{e}^{im\phi_{r_j-r}}=\sum_{n=-\infty}^{n=\infty}H_{n-m}^{(1)}(|r_j-r_i|)\mathrm{e}^{-i(n-m)\phi_{r_j-r_i}}\bullet J_n(|r-r_i|)\mathrm{e}^{in(\phi_{r-r_i})}$$

$$H_{-m}^{(1)}(Q)=H_m^{(1)}(Q)\bullet e^{im\pi}\qquad \phi_{r_j-r}=\phi_{r-r_j}+\pi$$

$$H_m^{(1)}(|r-r_j|)\mathrm{e}^{im\phi_{r-r_j}}=\sum_{n=-\infty}^{n=\infty}H_{n-m}^{(1)}(|r_j-r_i|)\mathrm{e}^{-i(n-m)\phi_{r_j-r_i}}\bullet J_n(|r-r_i|)\mathrm{e}^{in(\phi_{r-r_i})}\qquad(6.2)$$

Equation (6.2) is the final format of the translational addition theorem.

We can also write it into the regular form

$$J_m^{(1)}(|r-r_j|)\,\mathrm{e}^{im\phi_{r-r_j}} = \sum_{n=-\infty}^{n=\infty} J_{n-m}^{(1)}(|r_j-r_i|)\,\mathrm{e}^{-i(n-m)\phi_{r_j-r_i}} \bullet J_n(|r-r_i|)\,\mathrm{e}^{in(\phi_{r-r_i})} \qquad (6.3)$$

APPENDIX II

Derivation of the small term expansion for the *T*-matrix

From page 360 in [90], when ν is fixed and $z \to 0$, the ascending series for the Bessel functions of integer order is written as,

$$J_\nu(z) \sim (\frac{1}{2}z)^\nu \sum_{k=0}^{\infty} \frac{(-\frac{1}{4}z^2)^k}{k!\Gamma(\nu+k+1)} \tag{7.1}$$

$$\begin{aligned} Y_n(z) = & -\frac{(\frac{1}{2}z)^{-n}}{\pi} \sum_{k=0}^{n-1} \frac{(n-k-1)!}{k!} (\frac{1}{4}z^2)^k \\ & + \frac{2}{\pi} \ln(\frac{1}{2}z) J_n(z) \\ & - \frac{(\frac{1}{2}z)^n}{\pi} \sum_{k=0}^{\infty} \{\psi(k+1) + \psi(n+k+1)\} \frac{(\frac{1}{4}z^2)^k}{k!(n+k)!} \end{aligned} \tag{7.2}$$

For approximation, we only take the low power terms. Such that we have

$$J_0(z) = 1 - \frac{z^2}{4} \tag{7.3}$$

$$J_1(z) = \frac{z}{2} - \frac{z^3}{16} \tag{7.4}$$

$$H_0^{(1)}(z) = \frac{2i}{\pi} \ln z \tag{7.5}$$

$$H_1^{(1)}(z) = -\frac{2i}{\pi z} \tag{7.6}$$

$$J_n(z) = (\frac{1}{2}z)^n \frac{1}{\Gamma(n+1)} \tag{7.7}$$

Where $\Gamma(n) = (n-1)!$. Also from [90],

$$H_n^{(1)}(z) \sim iY_n(z) \sim -\frac{i}{\pi}(\frac{1}{2}z)^{-n}(n-1)! \tag{7.8}$$

The recurrence relationship is as follows, where ζ can be replaced by $J, H^{(1)}$

$$\zeta_n'(z) = -\zeta_{n+1}(z) + \frac{n}{z}\zeta_n(z) \tag{7.9}$$

TM incident case:

$$[T]_n = \frac{xJ_n(z)J_n'(xz) - J_n(xz)J_n'(z)}{H_n^{(1)'}(z)J_n(xz) - vJ_n'(xz)H_n^{(1)}(z)} \tag{7.10}$$

Where $x = \sqrt{\varepsilon_r}$ and $z = k_0 R \to 0$ (assume fine discretization). Plug equation (7.9) into the numerator (N) and denominator (D) of (7.10) we get,

$$\mathbf{N} = J_n(xz)J_{n+1}(z) - xJ_n(z)J_{n+1}(xz) \tag{7.11}$$

$$\mathbf{D} = xJ_{n+1}(xz)H_n^{(1)}(z) - H_{n+1}(z)J_n(xz) \tag{7.12}$$

When $n \geq 1$ we put (7.8) and (7.7) into the numerator and denominator,

$$\begin{aligned} \mathbf{D} &= [(\frac{1}{2}xz)^n \cdot (\frac{1}{2}z)^{n+1} - x(\frac{1}{2}z)^n \cdot (\frac{1}{2}xz)^{n+1}] \cdot \frac{1}{\Gamma(n+1)} \cdot \frac{1}{\Gamma(n+2)} \\ &= \frac{(\frac{1}{2})^{2n+1} z^{2n+1} x^n}{\Gamma(n+1)\Gamma(n+2)}(1-x^2) \end{aligned} \tag{7.13}$$

$$\begin{aligned} \mathbf{N} &= x(\frac{1}{2}xz)^{n+1} \cdot \frac{1}{\Gamma(n+2)} (\frac{-i}{\pi})(\frac{1}{2}z)^{-n}(n-1)! + \frac{i}{\pi}(\frac{1}{2}z)^{-n-1} n! \cdot (\frac{1}{2}xz)^n \cdot \frac{1}{\Gamma(n+1)} \\ &\xrightarrow{\text{keep the lower power term}} \quad \frac{i}{\pi}(\frac{1}{2})^{-1} x^n \end{aligned}$$

(7.14)

So

$$[T]_n \sim \frac{\mathbf{N}}{\mathbf{D}} = \frac{i\pi}{4^{n+1} n!(n+1)!} \cdot (x^2-1) \cdot z^{2n+2}, \quad n \geq 1 \tag{7.15}$$

When $n = 0$, we plug (7.3)~(7.6) into the numerator and denominator,

$$\begin{aligned} \mathbf{N} &= J_0(xz)J_1(z) - xJ_0(z)J_1(xz) \\ &= \left[1 - \frac{x^2 z^2}{4}\right]\left[\frac{z}{2} - \frac{z^3}{16}\right] - x\left[1 - \frac{z}{4}\right]\left[\frac{xz}{2} - \frac{xz^3}{16}\right] \\ &\sim \frac{z^2}{2} - \frac{x^2 z}{2} \\ &= \frac{z}{2}(1-x^2) \end{aligned} \tag{7.16}$$

$$\begin{aligned}\mathbf{D} &= xJ_1(xz)H_0^{(1)}(z) - H_1(z)J_0(xz) \\ &= x[\frac{xz}{2} - \frac{x^3z^3}{16}](\frac{2i}{\pi}\ln z) - (-\frac{2i}{\pi z})(1-\frac{x^2z^2}{4}) \\ &\sim \frac{2i}{\pi z}\end{aligned} \tag{7.17}$$

$$[T]_0 \sim \frac{\mathbf{N}}{\mathbf{D}} = \frac{\pi z^2}{4i}(1-x^2) \tag{7.18}$$

In the case of PEC, $x \to \infty$ such that

$$[T]_n = -\frac{J_n(z)}{H_n^{(1)}(z)} \sim -\frac{(\frac{1}{2}z)^n \frac{1}{\Gamma(n+1)}}{-\frac{i}{\pi}(\frac{1}{2}z)^{-n}(n-1)!} \sim -(\frac{1}{2}z)^{2n}\frac{\pi i}{n!(n-1)!},\ \mathrm{n} \geq 1 \tag{7.19}$$

$$[T]_0 = -\frac{J_0(z)}{H_0^{(1)}(z)} \sim -\frac{1-\frac{z^2}{4}}{\frac{2i}{\pi}\ln z} \sim \frac{1}{\frac{2i}{\pi}\ln z} = \frac{\pi i}{2\ln z} \tag{7.20}$$

Under the TM incidence, $[T]_0$ in dielectric case is on the same order of $[T]_1$ in PEC case. So in the mixed boundary problem we should pay attention to this specific point.